

# St. George's Weapon of Choice: the LANCE

Michael Kurkowski

2018 NSF/REU Program

Physics Department, University of Notre Dame

Advisor: M. Couder



**Figure 1:** *St. George Recoil Mass Separator. Source: [1]*

## 1 Abstract

Stars are powered by nuclear fusion. Understanding the reactions rates of specific nuclear reactions is crucial to understanding various properties of stars (e.g., lifetimes, element formation, energy generation, etc.). St. George (Fig. 1) is a recoil separator that was designed to look at these astrophysical nuclear reactions. Of particular interest are  $(\alpha, \gamma)$  reactions. With St. George, we can measure these reaction cross sections in the lab by bombarding a helium target with heavy ions and sending the beam and the reaction products through St. George to isolate the desired recoil and extrapolate a reaction rate.

The number of reaction products reaching the detection system at the end of St. George is proportional to the number of projectiles (beam particles), the amount of helium in the target, the probability of reaction (cross section), the transmission of the recoil through St. George, and the probability that the reaction product in a specific charge state is transported in St. George. One important aspect of this study is the theoretical prediction of this charge state production. We use a code, ETACHA, to estimate the charge state. We developed a Python interface, the Laborsaving Algorithm for Navigating the Code ETACHAx (LANCE), to the program and compared its predictions with the measurements.

## 2 Introduction

When a large enough cloud of gas in space clumps together due to the gravitational pull of each

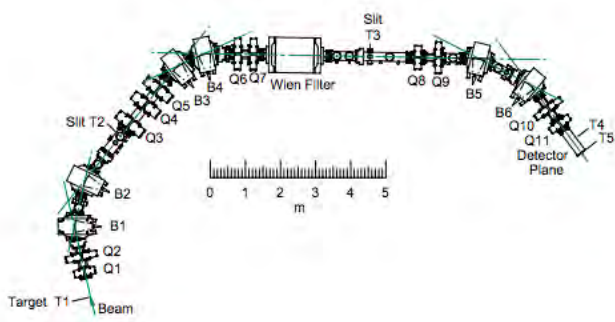


**Figure 2:** *Layout of St. George. Source: [2]*

individual particle, it becomes very dense and hot in the center, triggering a fusion reaction. The collision of atomic nuclei to form heavier elements gives off energy in the form of photons (or other particles' kinetic energy) that we can eventually see on earth, and we call these stars. The cross section (reaction rate) of specific nuclear reactions can be calculated via theoretical models, and verified in Notre Dame's Nuclear Science Lab (NSL).

Of particular interest are  $(\alpha, \gamma)$  reactions, where a heavier nucleus and an alpha particle collide and fuse together. Since the sum of the individual nuclear energies is greater than the energy of the resultant nucleus (a stable reaction product), energy must be released in this reaction, and we see it in the form of gamma rays. In stars, the nuclei don't always have enough energy to overcome the coulomb barrier, which means that classically, stellar lifetimes would be orders of magnitude shorter than they have been observed

to be. With a quantum mechanical understanding, we know that despite the lack of sufficient energy to overcome the barrier, the nuclei fuse anyway, and the reaction occurs.

In the NSL, we can reproduce these reactions utilizing a method called inverse kinematics, where we bombard a helium gas target with a heavier ion accelerated by the Santa Ana (5U) accelerator. Since the cross section is so low (a very small quantum mechanical probability to tunnel through the coulomb barrier), we accelerate the ions to much higher energies (up to 5 MeV) than the stellar interior and extrapolate the cross section at stellar temperatures. The Strong Gradient Electromagnetic Online Recoil separator for capture Gamma-ray Experiment (St. George) was built to analyze these specific reactions, utilizing various dipole and quadrupole magnets to select the desired recoils (products of reaction) and focus the beam, respectively. It also uses a Wien filter to reject recoils that are not of a specific velocity.

The total particle transmission number at the end of the beamline can be calculated as the product of the number of beam particles sent, the amount of target, the cross section of the reaction being studied, the transmission of St. George, and the distribution of recoils in a given charge

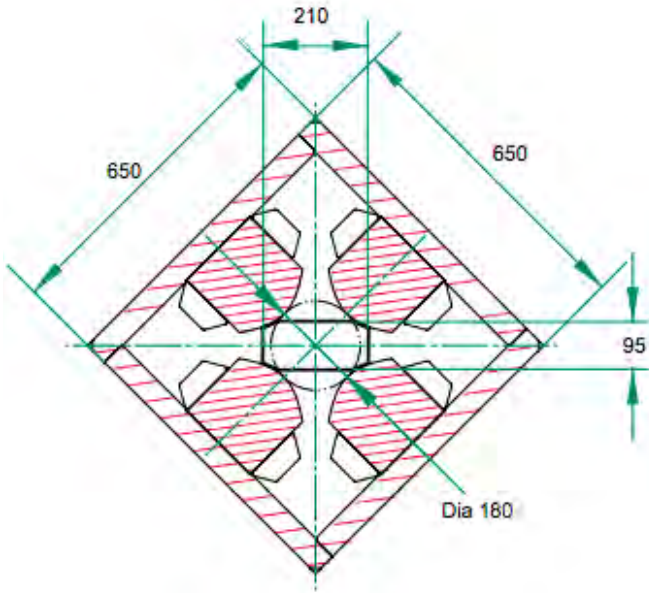


**Figure 3:** Cross section image of a St. George quadrupole magnet. Source: [2]

state:

$$N_{recoils} = N_{projectiles} \times n_{target} \times \sigma \times T_{St.G} \times p_q$$

We know the number of particles accelerated and the amount of target, and we have a fairly accurate theoretical prediction of the cross section. Fortunately, the transmission of St. George is close to 100%, so we can accurately analyze the charge state distribution. We compared it with a theoretical model encapsulated in ETACHA4 [3], as well as previous versions of the ETACHA code, coupled with a Python interface, the Laborsaving Algorithm for Navigating the Code ETACHAx (LANCE). We also created a companion program in Python to make running ETACHA and parsing

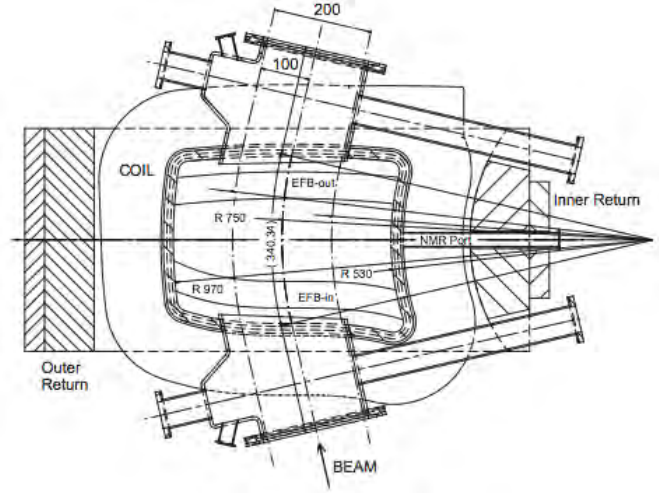


**Figure 4:** Dipole magnet in vacuum chamber. Source: [2]

its output easier.

The ETACHA code takes into account the atomic mass, number, charge, and incident energy of the incoming beam, as well as the atomic mass and number and density of the target through which it is being accelerated. It then allows the user to specify error parameters, and energy loss if desired. It then performs a Monte Carlo simulation, predicting the eventual charge state distribution of the beam, and returns the data in a separate output file.

### 3 Analysis

The Lorentz force guides most of the beam we analyze in St. George. We know that  $F = q(E + v \times B)$ , so setting this equal to  $mv^2/r$  with  $E =$

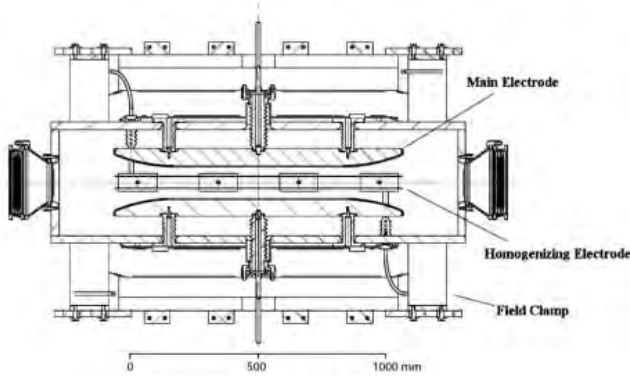


**Figure 5:** *Wien Filter used in St. George, top-down view. Source: [2]*

0 N/C and rearranging, we have

$$qvB = \frac{mv^2}{r} \implies B = \frac{mv}{qr}.$$

This allows us to adjust our the current running through the electromagnet to select specific re-coils.

The Wien filter also operates via the Lorentz force, the cross section of which can be seen in Fig. 5. It employs perpendicular magnetic and electric fields to select only velocities directly related to the magnitudes of the fields:

$$F = qvB, F = qE \implies qvB = qE \implies v = \frac{E}{B}.$$

Thus, only particles of a specific velocity will travel through the filter without being deflected; all others will experience a lateral force and be rejected.

When ions of a specific charge pass through

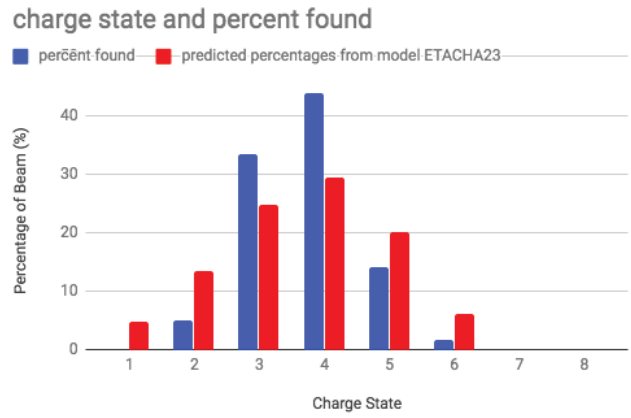


**Figure 6:** *Charge State Distribution of  $^{16}O^{3+}$  in  $^{12}C$  foil target*

a given target, they can gain or lose electrons in their outer shell. Depending on the element, its energy, and the target it's passing through, the resultant charge state distribution will be centered around one of these charge states, and the width of its spread will vary.

## 4 Data & Findings

One version of the ETACHA code (ETACHA23) produced a charge state distribution similar to the data from our most recent run, although its distribution was wider than the one detected in the lab, as seen in Fig. 6. There are several factors that could cause this behavior, namely, whether the energy loss calculation is accurate, or other specific qualities in the target that the program doesn't take into account.

This poses an interesting problem, that of

which theoretical model to trust, or if one is correct, why its distribution doesn't match the data. In the future we will be conducting more simulations and calculations to verify the theoretical model, along with finalizing the Python interface, the LANCE.

## References

- [1] University of Notre Dame, Institute for Structure and Nuclear Astrophysics <https://isnap.nd.edu/research/facility/experimental/st-george/>
  
- [2] M. Couder, G.P.A. Berg, J. Görres, P.J. LeBlanc, L.O. Lamm, E. Stech, M. Wiescher, J. Hinnefeld, <https://pdfs.semanticscholar.org/0bc0/b47e5079a391fb4bec80c027dc3e77c38bf3.pdf>
  
- [3] E. Lamour, P.D. Fainstein, M. Galassi, C. Prigent, C.A. Ramirez, R.D. Rivarola, J.-P. Rozet, M. Trassinelli, and D. Vernhet <https://journals-aps-org.proxy.library.nd.edu/prd/pdf/10.1103/PhysRevA.92.042703>

# An Electromechanical Model of Cardiac Myocyte with Death

Baiting Liu

2018 NSF/REU Program

Physics Department, University of Notre Dame

Advisor: Derviş Can Vural

## Abstract

This is a part of a study on how two different types of cells can support each other. We are going to study a system that including two types of cells, cardiomyocytes and fibroblasts, to explore how cells cooperate in organs. Using the classical Hodgkin-Huxley Model, we can model the electrical activations of neuron-like myocytes. The mechanical movement of the myocytes is coupled with the electrical activities in heart tissues to let the heart beat as a whole periodically. However, as the cells die, the heart tissue, a system consisting of myocytes, will lose its steady state at some critical point. In this paper, an electromechanical model will be used to describe the activities in heart tissues. The death of cells is introduced into the model and we can observe when the death will break the balance of the whole tissue.

## 1 Introduction

A Heart is a network of cells that is functioned to contract together to pump the blood in our bodies. The muscle cells in hearts, or cardiomyocytes, can be excited by external electrical signals and can pass the excitation on to other cells. This is almost the same as the network of neurons, except that there is also mechanical movements coupled with electrical activities in cardiomyocytes, which makes the case more complicated. Therefore in cardiac tissues, we can observe special electromechanical patterns such as rotating spiral waves in special situations[1][2], such as when the heart is undergoing serious diseases. The turbulence patterns in heart tissues have been studied for a long time in medical research[4]. Many studies focus on the electromechanical patterns of cardiac tissues[1][2][3], but none of them have included cell death. In fact, cell death is the main cause of a number of serious heart diseases, including myocardial infarction and heart failure[5]. As the cell death accumulates, the system will no longer function properly. The purpose of this paper

is to add cell death into the electromechanical model and to see if there is a critical point at which the heart will lose its normal rhythm.

## 2 Model

To model the pumping heart, we need a model to describe the excitement and relaxation in the tissue both electrically and mechanically. For the electrical activity, there are quite a lot of Hodgkin-Huxley models that we can use. Some of them are complicated while some are quite simplified. And for the mechanical activity, the tissue have internal stress generated by the strain, and the stress is coupled with the electrical process. Therefore we can have an electromechanical model to describe the overall state of the tissue. The next thing is to add cell death into the electromechanical model we already have.

### 2.1 Electrical Model

There are a lot of models that can describe the electrical activity of heart cells, most of which have a similar form to Hodgkin-Huxley Model(HH model)[6]. The HH model abstract the excitable cells into a circuit, in which the membrane is a capacitor and the ion channels are different resistors. Generally speaking, the form of HH type models is:

$$C \frac{\partial u}{\partial t} = \partial x^2 + I_{ion}(u, w) + I_{ext} \quad (1)$$

Here  $u$  is the electric potential,  $C$  is the capacity of the membrane,  $I_{ion}$  is the current through the ion channels and  $I_{ext}$  is the external current. For each type of ion current, there is an extra differential equation describing how open the channels are. Eq. (1) is the model for a single cell. When intercellular propagation of the excitement is involved, there must be a second order gradient term added:

$$C \frac{\partial u}{\partial t} = D \frac{\partial^2 u}{\partial x^2} + I_{ion}(u, w) + I_{ext} \quad (2)$$

Where  $D$  is a tensor of conductivities. For homogenous distribution of cells,  $D$  is 1 and can be omitted. The difference between the models is that they have different ways to determine  $I_{ion}$  and  $I_{ext}$ . The second-order partial derivative on position  $x$  can describe the spread of excitation in space.  $D$  is a parameter of conductivities on the membrane. The model proposed by Aliev and Panfilov [7] is:

$$\frac{\partial u}{\partial t} = D\nabla^2 u - ku(u - a)(u - 1) - vu + I_s \quad (3)$$

$$\frac{\partial v}{\partial t} = \epsilon(u)(ku - v) \quad (4)$$

This is a simplified model which comes from FitzHugh-Nagumo model[8] (FHN model). In this model, there are no forms of different types of ion currents, but a simple form of potential  $u$  and several parameters that can describe the properties of the cell. And here  $v$  represents the “memory” of previous action of potential  $u$ .  $I_s$  is the external current, which can be influenced by the mechanical movement of the cells.

## 2.2 Electromechanical Model: Continuous or Discrete?

There are some popular electromechanical models people use to study the heart tissue. The model we want to use[9] is a brief one, which show the influence of mechanical motions to the electrical excitation by  $I_s$  and  $\nabla^2 u$  using finite deformation elasticity theory. In this model, there are several equations added to the model described by (3) and (4):

$$\nabla^2 u = \frac{\partial}{\partial X_M} \left( \sqrt{C} C_{MN}^{-1} \frac{\partial u}{\partial X_N} \right) \quad (5)$$

$$I_s = G_s (\sqrt{C} - 1) (u - E_s) \quad (6)$$

Here we have two coordinates for position,  $\mathbf{x} = \{x_i\}$  for deformed position and  $\mathbf{X} = \{X_M\}$  for reference configuration (undeformed position).  $C$  is the right Cauchy-Green deformation tensor that shows the connection between two coordinates.  $G_s$

is maximal conductance and  $E_s$  is reversal potential. This equation about  $I_s$  shows how the ion channels depend on the stretching and shrinking.

We must note that the excitation also has influence on the contraction. To show the dependence of stress to the electrical excitation, we need another variable  $T_a$  and another partial differential equation for it:

$$\frac{\partial T_a}{\partial t} = \epsilon(u)(k_{T_a}u - T_a) \quad (7)$$

Here tensor  $T$  is the second PiolaKirchhoff tensor for force per unit area, which has the following form,

$$T^{MN} = \frac{1}{2} \left( \frac{\partial W}{\partial E_{MN}} + \frac{\partial W}{\partial E_{NM}} \right) + T_a C_{MN}^{-1} \quad (8)$$

Newton's law, or equation of force balance, should also be included:

$$\frac{\partial}{\partial X_M} \left( T^{MN} \frac{\partial x_j}{\partial X_N} \right) = 0 \quad (9)$$

Equation (3)-(9) constitute the continuous electromechanical model of heart cells. Continuous models have a lot of advantages and are easier to solve. However, if we want to include cell death, the continuousness may cause some trouble. The first approach is to include cell density in the continuous model. To add cell density  $n$  into the system, we need to change some constant in the previous model, such as  $k(n)$  or  $I_s(n)$ . This approach can be vary hard to reconcile with the reality and sounds baseless. The second approach is to discretize this continuous model.

The discrete form of the previous electromechanical model is already done in a paper[10] which is what we want to use. Instead of using equation (5), (8) and (9), the discrete version uses the forces between each cells.

## 2.3 Cell Death

How can we determine when and where the cell death will happen? According to previous research[11], the death rate of cells depends on the concentration of some

factors secreted by other cells. The factors can be called ‘‘Cooperative Factors’’, or CFs. The relationship between cell density  $n$  and the concentration of CF is:

$$\frac{dn}{dt} = -\frac{\phi_0}{\phi_0 + \phi}n \quad (10)$$

Here  $\phi$  is the concentration of CF, and  $\phi_0$  is a constant that marks the threshold of the concentration  $\phi$  below which the probability of death is more than half.

## 3 Simulation

### 3.1 Method

For now, we are using the finite element method (FEM) to solve the system of Eqs. (3), (4) and (10). To describe the cell death, we change  $I_s$  in Eq. (3) into  $I_s = nI_{s0}$ . We take the initial  $n$  to be 1, initial  $u$  to be  $-70$  and initial  $v$  to be 0. We set the concentration  $\phi$  as an oscillating form:  $\phi = 0.5 + 5(1 + \sin(2\pi t + \pi))(x^2 + y^2)$  It is set to be time-dependent and space-dependent to add some variation to the model. The original external current  $I_{s0} = \frac{30n}{1+e^{1000(\text{mod}(t,1)-0.01)}}$  is a continuous form of square signal, with a period of 1s and duty cycle of 0.01. The boundary conditions for  $u$  and  $v$  are set to be no-flux boundary conditions. For the value of other parameters, we use the numbers in the paper[9]. The model is solved in FreeFem++ using  $\delta t = 0.01$  on a unit square with 100 nodes on the border, and the figures are plotted in MATLAB.

### 3.2 Results

The potential with and without cell death in the center point is shown in Fig. (2)a. Other points in the simulation area show similar results. As a result of alternated  $I_s$ , the electrical potential peaks go down while the density  $n$  is decreasing. Due to the set form of  $\phi$ ,  $n$  decreases approximately exponentially with a periodic fluctuation, which can be seen in Fig. (2)b.

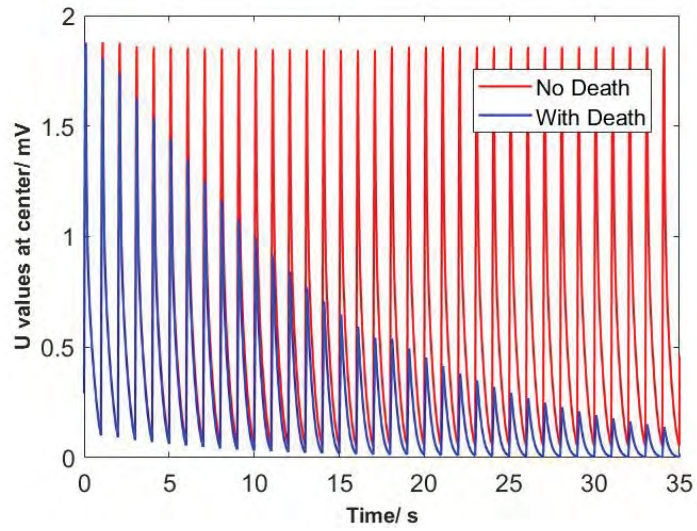
In this result, we can not see the breaking point where the cells lose its steady state. Maybe it is because of the continuity of the model. If you look at the model discretely, the cells at one point is not in two certain state: living or dead, it can only be partly-dead.

## 4 Discussion and Our Next Step

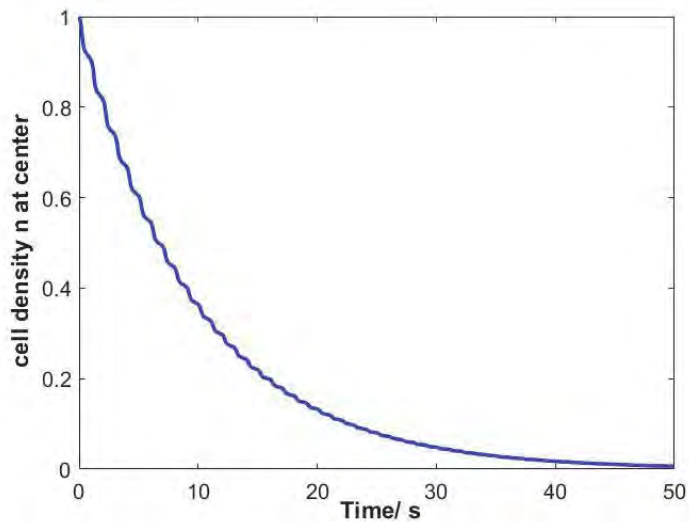
As shown in the previous section, the results from the continuous model seem to be nonsense. It tells us that to add death into the continuous model is much more complicated than what we have done. It also shows that the discrete model is more suitable for our study here because it is more realistic. For cardiac cells, it is a more accurate approximation to see the cells as discrete points, not an abstract density  $n$  on the position.

The next thing we want to do is to solve the discrete model using the method of Verlet integrate[10] in MATLAB. While solving the electro mechanical model of cardiac myocytes, we can easily add cell death into the cell group and see how it lose its steady state with decay. It is still not easy to include death even in the discrete model. What will happen after the cell's death is not certain. Can the myocytes still conduct mechanical contractions or excitations? More research is needed to know for sure.

Another future diafter simulating the myocytes with death successfully, we want to look at a system consists of two types of cells. The experimental setup of this system is shown in Fig. 1. In this experiment, the red cells are cardiac myocytes, which works as a pump to generate the flow in the pipe. And the flow carries the CFs secreted by the fibroblasts along the pipe wall (the green ones). The survival of myocytes depends on the CF secreted by fibroblasts, and the the survival of fibroblasts depends on the flow produced by myocytes. In organisms, there are



(a) potential  $u$  with and without death, at center



(b) cell density  $n$ , at center

Figure 1: Results from Numerical Simulation on Electrical Model

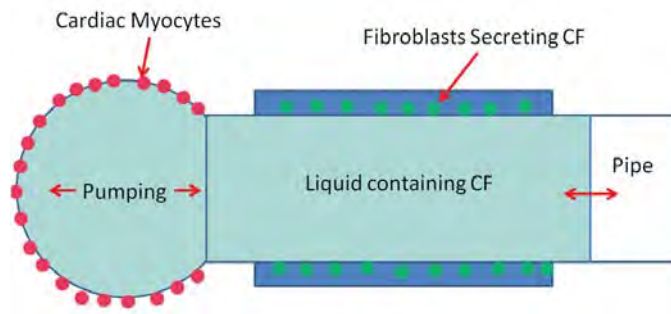


Figure 2: Experimental setup

always different types of cells working together to function the organs, supporting each other, which is similar to the case in our setup. Previous studies of decay are all on systems of single-type cells. So this research may help to understand how complex organs grow old and lose its function.

## 5 Acknowledgements

First I want to thank my advisor, Derviş Can Vural, for accepting me in his group and leading me into the field of doing researches. Thanks for the help of the super smart graduate students Gurdip Uppal, Vu Nguyen and Francesco Pancaldi. And thanks to Rebeckah Fussell, she is really a brilliant girl and pleasant to work with. Special thank you to Lori Fuson and Prof. Umesh Garg, they really helped me a lot with my life during the REU program.

## References

- [1] Winfree, A.T., 1989. Electrical instability in cardiac muscle: phase singularities and rotors. *J. Theor. Biol.* 138, 353C405.

- [2] Davidenko, J.M., Pertsov, A.M., Salomonsz, R., Baxter, W.T., Jalife, J., 1992. Stationary and drifting spiral waves of excitation in isolated cardiac muscle. *Nature* 355, 349C351.
- [3] Abildskov, J.A., Lux, R.L., 1991. The mechanism of simulated Torsade de Pointes in a computer model of propagated excitation. *J. Cardiovasc. Electrophysiol.* 2, 224C237.
- [4] Kohl, P., Ravens, U. (Eds.), 2003. Mechano-electric feedback and cardiac arrhythmias. *Prog. Biophys. Molec. Biol.* 82(1C3), 1C266.
- [5] Konstantinidis, K., Whelan, R., Kitsis, R., 2012. Arteriosclerosis, Thrombosis, and Vascular Biology 32,1552-1562
- [6] Hodgkin, A.L., Huxley, A.F., 1952. A quantitative description of membrane current and its application to conduction and excitation in nerve. *The Journal of Physiology* 117 (4): 500C44.
- [7] Aliev, R.R., Panfilov, A.V. 1996. A simple two-variable model of cardiac excitation. *Chaos, Solitons and Fractals* 7 (3),293C301.
- [8] FitzHugh R. 1961 Impulses and physiological states in theoretical models of nerve membrane. *Biophysical J.* 1:445C466
- [9] Nash, M.P., Panfilov, A.V. 2004. Electromechanical model of excitable tissue to study reentrant cardiac arrhythmias, *Progress in Biophysics & Molecular Biology* 85, 01C522
- [10] Weise, Louis D., Nash, M. P., Panfilov, A. V. 2011. A Discrete Model to Study Reaction-Diffusion-Mechanics Systems. *Plos One.* 6.7:: e21934.
- [11] Suma, D., Acun, A., Zorlutuna, P., Vural, D. C. 2018. Interdependence theory of tissue failure: bulk and boundary effects. *Royal Society Open Science*, 5(2).

# Production of $^{149}\text{Tb}$ for Medical Diagnostics and Treatment

Mallory McCarthy

2018 NSF/REU Program

Department of Physics, Notre Dame University

Advisor: Graham Peaslee

## Abstract:

Long-lived radioactive isotopes are used for applications such as cancer diagnostics and treatment. These isotopes must typically satisfy several criteria to be suitable – such as having an appropriate half-life and specific decay properties. We produced  $^{149}\text{Tb}$  ( $t_{1/2} = 4.1$  hrs) by an indirect heavy ion reaction,  $^{141}\text{Pr}(^{14}\text{N}, 6n)^{149}\text{Dy}$ , which subsequently decayed to  $^{149}\text{Tb}$ . A 10 MeV/n  $^{14}\text{N}$  beam was accelerated by the K150 Cyclotron at Texas A&M University's Cyclotron Institute and irradiated a  $\text{Pr}_6\text{O}_{11}$  target. The long-lived products produced in this reaction were identified by gamma-rays with a high-purity germanium detector set to measure off-line in one-hour increments over 22 hours. This information was used to measure the original activity of  $^{149}\text{Tb}$  at the end of beam and to calculate the reaction cross section. The observed cross section is significantly lower than the theoretical cross section, although this difference has been seen previously in the literature.

## Introduction:

The process of producing an long-lived radioisotope via a nuclear reaction and isolating it for a specific purpose is known as isotope harvesting. Specifically, isotopes for diagnostics and therapeutics within the field of nuclear medicine are examples of practical applications of isotope harvesting. For these radioactive isotopes to be considered, they have to meet the following criteria: ability to target a specific region of the body, a specific type of radiation, a moderate half-life, and the ability to be produced in abundance. Medical isotopes typically are bound to compounds that have specific ligands that are responsible for delivering the radioactive isotope to a certain type of cancer cell. These ligands are sugar and antibody derivatives that allow for the radioactive isotope to accumulate in the cancer cell. For example, many cancer cells exhibit elevated growth rates compared to normal cells, resulting in a preferential uptake of sugar. A

radiolabeled sugar:  $^{18}\text{F}$ -fluorodeoxyglucose is often used for PET (Position Emission Tomography) imaging because this radioisotope is  $\beta^+$ , or positron emitter with a moderate (2 hour) half-life. When a positron interacts with an electron in the cancer cell, two back-to-back gamma rays are produced (precisely  $180^\circ$  to each other) through an annihilation reaction, demonstrated by Figure 1. The detection of these characteristic gamma rays can be used to reconstruct the exact source of the positron emission spatially within a patient. Alpha emitting isotopes are typically used for cancer treatments because of their high linear energy transfer; this energy is deposited into nearby cancer cells, thus preferentially killing cancer cells instead of normal cells. Alpha particles have low penetration range and can damage the cancer cells without harming the surrounding, healthy tissue.

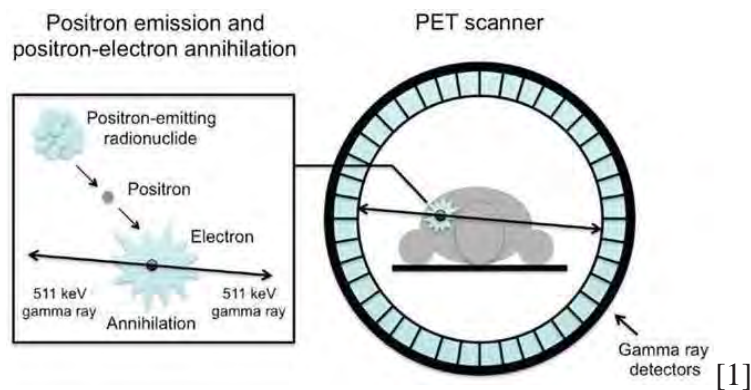


Figure 1. The annihilation of a positron with an electron, as well as the emission of the two  $\gamma$  rays.

The half-life of any medical radioisotope is crucial too. These isotopes are often produced in a separate location from the medical treatment facility, and therefore need to be combined with the medical compound and then transported and administered to the patient. The half-life must be long enough such that sufficient radioactivity survives this process but not too long such that the radioactive isotope continues to radiate the patient beyond the therapeutic dosage. This consideration is also critical for the daughter products as well [2].

In this experiment,  $^{149}\text{Tb}$  was produced and studied to measure the cross sections, in order to assess the possibility of a novel production mechanism for this isotope.  $^{149}\text{Tb}$  has a half-life of 4.1 hours and undergoes  $\beta^+$  (7.1%),  $\alpha$  (16.7%), and EC (76.2%) decay [3]. This is a potentially useful medical isotope because it provides both diagnostic capability (positron emission) and therapy (alpha emission) from a single isotope. Very few isotopes can do this, and  $^{149}\text{Tb}$  is the lightest alpha emitter known. To calculate the cross sections of the  $^{149}\text{Tb}$  produced in this experiment, a specific gamma ray of the decaying radioisotope, 164 keV, was measured and integrated.  $^{149}\text{Tb}$  has other gamma ray emissions, however these were not useful due to their low branching ratio and background contamination with identical decay energies,

#### Experiment:

The target was a  $\text{Pr}_6\text{O}_{11}$  powder held in an aluminum target frame (Figure 2) with a 12.5  $\mu\text{m}$  foil on top (Figure 3). Praseodymium was used as a target because it is monoisotopic, or where only one stable isotope exists. The predicted  $^{149}\text{Tb}$  cross section has a maximum cross section at 107 MeV of the  $^{141}\text{Pr}(^{14}\text{N}, 6n)^{149}\text{Dy}$  reaction. Other thicknesses of Al foil were used to study the cross section as a function of energy. These are indirect reactions where atoms  $^{149}\text{Dy}$  produced in the reaction subsequently decay into  $^{149}\text{Tb}$ . The target was oriented at a  $10^\circ$  angle with respect to the beam in order to decrease localized target heating due to the irradiation. The target was held in a vacuum chamber shown in Figure 4. The  $^{14}\text{N}$  was accelerated to 10 MeV/n at 100 nA at Texas A&M University's Cyclotron Institute K150 cyclotron. Different aluminum cover foils were used to change the bombarding energy to study the cross section as a function of energy. Figure 3 shows the 12.5  $\mu\text{m}$  foil.



Figure 2.  $\text{Pr}_6\text{O}$  powder target



Figure 3. Target with  $12.5\ \mu\text{m}$  Al foil

The irradiation time was 20 minutes. Immediately after the run, the samples had an approximate activity of 70 mrem/hr. After the end of beam, the target was analyzed with a germanium detector for hour-long increments over a period of 22 hours.

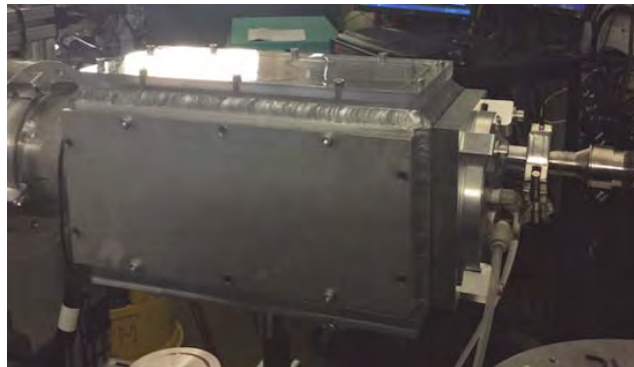


Figure 4. Vacuum Chamber

### Analysis:

To determine the cross section for the production reaction, the original activity (end of beam) of  $^{149}\text{Tb}$  has to be found. Note, these calculations are for the  $12.5\ \mu\text{m}$  Al foil target. To do this, the

activity of the  $^{149}\text{Tb}$  must be measured over a period time.  $^{149}\text{Tb}$  has a characteristic gamma ray line at 164 KeV. Figure 5 shows a typical spectrum.

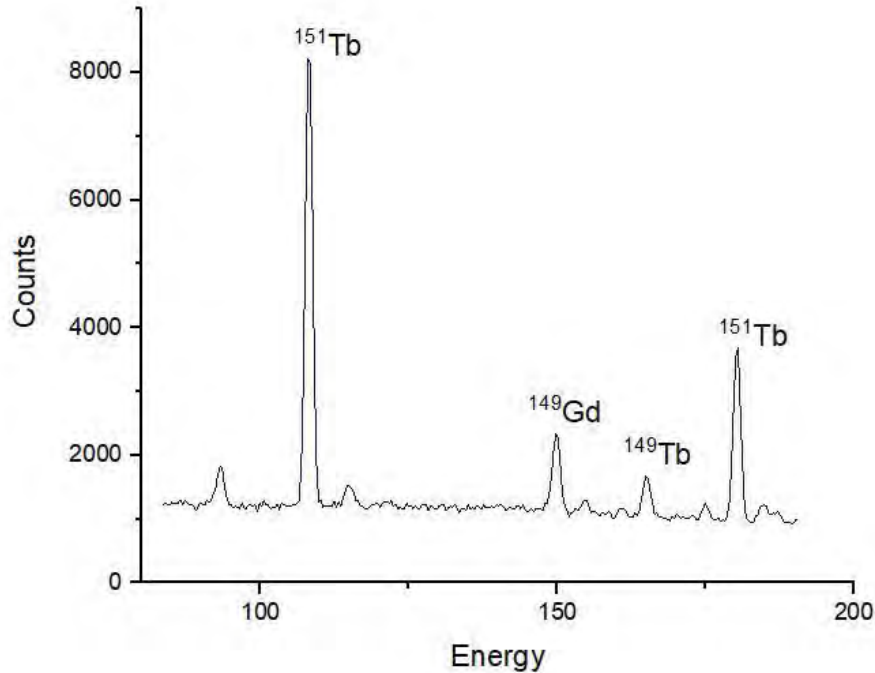


Figure 5. Spectra of 4<sup>th</sup> Measurement of Target (18hr) after EOB

This spectrum results from the decay of  $^{149}\text{Tb}$  into its daughter products, which means  $\alpha$ ,  $\beta^+$ , and  $\gamma$ -rays are associated with each decay. The activity (decays/s) for this decay channel was measured over time to find the original activity at end of beam. Many other products were formed and the majority have milliseconds - few minutes half-lives. Immediately after beam, the detector was flooded with signals indicating decays and no beneficial information was obtained until most of the other products decayed away after 1 hour. By integrating the peaks, this essentially gives us the activity of the  $^{149}\text{Tb}$  at the time of the measurement. It is possible to calculate how much was created with the relationship  $A = \omega N$  where  $\omega$  is  $\ln(2)/t_{1/2}$  and N is number of atoms. The integrations were corrected for detector efficiency, geometry, branching ratios, and duration of the run shown by the formula below [4].

$$Activity = \frac{Counts}{BR * Eff * \Omega} \quad (1)$$

where BR= branching ratio; Eff= Detector efficiency at 164 keV;  $\Omega$  = solid angle.

Each measurement was for one hour. The measurements were taken at approximately 4.5, 12, 18, and 22 hours after the end of beam. Figure 6 plots the activity of the  $^{149}\text{Tb}$  over time on a semi-log scale.

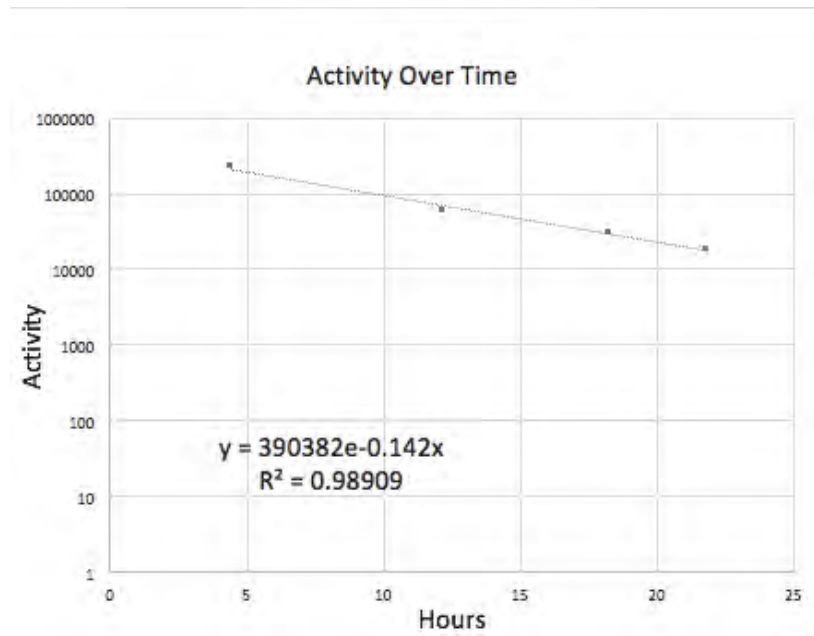


Figure 6. Activity of  $^{149}\text{Tb}$  over a period of 22 hours

At time 0, this indicates end of beam and the original activity is 390,382 decays/s. Using the equation below with the original activity, the cross section can be calculated. [4]

$$\sigma = \frac{A}{n \Delta x \phi (1 - e^{-\lambda t})} \quad (2)$$

where  $n$ =atoms/cm<sup>3</sup>;  $\Delta x$ =thickness of bombarded target ;  $\phi$ = $^{14}\text{N/s}$

**Results and Conclusion:** The cross section determined was  $11.75 \pm 3.9$  mb. Compared to literature, this cross section is significantly lowered than predicted by PACE4. Figure 7 shows

the predicted products, cross sections, and the important decay chains. The primary ones of interest are  $^{149}\text{Tb}$  and  $^{149}\text{Dy}$ .

**1. Yields of residual nuclei**

Z	N	A	events	percent	x-section(mb)
66	85	<b>151 Dy</b>	14	0.014%	0.198
65	86	<b>151 Tb</b>	7	0.007%	0.0989
64	87	<b>151 Gd</b>	3	0.003%	0.0424
66	84	<b>150 Dy</b>	2680	2.68%	37.9
65	85	<b>150 Tb</b>	962	0.962%	13.6
64	86	<b>150 Gd</b>	153	0.153%	2.16
63	87	<b>150 Eu</b>	1	0.001%	0.0141
66	83	<b>149 Dy</b>	23355	23.4%	330
65	84	<b>149 Tb</b>	8492	8.49%	120
64	85	<b>149 Gd</b>	762	0.762%	10.8
63	86	<b>149 Eu</b>	2	0.002%	0.0283
66	82	<b>148 Dy</b>	14406	14.4%	204
65	83	<b>148 Tb</b>	3948	3.95%	55.8
64	84	<b>148 Gd</b>	514	0.514%	7.26

Figure 7. A portion of the table of isotopes that illustrate the primary products produced in our experiment.

PACE4 makes two assumptions: First, the cross sections and percentages shown are from the direct reaction of that certain isotope. For example,  $^{149}\text{Dy}$  decays in  $^{149}\text{Tb}$ ; however, the number listed does not include both the direct and indirect production of  $^{149}\text{Tb}$ . Second, PACE4 always includes the metastable form of the isotope as part of the percentages. A metastable isotope has the same number of protons and neutrons, but the nucleus is in a different arrangement at a higher energy state. The  $^{149\text{m}}\text{Tb}$  is not useful in the application because it has a short half life and does not decay to the ground state. The PACE4 calculated amount of  $^{149}\text{Tb}$  produced is predominately  $^{149\text{m}}\text{Tb}$ . This is observed to happen at energies higher than 77 MeV [4]. The only viable option to produce  $^{149}\text{Tb}$  is through indirect production and the decay of  $^{149}\text{Dy}$  through

positron emission. Early analysis and literature suggests that no  $^{149}\text{Tb}$  was directly made; the cross section computed was the cross section of the  $^{149}\text{Dy}$  decaying into  $^{149}\text{Tb}$ . However, only 48% decays into the metastable state so the actual full cross section of  $^{149}\text{Dy}$  is  $22.79 \pm 7.6$  mb. It is possible to directly calculate the cross section of  $^{149}\text{Dy}$  through its own gamma ray lines, however  $^{149}\text{Dy}$  has a 4-minute half-life and was lost before these measurements were made. PACE4 calculated the cross section of the  $^{149}\text{Dy}$  to be 330. The percentage of observed cross is to be  $22.79/330 = 6.91\%$ . However, it is important to note that  $^{149\text{m}}\text{Dy}$  can be formed as well. This does not affect the observable cross section because  $^{149\text{m}}\text{Dy}$  will decay to  $^{149}\text{Tb}$  as well. All combinations of projectiles ( $^{10}\text{B}$ ,  $^{11}\text{B}$ ,  $^{12}\text{C}$ ,  $^{14}\text{N}$ ,  $^{15}\text{N}$ ,  $^{16}\text{O}$ ,  $^{18}\text{O}$  and  $^{19}\text{F}$ ) and targets (Ba to Nd) used in the simulations of this production of  $^{149}\text{Tb}$ , yielded had a maximum observed cross section of 7% [4]. This can be due to the spin states of the nuclei of both projectile and target. For future plans, the other energies 18 and 30  $\mu\text{m}$  Al foils will be evaluated as well to find cross sections as a function over energy. A radiochemical isolation process is being developed, where the  $^{149}\text{Tb}$  can be extracted and bound to antibodies that can deliver the isotope to cancer cells. These results are preliminary.

**Acknowledgements:** I would like to thank Sherry Yennello and Alis Rodriguez Manso for help running the experiment at Texas A&M University Cyclotron Institute as well as Suzanne Lapi and her group at University of Alabama-Birmingham for their collaboration and expertise in isotope harvesting. I would also like to thank Graham Peaslee, John Wilkinson, and Sean McGuinness. This work has been supported by the NSF through the University of Notre Dame's Physics REU as well as the Department of Energy Isotopes Program.

**Sources-**

- [1] <https://www.physicsforums.com/insights/basics-positron-emission-tomography-pet/>
- [2] Lanthanides in Nuclear Medicine: Preparation of  $^{149}\text{Tb}$  by Irradiation with Heavy Ions- Dmitriev 2001
- [3] Production Routes of the Alpha Emitting  $^{149}\text{Tb}$  for Medical Application- Beyer 2001
- [4] Modern Nuclear Chemistry- Loveland, Morrissey, Seaborg
- [5] New Measurement of Cross Section of Evaporation Residues from  $^{200}\text{Pr}+^{12}\text{C}$ : A comparative Study of the Production of  $^{149}\text{Tb}$  – Maiti 2011

Using Particle Interaction Simulations to Understand Tracker Efficiency for  
the Phase II High Luminosity Upgrade on the CMS Experiment

Christopher E. McGrady

2018 NSF/REU Program

Physics Department, University of Notre Dame

Advisors:

Kevin Lannon, Michael Hildreth

# Abstract

Given the planned integration of the tracker and the trigger during the Phase II High-Luminosity Upgrade to CMS, it is critical to understand the limitations of the tracker from losses in terms of losses due to high data rates and limited bandwidth readout. This study was performed in order to understand where and under what conditions these data losses occur. Different interactions were simulated in CMS Software (CMSSW) 9.3.7 using samples from both 9.3.2 and 9.3.7 to study track stubs lost under various conditions. It was found that under any interaction conditions with or without additional pileup interactions, with or without pileup most of the losses occurred in the outer barrel layers of the tracker. As additional pileup interactions increased, losses in the inner barrel and end cap at high  $\eta$  increased. Stub losses were also found on the jet axis at high energies of 350 GeV - 1800 GeV. At these energies, the losses from the CMS Binary Chip/Macro Pixel ASIC (CBC/MPA) and the Concentrator Integrated Circuit (CIC) seem to be contributing equally to the total loss while the consistent losses in the outer barrel come from the CBC/MPA limitations and the inner layer losses at high  $\eta$  losses come from limitations in the CIC.

## 1 Background

### 1.1 The LHC

In any experiment, understanding the limitations of any measuring device is critical to understanding the measurements themselves. The Compact Muon Solenoid (CMS) experiment on the Large Hadron Collider (LHC) at CERN is no different. Here, two 6.5 TeV counter-current proton beams are collided at 40 MHz. Different aspects of the resulting particle spray are measured through different layers of the CMS detector. Without a system for data

reduction, the CMS detector would produce 70 Tb/s of data. It was for this reason that the trigger system, where data can be reduced to a receivable level, was created (1).

## 1.2 The CMS Detector

From the hard collision point out, the layers of the CMS detector are the tracker, electromagnetic calorimeter, hadronic calorimeter, superconducting solenoid and muon chamber as seen in Figure 1. This study will concentrate on the tracker which detects the paths of charged particles passing through it.

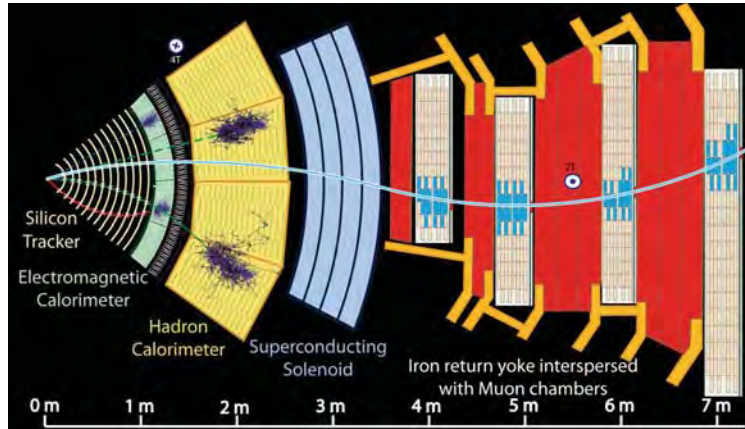


Figure 1: Layers of the CMS detector (2)

The tracker has six barrel and five end cap layers of silicon sensors to detect charged particles. Figure 2 shows the pixel tracker layers in yellow and cyan with the tracker layers are shown in blue and red. This plot shows the radial distance from the barrel ( $r$ ), the distance down the barrel ( $z$ ), and the pseudorapidity ( $\eta$ ). There are four subsections to the detector, The Inner Barrel (TIB), The Outer Barrel (TOB), The Inner Disk (TID), and Two End Caps (TEC). The barrel layers are given by  $z < 1200$  and the disk and end cap layers are located at  $z > 1200$ . TIB and TID are located at  $r < 550$  with TOB and TEC residing at  $r > 550$ . Note that each layer is composed of two parallel layers of detectors; hits in these adjacent layers are grouped into pairs which function as track "stubs". The blue layers are PS modules where

there is a combination pixels and strips while the red shows the 2S modules where there are only strips. This initial part of the detection chain is called the CMS Binary Chip/Macro Pixel ASIC (CBC/MPA). The signal is then sent to the Concentrator Integrated Circuit (CIC).

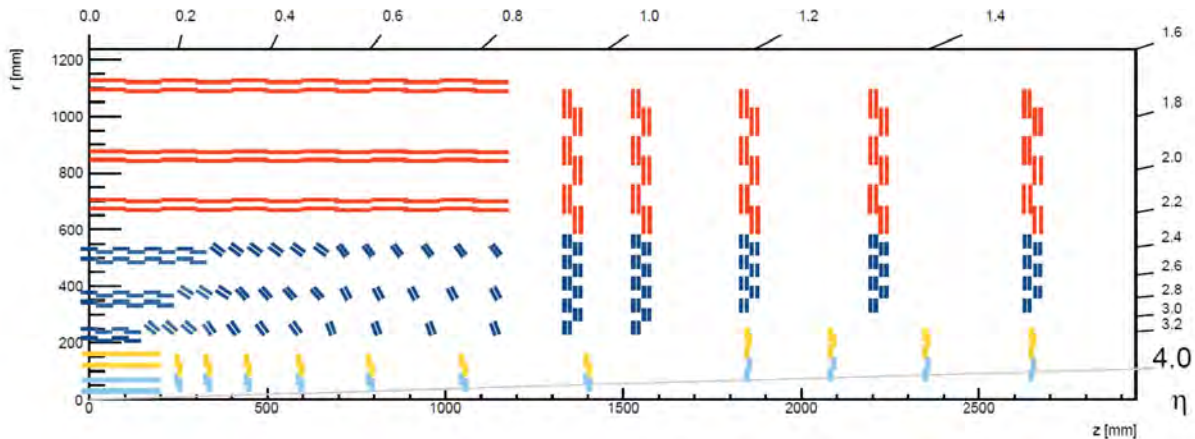


Figure 2: Tracker Detector Layers Including Pixels (3)

Even before the data reduction, there are physical limitations to each of these components. One known cause of reaching these limitations is through pile up which is when there are extra proton-proton collisions. Another possible cause of data losses could be from high-momentum jets. Both of these are studied and their effects are shown later on in this paper.

### 1.3 CMSSW

CMS Software (CMSSW) is the framework for CMS. A simulation of the detector was created as a part of this framework in order to understand how different interactions will effect the detector. This system replicates various limitations on the detector while keeping track of the true event so that what actually happened and what would be detected can be compared. The limitations of interest used in this study are shown below.

```

CBClimit      = cms.uint32(3),    # CBC chip limit (in stubs/chip/BX)
MPAlimit      = cms.uint32(5),    # MPA chip limit (in stubs/chip/2BX)
SS5GCIClimit  = cms.uint32(16),   # 2S 5G chip limit (in stubs/CIC/8BX)
PS5GCIClimit  = cms.uint32(17),   # PS 5G chip limit (in stubs/CIC/8BX)
PS10GCIClimit = cms.uint32(35),   # PS 10G chip limit (in stubs/CIC/8BX)

```

## 2 Methods

CMSSW 9.3.7 was used to run simulations of various interactions from both 9.3.2 and 9.3.7. During each run, the following line from `/TrackTrigger/python/TTStub_cfi.py` was set to true in order to reconstruct the stubs with and without the losses from data limitations.

```

FEineffs = cms.bool(False)

```

The following samples were used. QCD is a high momentum jet production sample while TTBar refers to a top quark pair production. Pile up is the number of extra proton-proton collisions. Pile up 200 is close to what we expect at the detector. The pile up 0 and pile up 300 samples were used as extreme conditions tests. ‘

```

QCD PU200: /RelValQCD_Pt-15To7000_Flat_14TeV/CMSSW_9_3_2-PU25ns_93X_upgrade2
023_realistic_v2_2023D17PU200-v1/GEN-SIM-DIGI-RAW

```

```

TTBar PU0: /RelValTTbar_14TeV/CMSSW_9_3_7-93X_upgrade2023_realistic_v5_2023D
17noPU-v2/GEN-SIM-DIGI-RAW

```

```

TTBar PU200: /RelValTTbar_14TeV/CMSSW_9_3_7-PU25ns_93X_upgrade2023_realistic
_v5_2023D17PU200-v1/GEN-SIM-DIGI-RAW

```

```

TTBar PU300: /RelValTTbar_14TeV/CMSSW_9_3_7-PU25ns_93X_upgrade2023_realistic
_v5_2023D17PU300-v1/GEN-SIM-DIGI-RAW

```

Once the stubs are reconstructed, all stubs that would be lost were flagged by being given an `allstub_trigDisplace` value less than 100. 2D histograms comparing the radial distance ( $r$ ) and the distance down the barrel ( $z$ ) of each stub were then made with and without considering lost stubs. The histogram with lost stubs considered was then divided by the histogram of all stubs to get an efficiency. 1 - the efficiency was then calculated for each layer, separating the barrel from the disk/end cap.

Next, the minimum distance each stub is from a jet ( $\Delta R$ ) in the simulated interaction using change in the the angle from the jet ( $\Delta\phi$ ) and the change in pseudorapidity ( $\Delta\eta$ ) using the following formula.

$$\Delta R = \sqrt{\Delta\phi^2 + \Delta\eta^2} \quad (1)$$

A 2D histogram comparing the energy of the jet and the minimum  $\Delta R$  was then made for both the stubs with and without losses separated by layer and discriminating between the barrel and the disk/end cap. The histogram with the losses considered was then divided by the histogram without losses to get the efficiency. This analysis was only performed on the QCD PU200 sample as it is the only set to reach high enough energies to see losses. A visual representation is given below in Figure 3.

In order to understand where these inefficiencies were coming from, `TTStub_cfi.py` was again modified. The following lines were changed.

```
CBClimit      = cms.uint32(3),    # CBC chip limit (in stubs/chip/BX)
MPAlimit      = cms.uint32(5),    # MPA chip limit (in stubs/chip/2BX)
SS5GCIClimit  = cms.uint32(16),   # 2S 5G chip limit (in stubs/CIC/8BX)
PS5GCIClimit  = cms.uint32(17),   # PS 5G chip limit (in stubs/CIC/8BX)
PS10GCIClimit = cms.uint32(35),   # PS 10G chip limit (in stubs/CIC/8BX)
```

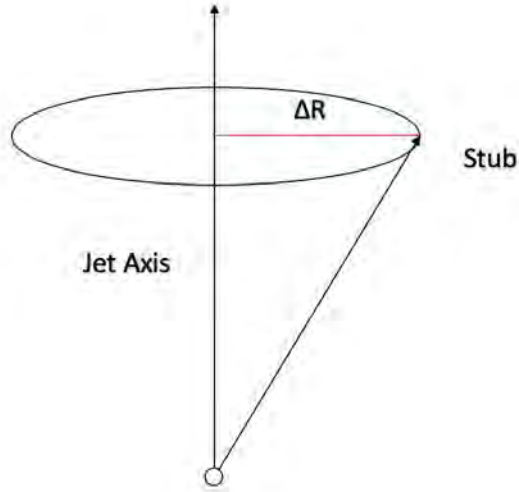


Figure 3: Visual Representation of  $\Delta R$

Two sets of simulated stub reconstructions were performed, one where CBCLimit and MPALimit were set to 20,000 and one where SS5GCICLimit, PS5GCICLimit, and PS10GCICLimit were set to 20,000. The same data sets and analyses were done for these as with the initial simulations.

### 3 Results

The efficiencies with increasing pile up are shown below.

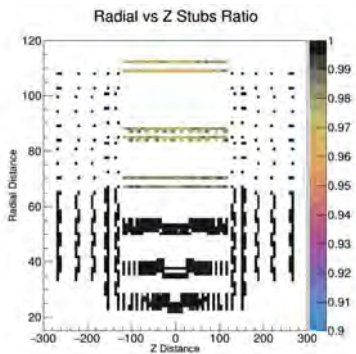


Figure 4: TTBar PU0

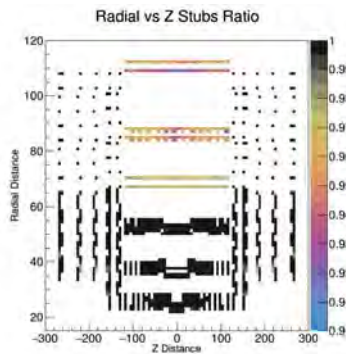


Figure 5: TTBar PU200

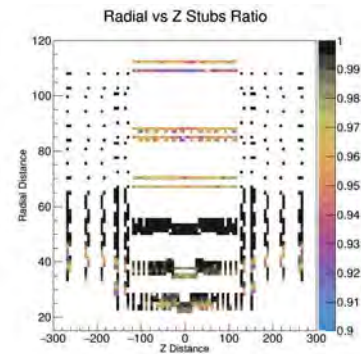


Figure 6: TTBar PU300

Below are the stub losses from pile up.

Table 1: Stub Loss From Pile Up

Location Loss	TTBar PU0	TTBar PU200	TTBar PU300
Layer 1 Barrel	0.15%	0.16%	1.36%
Layer 2 Barrel	0.05%	0.13%	1.02%
Layer 3 Barrel	0.03%	0.08%	0.17%
Layer 4 Barrel	1.51%	2.89%	3.13%
Layer 5 Barrel	2.23%	4.25%	4.34%
Layer 6 Barrel	2.83%	5.41%	5.58%
Layer 1 End Cap	0.07%	0.10%	0.94%
Layer 2 End Cap	0.04%	0.22%	1.88%
Layer 3 End Cap	0.03%	0.24%	1.67%
Layer 4 End Cap	0.03%	0.24%	1.74%
Layer 5 End Cap	0.02%	0.17%	1.39%

Stub efficiency by the jet's energy and its distance from the jet is shown below.

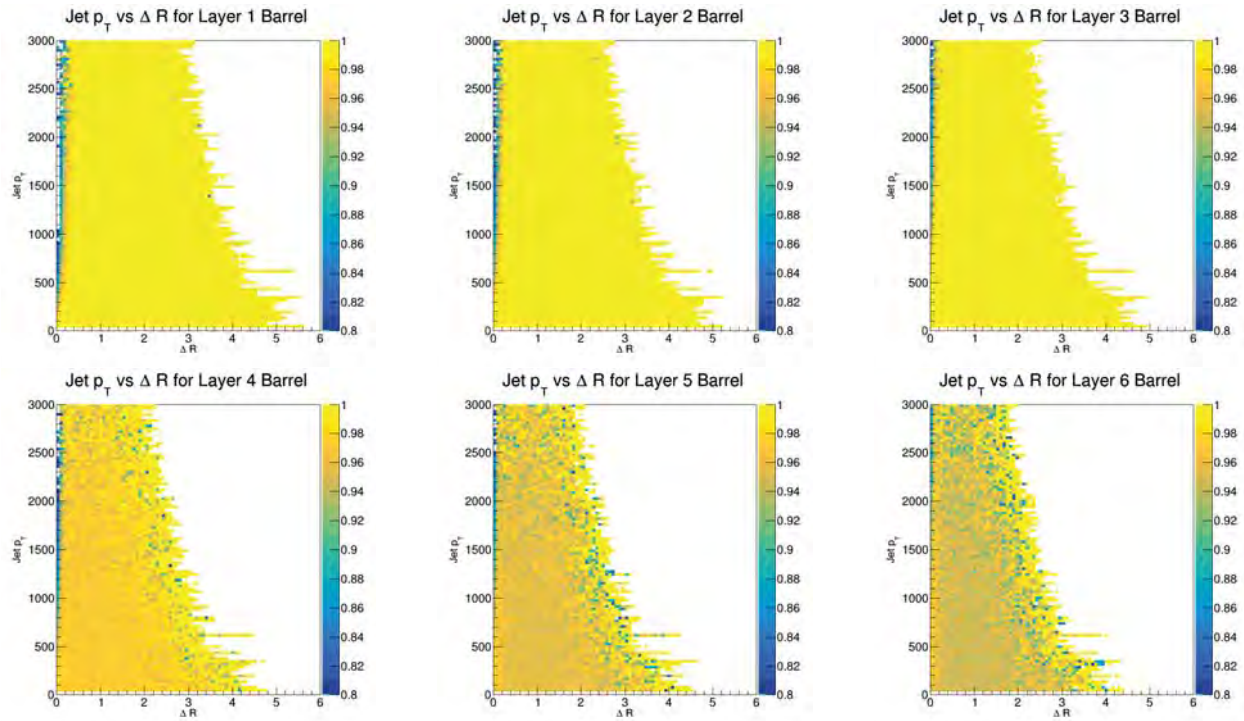


Figure 7: Barrel Stub Efficiency From High Energy Jets

The efficiencies from TTBar PU300 separating losses from CBC/MPA and CIC are shown below.

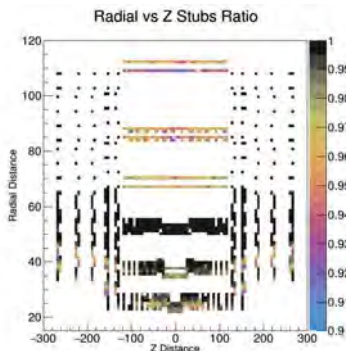


Figure 8: Full Limits

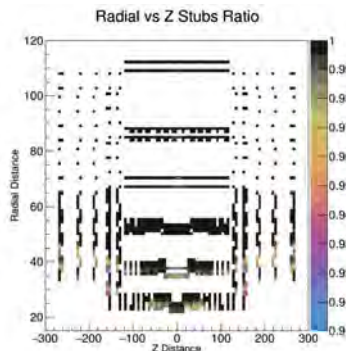


Figure 9: CIC Loss

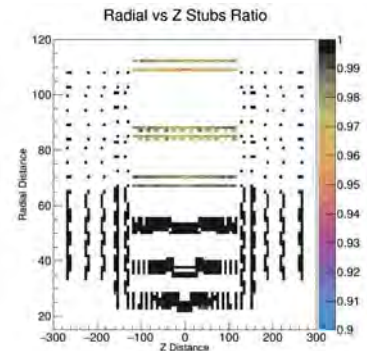


Figure 10: CBC/MPA Loss

Below are the stub losses from CBC/MPA and CIC in a TTBar PU300 sample.

Table 2: Stub Loss From Different Limitations

Location Loss	Full Limits	CIC Losses	CBC/MPA Losses
Layer 1 Barrel	1.36%	0.72%	0.19%
Layer 2 Barrel	1.02%	0.90%	0.04%
Layer 3 Barrel	0.17%	0.05%	0.04%
Layer 4 Barrel	3.13%	0.30%	1.39%
Layer 5 Barrel	4.34%	0.24%	2.20%
Layer 6 Barrel	5.58%	0.15%	2.95%
Layer 1 End Cap	0.94%	0.66%	0.08%
Layer 2 End Cap	1.88%	1.57%	0.11%
Layer 3 End Cap	1.67%	1.56%	0.01%
Layer 4 End Cap	1.74%	1.70%	0.01%
Layer 5 End Cap	1.39%	1.31%	0.01%

## 4 Discussion and Conclusion

As seen in Figures 4, 5, and 6, as pile up increases, heavy losses occur near the collision point and at high  $\eta$ . It should also be noted that regardless of pile up, there are significant losses in The Outer Barrel (TOB). From Table 1, TOB losses range from 1.51% - 5.58%. Figure 7 shows that stub losses  $\geq 10\%$  from jet energy ranges from 350 GeV - 1800 GeV. When the

CIC and CBC/MPA limitations are separated, the losses near the interaction point and at high  $\eta$  is from the CIC limits while TOB losses are from the CBC/MPA as shown by Figures 8, 9, and 10 and Table 2.

From this, one can see that the consistent losses in TOB is from the CBC/MPA. This is likely due to the strip style chipset used in TOB which has a much lower data rate limitation than TIB. Losses close to the interaction point at high pile up is not a heavy concern as a pile up of 300 is a stress test and collisions in the detector should be closer to 200 where losses at TIB and on the disk/end cap never exceed 0.24%. Similarly, the losses from jets are of little concern as well as they occur at energies of 350 GeV - 1800 GeV which are high enough in energy to be detected at the jet trigger. Further studies should be conducted to find ways to remedy TOB losses from the CBC/MPA.

## References

- [1] G. Codiapoti, “Cms level-1 trigger online control system,” in *CMS Induction Course*, 2017.
- [2] F. Hartmann, “Introduction muons, tracker, tracking,” in *CMS Induction Course*, 2017.
- [3] A. Dierlamm, “Cms strip tracker r&d,” 2016.

# Measuring Lifetimes of Excited States in $^{170}\text{Er}$

Martin Meier

2018 NSF / REU Program

Physics Department, University of Notre Dame

Advisors: Prof. Ani Aprahamian, Prof. Shelly Leshner

## Abstract

The nature of excited  $0^+$  bands in nuclei remains the topic of much debate in nuclear structure physics. Obtaining level lifetimes of well-deformed nuclei in the rare-earth region will help guide theoretical interpretations of these bands. This work studies  $^{170}\text{Er}$ , which lacks experimental data for low-lying levels. Using the Doppler-Shift Attenuation Method (DSAM) at the University of Kentucky Accelerator Laboratory, low-lying excited states with energies of  $< 3.4$  MeV were populated and level lifetimes were measured. Preliminary results for level lifetimes, including results for possible  $0^+$  states, will be discussed.

## 1 Introduction

The many-bodied nature of nuclei poses challenges for calculating nuclear properties from equations of the interactions of nucleons alone. Because of this, theories of nuclear structure are vastly simplified pictures of the nucleus not formed from first principles, but rather developed in response to experimental observations. The observation of magic numbers led in part to the development of the nuclear shell model which predicts that nuclei exist in discrete energy levels much like atoms with electronic shell levels. The shell model had surprising predictive power across a wide range of nuclides of measurables like spin and parity of excited states, yet observations of large quadrupole moments in sufficiently heavy even-even nuclei could not be explained by the shell model alone [1]. Expanding the predictive power of the shell model to account for this feature, an improved model describing collective nucleon motion was developed. According to this model, multiple nucleons can move together, contrary to the movement of single valence nucleons in the shell model, creating quantum

vibrations [2].

Although most nuclei exhibit a spherical ground state, heavier nuclei, particularly in the mass region  $150 < A < 180$ , can possess non-spherical, or deformed, ground states. This means vibrations in deformed nuclei can distinguishably align with axes of symmetry of the nuclei, whereas vibrations in spherical nuclei are degenerate with respect to the vibrational axis. The result in deformed nuclei is an excited level scheme where rotational bands are superposed on vibrational modes. Excited states of deformed nuclei in the  $K^\pi=0^+$  rotational band have recently attracted attention by a study that discovered an unexpectedly large number of these states in  $^{158}\text{Gd}$  [3]. This discovery has fueled a wave of research on  $0^+$  states and a debate over how the variations in numbers and energies of these states across nuclides fits into the current theory of the structure of nuclei. My research project aims to collect valuable lifetime data in  $^{170}\text{Er}$ , which is a relatively unstudied nuclide in the deformed region. I hope to report lifetimes of excited states, which will ultimately be used in calculations of transition probabilities which are a key to understanding the nature of  $0^+$  excited states.

## 2 Method

There are multiple methods available to measure lifetimes of excited states in nuclei, and each method has different limitations in its precision and the timescales that it can detect. The method used for this project is the Doppler-Shift Attenuation Method (DSAM) with a sensitivity range in the  $\leq 1$  ps lifetime region. This method relies on inelastic neutron scattering ( $n, n'\gamma$ ) to excite the target nucleus, and exploits the doppler shift on radiation emitted from the recoiling nuclei as detected at forward and backward angles to determine

the time after scattering that de-excitation occurred. The shifted  $\gamma$  ray energy ( $E_\gamma$ ) as a function of the detector angle ( $\theta_{lab}$ ) can be described by:

$$E_\gamma(\theta_{lab}) = E_{\gamma,o} \left[ 1 + \frac{v_{cm}}{c} F(\tau) \cos(\theta_{lab}) \right] \quad (1)$$

where  $V_{cm}$  is the initial velocity of the recoiling nucleus,  $c$  is the speed of light,  $F(\tau)$  is an experimentally determined curve with a theoretical fit for a particular target isotope that takes into account the stopping power of the target medium with respect to a fast moving target nucleus,  $E_{\gamma_0}$  is the unshifted  $\gamma$  ray energy [4]. The  $\gamma$  ray energy versus detector angle is plotted for each  $\gamma$  ray, and the slope of the plots is used to determine the value of  $F(\tau)$  from equation 1 and the theoretical fit of  $F(\tau)$  is used to extract the  $\gamma$  ray lifetime.

Measurements of  $\gamma$  rays at different angles is achieved by placing a detector at angles around the sample. This detector is shown at the  $90^\circ$  location in figure 1, and figure 2 shows the mechanism for rotating the detector around the sample.

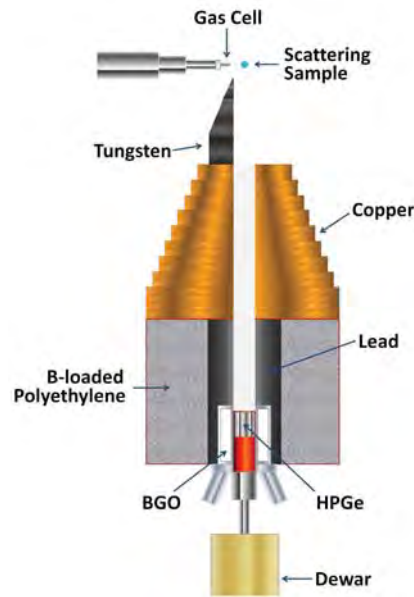


Figure 1: A schematic of the detector and its placement relative to the scattering sample and beam line [5].



Figure 2: The rotating detector apparatus.

Measuring the lifetimes of excited levels in nuclei requires measuring the lifetimes of  $\gamma$  rays leaving those levels, and typically multiple  $\gamma$  rays depopulate the same level from transitions to a number of different lower energy levels. Level lifetimes are most accurately calculated as the average lifetime of all  $\gamma$  rays depopulating that level, so it is necessary to identify all  $\gamma$  rays depopulating the levels of interest.

To aid in the identification, excitation functions for  $\gamma$  rays were performed. This involves measuring a  $\gamma$  ray spectrum for increasing neutron energies in 100 keV increments at a fixed detector angle. The result is information about  $\gamma$  ray yields for a range of neutron energies.  $\gamma$  rays in the same level will have the same energy threshold where they enter the spectrum, and the same qualitative shape of the  $\gamma$  ray yield versus neutron energy plot as shown in fig. 3 for the two  $\gamma$  rays depopulating the 1824 keV level.

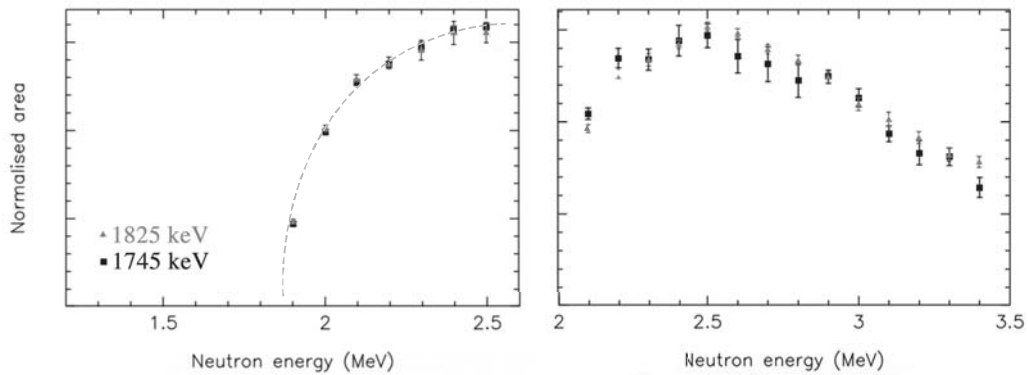


Figure 3: An excitation plot for the 1745 keV  $\gamma$  ray from the 1825 keV excited level. The x-intercept of the dotted fit indicates the energy threshold for this  $\gamma$  ray is  $\sim 1.9$  MeV.

### 3 Results

A partial level scheme shown in fig. 4 denotes the levels measured and the transitions between levels that resulted in detectable  $\gamma$  rays.

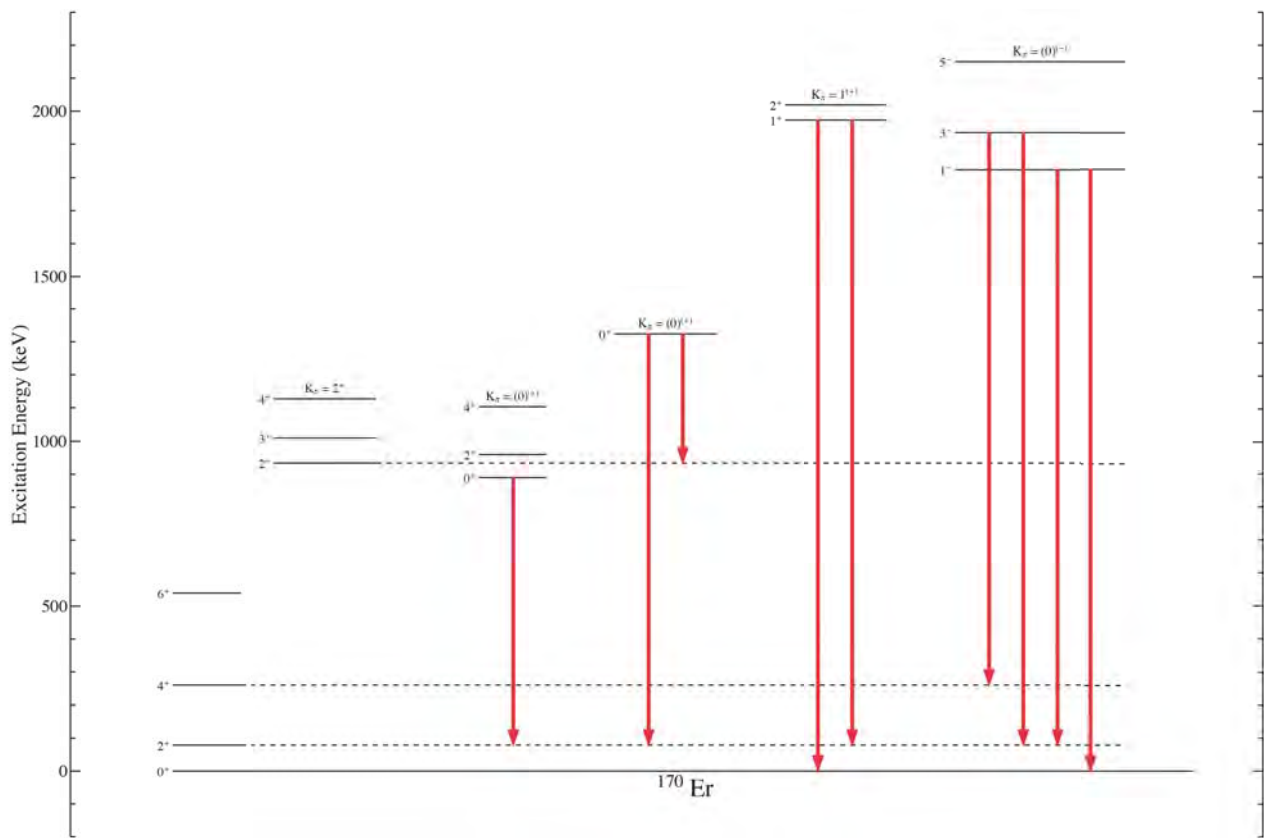


Figure 4: The partial level scheme for low-lying levels in  $^{170}\text{Er}$ . Data represented in this level scheme was obtained from the National Nuclear Data Center (NNDC) [6]

The lifetimes of 3 excited states in  $^{170}\text{Er}$  were measured and lifetime limits for 2 excited states were determined, summarized in table 1. An example of a complete set of plots for an excited level is shown in fig 4.

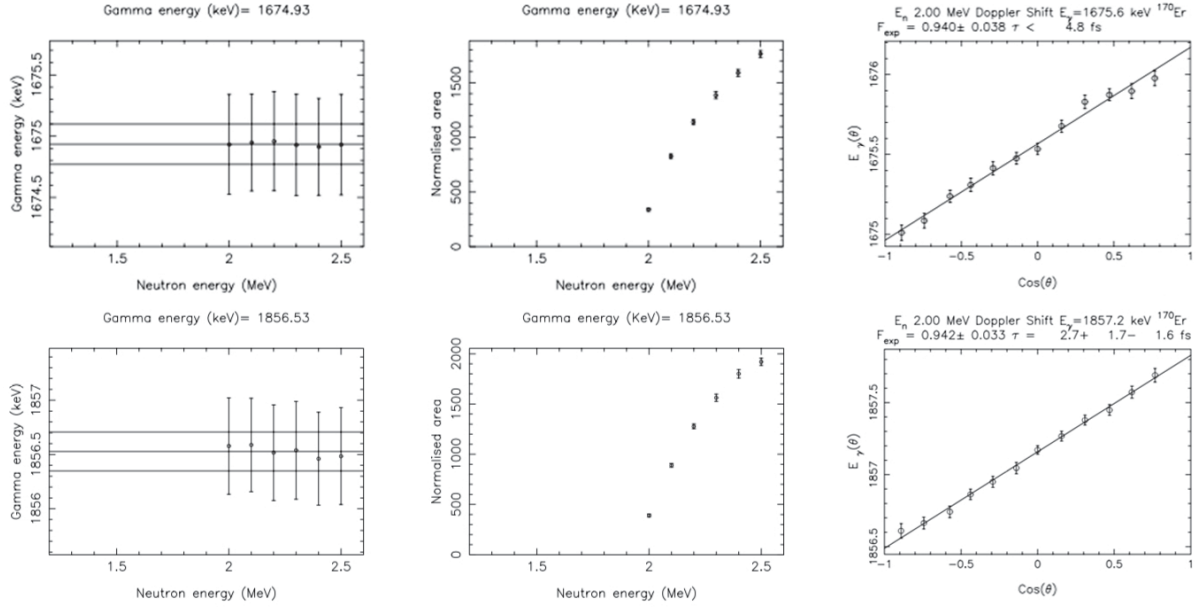


Figure 5: These are plots of the excitation function and angular doppler shift measurements for two  $\gamma$  rays leaving the 1935 ( $1^-$ ) keV level.

Table 1: Lifetimes measured using the DSAM method. The neutron energy was 2.0 MeV.

$E_{level}$	$J^\pi$	$\tau$ (fs)
1824 keV	$1^-$	$6.3^{+0.9}_{-0.9}$
1935 keV	$(3^-)$	$2.89^{+1.3}_{-1.2}$
1973 keV	$1^{(+)}$	$370^{+290}_{-120}$
890 keV	$(0^+)$	$> 804$
1324 keV	$(0^+)$	$> 1770$

Doppler shifts for the tentatively assigned  $0^+$  levels were too small to detect as shown in fig 5, so lower limits were determined for the lifetimes of these states.

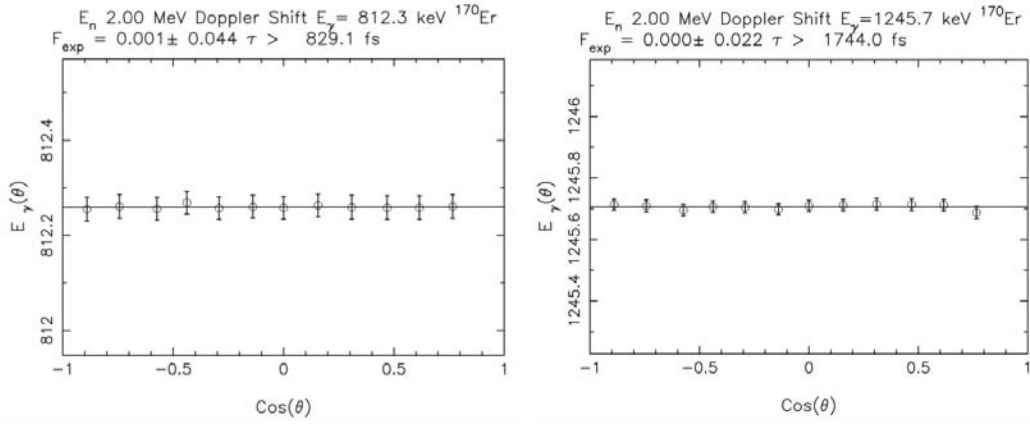


Figure 6: the doppler shift plot of the 812 keV  $\gamma$  ray that depopulates the 890 keV  $0^+$  state and the 1245 keV  $\gamma$  ray that depopulates the 1324 keV  $0^+$  state.

## 4 Analysis and Conclusions

At least three level lifetimes were in the accessible range for accurate measurement with this data set. Additional analysis of these data sets, and an additional  $E_N=2.2$  MeV angular distribution data set, will yield angular distributions, branching ratios, and additional lifetimes for  $E_N=2.0$ , 2.2, and 2.8 MeV.

Future work on this project includes using the  $0^+$   $\gamma$  ray measurements to determine lifetime measurement techniques that would be effective for lifetimes longer than the measurable range of DSAM. It is also possible that the lifetimes lie below the limits reported by the analysis programs due to the high neutron energy causing higher level feeding. In this case, performing angular measurements at 1-1.3 MeV for DSAM would be appropriate. Although additional data sets that were not analyzed for this project might be useful in identifying possible candidates for higher lying  $0^+$  states closer to the 2.0 MeV threshold, only measurements from the  $^{168}\text{Er}(t,p)^{170}\text{Er}$  transfer reaction can conclusively identify  $0^+$  states.

## References

- [1] Krane, K. S. (1988). Introductory nuclear physics. New York: John Wiley and Sons.
- [2] A. Bohr and B. Mottelson, Nuclear Structure Vol. II (W.A. Benjamin, Reading, Massachusetts, 1975).
- [3] S. R. Leshner, A. Aprahamian, L. Trache, A. Oros-Peusquens, S. Deyliz, A. Gollwitzer, R. Hertenberger, B. D. Valnion, and G. Graw, Phys. Rev. C **66**, 051305(R) (2002).
- [4] P. E. Garret, N. Warr, S. W. Yates, J. Res. Natl. Inst. Stand. Technol. 105, 141 (2000).
- [5] UKY. (n.d.). Equipment & Setups page 1. Retrieved from [www.pa.uky.edu/~marcus/setups2.html](http://www.pa.uky.edu/~marcus/setups2.html)
- [6] NNDC. (n.d.). Evaluated and Compiled Nuclear Structure Data. Retrieved from [www.nndc.bnl.gov/ensdf](http://www.nndc.bnl.gov/ensdf)

# Thymine Deposition onto Gallium Arsenide and Changes in the Surface Properties

Max Nguyen

University of Notre Dame  
Radiation Lab

July 2018

## **Abstract**

Current efforts to improve photoelectrochemical solar cells have scientists looking for a way to lengthen the lifetime of superconductors and move their band gaps to an efficient range for incident sunlight. The deposition rate of thymine onto a GaAs substrate was investigated as a function of temperature at ambient pressure as a potential solution to the challenges that photoelectrochemical solar cells face. After the deposition of a few nanometers of thymine, the surface of the substrate was analyzed by an X-Ray Photoelectron Spectroscopy to identify the change in surface chemistry. The optimum temperatures for deposition is in the range of 150 to 250°C. Any higher temperature causes thymine to solidify and clump together as well as produces a new compound. This was identified as a new peak in the infrared spectrum that correlates to carbon dioxide, which implies some damage to the thymine.

# Introduction

Solar power is rapidly gaining popularity as the best clean and renewable energy source in response to global concern about the changing climate. Despite many large advances in solar technology, there are still many obstacles with the cost of implementation and storage of surplus energy, which presents itself as the motivation of this project. Photo-electro-chemical solar cells are being studied as a source of hydrogen for usage in hydrogen fuel cells [3]. This hydrogen comes from using solar power to facilitate water splitting catalysis to create both hydrogen and oxygen gas. Deposition rates from different temperatures were studied to aid in future projects that desire to deposit various amounts of the biomolecules tested.

The frequency change of vibration within a quartz crystal was measured to calculate the thickness of deposition onto the microbalance in the chamber. The frequency change is related to the change in mass by the Sauerbrey equation

$$\Delta f = -\frac{2f_0^2}{A\rho_q\mu_q}\Delta m \quad (1)$$

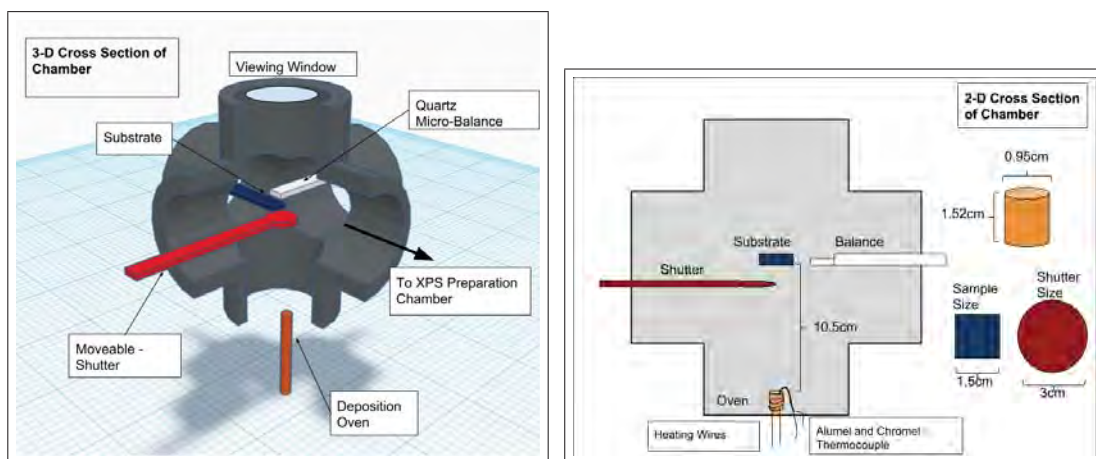
where  $\Delta f$  is the frequency change,  $f_0$  is the resonant frequency of the crystal,  $A$  is the piezoelectrically active area,  $\rho_q$  is the density of quartz,  $\mu_q$  is the shear modulus of AT cut quartz, and  $\Delta m$  is the change in mass [4]. AT cut is the most common way to cut a crystal blank from the main quartz crystal. Equation (1) gives the basis for the following equation

$$T_f = \frac{K(\Delta f)}{d_f} \quad (2)$$

where  $T_f$  is the final thickness,  $d_f$  is the density of the film deposited, and  $K$  is a constant  $= \frac{N_a t d_q}{F_q^2}$ ; where  $N_a t$  is the natural frequency of AT cut quartz,  $d_q$  is the density of quartz, and  $F_q$  is the uncoated frequency of the quartz crystal [2]. A previous study into the effects of nucleic acids on light emitting diodes found that the thermal stability of thymine began to deteriorate at roughly 270°C and conducted depositions at a temperature of 280°C in vacuum [1].

# Experimental Design

The deposition was conducted in a stainless steel chamber with six configurable outlets. Five of these outlets were fitted with maneuverable extensions into the chamber while the last one remained closed. Heating wires wrapped around the oven were connected to an external power supply with which the temperature inside the oven could be controlled by manipulating the voltage and amperage. Figures 1a and 1b illustrate the main experimental apparatus in both two and three dimensions. The exact measurements of key components of the apparatus are detailed in figure 1b. It is important to note that both the substrate or the microbalance can be centered above the oven or one can attempt to monitor deposition onto the substrate with the balance slightly off to the side at the same time. The microbalance and substrate were deposited upon separately.



(a) 3-D Diagram of Deposition Chamber (b) 2-D Diagram of Deposition Chamber

Figure 1: Diagrams of the experimental set-up

## Observations and Data

The first few tests of deposition were conducted with a low vacuum creating a pressure of about  $10^{-2}$  millibars inside the chamber. Deposition was not seen within these trials either because the rate of deposition was lower than the rate of the vacuum removing material from the chamber, or because the microbalance was placed side by side with the substrate. Instead, the change in frequency detected was a positive trend (shown in figure 2), which is the opposite direction from the expected negative trend indicating an increase in mass on the quartz crystal.

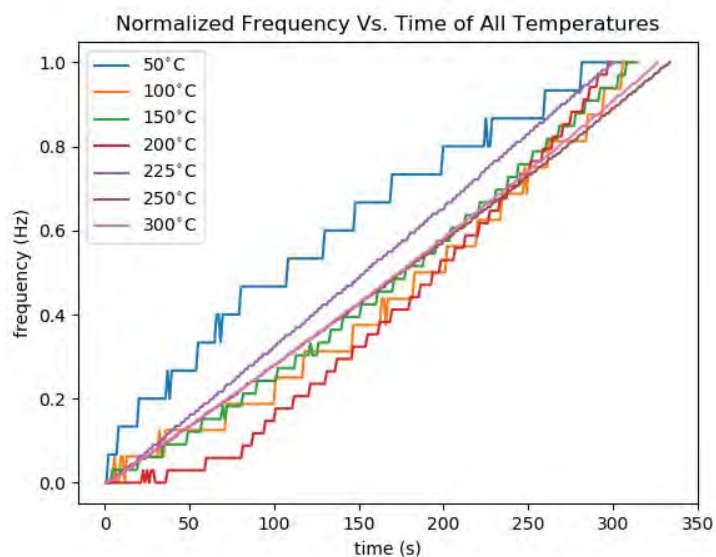


Figure 2: Graph of Initial Depositions in Weak Vacuum

The subsequent tests were conducted in ambient pressure to more clearly see the deposition, and the substrate was removed to allow the microbalance to take its place directly above the oven. A graph of the desired negative change in frequency is depicted in figure 3. The most important sections of figure 3 are the start and end of the graph as the difference between those two plateaus will give the  $\Delta f$  that is needed to calculate the thickness deposited. Currently, there is not an explanation for why the middle regions of the graph spike upwards and oscillate, but that region is not significant to this study.

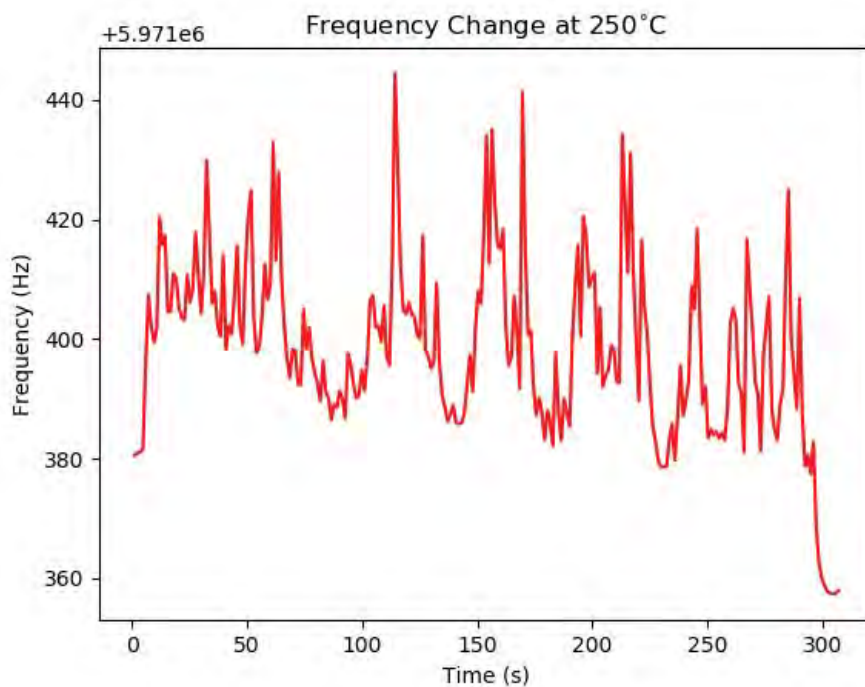


Figure 3: Representative data from one trial of deposition

The physical traits of thymine begin changing at approximately 275°C. The thymine will begin to clump together and become more difficult to deposit. A color change also begins to take place within the thymine, changing progressively from a pure white to a brown-gray color.



(a) Thymine after being heated to 275°C (b) Thymine after being heated to 300°C

Figure 4: Color Changes Observed in Thymine Sample

## Analysis

The average deposition rate was calculated by dividing the average calculated thickness for each temperature by the set deposition time of 5 minutes. These deposition rates are graphed and shown in figure 5.

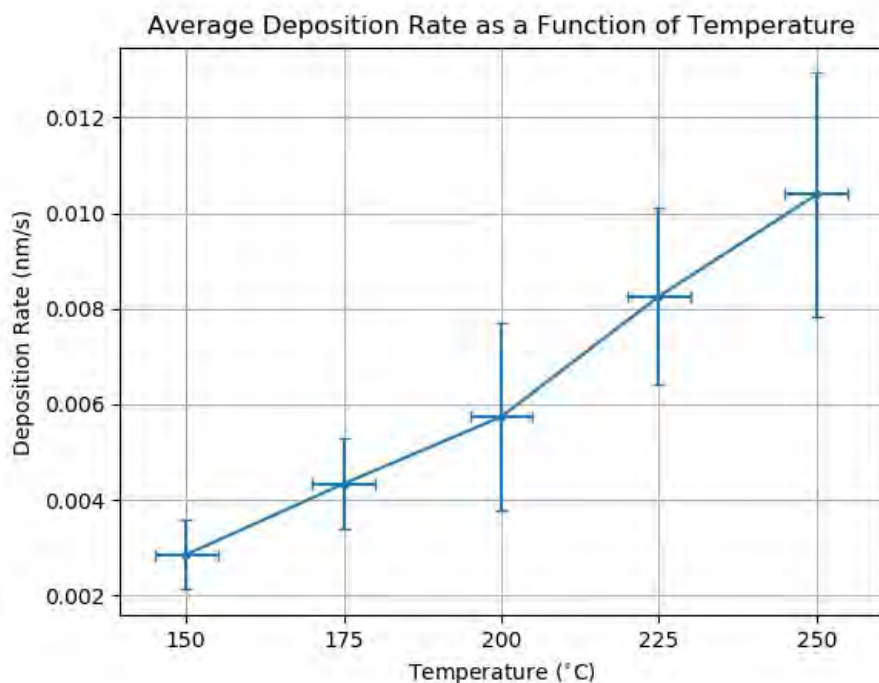


Figure 5: Trend of Deposition Rate with Increasing Temperature

The error bars on the x-axis are all  $\pm 5^{\circ}\text{C}$  as the deposition temperature oftentimes was rising while the trial took place. Therefore, the shutter was removed at a lower temperature to attempt an average temperature close to the one displayed on the graph. The y-axis error bars represent the standard deviation calculated from three trials at each temperature. These bars are large likely due to the small sample size as well as the low magnitude of the values. The overall trend of the rate versus temperature is linear, which is useful for predicting deposition rates at untested temperatures.

Pure thymine is characterized in by two peaks between  $1750$  and  $1600\text{cm}^{-1}$ . The spectra in figure 6, shows a change in the thymine spectrum occurring at approximately the  $275^\circ\text{C}$  mark with a new peak forming at around a wave number of  $2400\text{cm}^{-1}$ . This is consistent with the temperatures at which the changes in color were observed, so one can be relatively safe in assuming their thymine sample is compromised after a change in color is observed. One previous study has categorized this new peak at  $2360\text{cm}^{-1}$  to be corresponding to a carbon-oxygen double bond [5], which is found in carbon dioxide. The IR peak associated with carbon dioxide was then matched with the peak to confirm this change. This production is not surprising as it is common to create carbon dioxide when burning organic compounds.

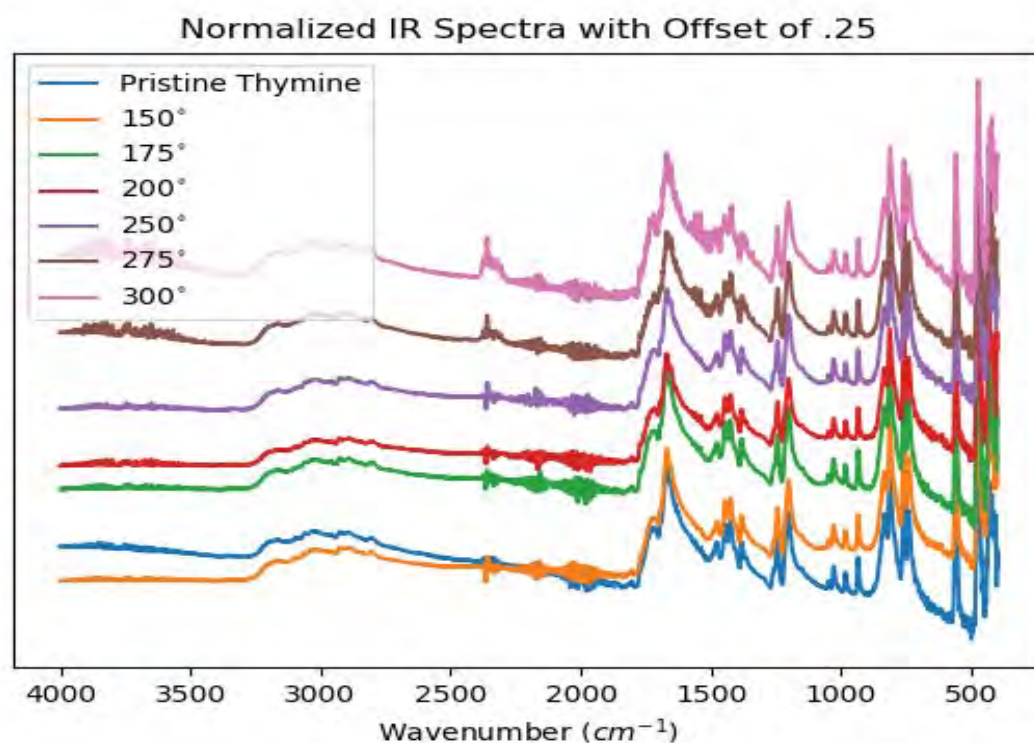


Figure 6: The normalized spectra of heated thymine samples. The order of heating is increasing from bottom to top, with  $300^\circ\text{C}$  being at the top.

<b>Integrated Area Under Peaks</b>		
Elemental Peak	Before Deposition	After Deposition
Carbon	1380.7	2784.3
Gallium	14,299.5	9912.7
Arsenic	3609.8	1870.6

Table 1: Table showing the change in integrated intensity of the elemental peaks before and after deposition of thymine.

The first substrate analyzed in the XPS was deposited upon for 5 minutes at 150°C. There was no notable change in the spectrum for this substrate. The second substrate analyzed in the XPS was deposited upon for 15 minutes at 175°C. This substrate shows significant change in the gallium peak regions as well as the arsenic peak regions as seen in table 1. The gallium peaks were diminished after the deposition, which can be interpreted as a new layer of thymine obscuring the surface of the substrate. The gallium-arsenic bond peak that was previously seen on the surface completely disappeared from the spectrum in the gallium 2p orbital (Figure 7). An increase in the intensity of the carbon peak was observed, which could have come from the thymine, but a major concern that was faced in the analysis of this substrate was that it was exposed to the atmosphere during the transfer from the deposition chamber to the analysis chamber. As such, it becomes difficult to predict whether some of these changes in the spectra are coming from thymine or contamination from the atmosphere.

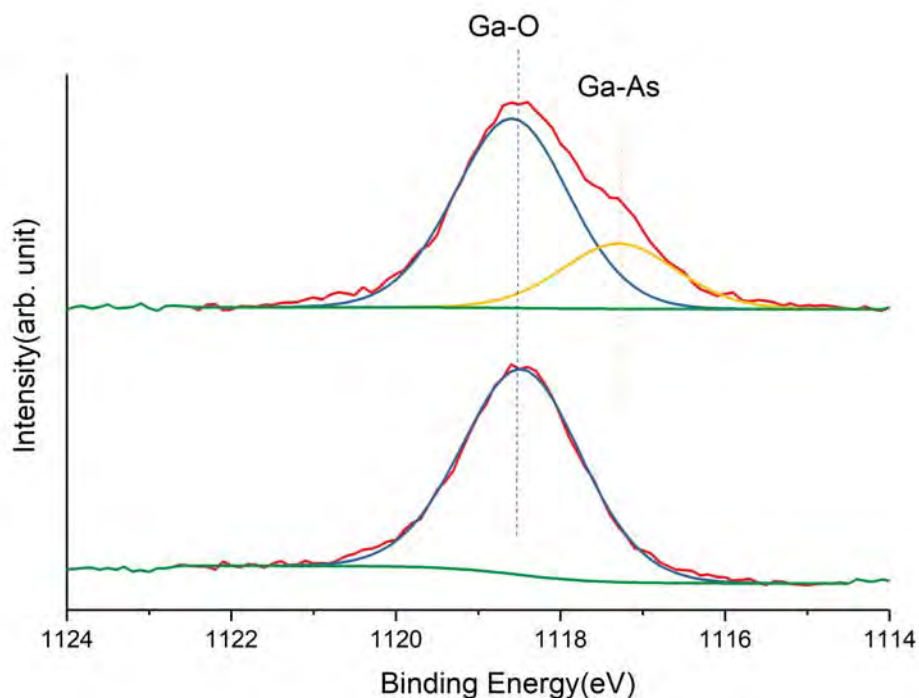


Figure 7: Gallium 2p peaks before and after deposition

## Discussion

While the precision of deposition found in this project was not high, it is still accurate enough to form mono-layers. This first layer of interaction is the most important to achieve in order to affect electronic properties of the substrate. It is recommended keep the range of temperature between 150°C and 250°C when depositing thymine using this method to preserve the integrity of the thymine sample. Further testing with thymine will require doing the entire deposition and analysis process in vacuum in order to more definitively identify the exact effects that thymine has on gallium arsenide. The next molecule to be tested will be uracil. It can be reasoned that uracil will be similar to thymine as they are closely related in their function in DNA and RNA, so it is a logical continuation of this project.

## Acknowledgements

I would like to thank my advisor, Sylwia Ptasińska, for overseeing this project. I would also like to thank Pitambar Sapkota, Amal Sebastian, and Soumya Banerjee in the XPS group with helping me to collect and interpret data. I am very grateful for the funding that I received for this project from the Department of Energy. Lastly, I would like to thank the Notre Dame REU program for allowing me to present this project and its findings.

## References

- [1] E. F. Gomez, V. Venkatraman, J. G. Grote, and A. J. Steckl. Exploring the Potential of Nucleic Acid Bases in Organic Light Emitting Diodes. *Adv. Mater. Weinheim*, 27(46):7552–7562, Dec 2015.
- [2] Inficon. Sqm-160 thickness monitor operation manual, 2015.
- [3] E. L. Miller. Photoelectrochemical water splitting, Sep 2015.
- [4] Günter Sauerbrey. Verwendung von schwingquarzen zur wägung dünner schichten und zur mikrowägung”. *Zeitschrift für Physik*, 155(2):206–222, Apr 1959.
- [5] Feng Yang, Meilian Zhao, Baozhan Zheng, Dan Xiao, Li Wu, and Yong Guo. Influence of ph on the fluorescence properties of graphene quantum dots using ozonation pre-oxide hydrothermal synthesis. *J. Mater. Chem.*, 22:25471–25479, 2012.

# A systematic study of GaMnAsP-based magnetic tunnel junctions

---

Moses Nnaji

2018 NSF/REU program

University of Notre Dame, Department of Physics

July 27, 2018

Advisors:

Prof. Xinyu Liu, Prof. Jacek Furdyna

## **Abstract**

While the development of room temperature ferromagnetic semiconductors continues, efforts are being made on how to properly incorporate these materials into existing technology once they are realized. One aspect is the optimization of magnetic tunnel junctions (MTJ) for use in current and future magnetic random-access memory (MRAM) technology. Such a system can be implemented by use of GaMnAsP layers, where attempts are made to align the out-of-plane magnetization for each layer. In this study, GaMnAsP/GaAs:Be trilayer samples were produced via molecular beam epitaxy (MBE), annealed, and then analyzed via superconducting quantum interference device (SQUID) magnetometry. Magnetic properties of the ferromagnetic layers, such as the Curie temperatures and magnetic alignment were observed; from this, the tunnel magnetoresistance (TMR) behavior can be elucidated.

Key words: GaMnAs, magnetic tunnel junction, magnetization alignment, tunnel magnetoresistance

## **I. Introduction**

The development of a ferromagnetic semiconductor that exhibits ferromagnetic behavior near and above 300 K is attractive for the development of practical spin field effect transistors (spinFETs). Unlike traditional transistor devices such as metal oxide semiconductor field-effect transistors (MOSFETs), the spin states of the electrons relative to one another serve as the transfer of information. The successful implementation of such a device would create transistors that are smaller, more efficient, and less energy-dependent, implicating major improvements of electronic storage devices. The development of spintronic systems is largely dependent on the optimization of diluted magnetic semiconductors (DMSs) - GaMnAs is an excellent candidate since GaAs has

enjoyed implementation in a variety of applications, meaning that GaMnAs will be easier to integrate into current technology.

The development of magnetic random-access memory (MRAM) is one prospect of new DMS technology. In particular, the development of perpendicular magnetic tunnel junctions (pMTJs) is important for the refinement of these spintronic materials in MRAM devices [figure 1]. Notably, the integration of P into GaMnAs encourages a change in magnetic anisotropy of the ferromagnetic layers towards an out-of-plane direction. This study features GaMnAsP/GaAs:Be trilayer fragments intended to simulate pMTJs being designed for new MRAM technology - one paramagnetic layer of GaAsBe is sandwiched between two layers of ferromagnetic GaMnAsP. These samples were created by use of MBE and measured via SQUID magnetometer to characterize their magnetization.

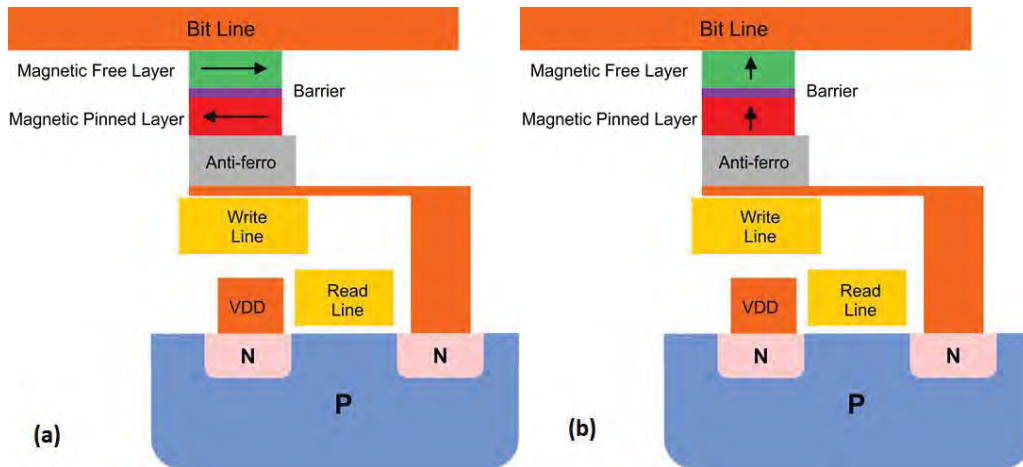


**Figure 1:** Schematic of MRAM cells. (a) The MTJ section represents a bit, where parallel and antiparallel configurations represent 0 and 1, respectively. The top layer of the MTJ can change magnetic orientation, while the bottom layer is fixed. (b) An alternate magnetic configuration of the MTJ that could permit higher density MRAM (Zhu & Park, 2006).

## II. SQUID Magnetometer

The Superconductive quantum interference device (SQUID) is a type of magnetometer that is capable of detecting very small magnetic fields. The SQUID apparatus functions by utilizing Josephson junctions that exhibit the dc Josephson effect, where electron (cooper pair) tunneling across a superconductor-nonsuperconductor-superconductor junction occurs in the absence of an external electric field, creating a tunneling current [figure 2].

When two Josephson junctions are paired to form a superconducting ring, the tunneling current splits equally into two paths. The application of an external magnetic field causes the current traveling through each path to become unequal; when the current is high enough, a voltage across the junctions will appear (Clark & Braginski, 2004). If the external magnetic flux does not exceed half the magnetic flux quantum,  $\frac{\Phi_0}{2}$ , the induced current will cancel out the applied flux. However, if the flux exceeds this value, then the total flux favorably increases to  $\Phi_0$  instead of zero, causing the induced current to reverse direction. Essentially, as the magnetic field continues to increase, the current oscillates between constructive and destructive interference behavior as it convenes at the end of the loop due to a phase difference between the cooper pairs in the paths. The number of the resulting voltage oscillations observed can be counted to determine the total magnetic flux that has occurred (Clark & Braginski, 2004).

The SQUID magnetometer used in this study utilizes a superconductive wire that coils to form a four-ring detector and is surrounded by superconducting magnets. The samples are mounted in a straw and then moved at various positions within the coil. A current is induced from the magnetic moment of the sample and processed through a flux antenna into a SQUID ring [figure 2]. This study features the Magnetic Property Measurement System (MPMS) model XL. In this system, superconducting magnets are capable of providing a uniform magnetic field of -7.0 to 7.0

Tesla with a 0.1 Gauss resolution, and the configuration of the coils allows them to shield the sample from the superconducting magnets, controlling the exposure with a precision of roughly 0.1%. The SQUID apparatus is kept cool at around temperatures of 2-5 K and can reach up to 400 K when measuring samples. Therefore, the device is suitable for measuring magnetization of small samples at a variety of temperatures and magnetic fields; it is capable of detecting magnetic fields as low as  $10^{-9}$  emu (Quantum Design, 2011).

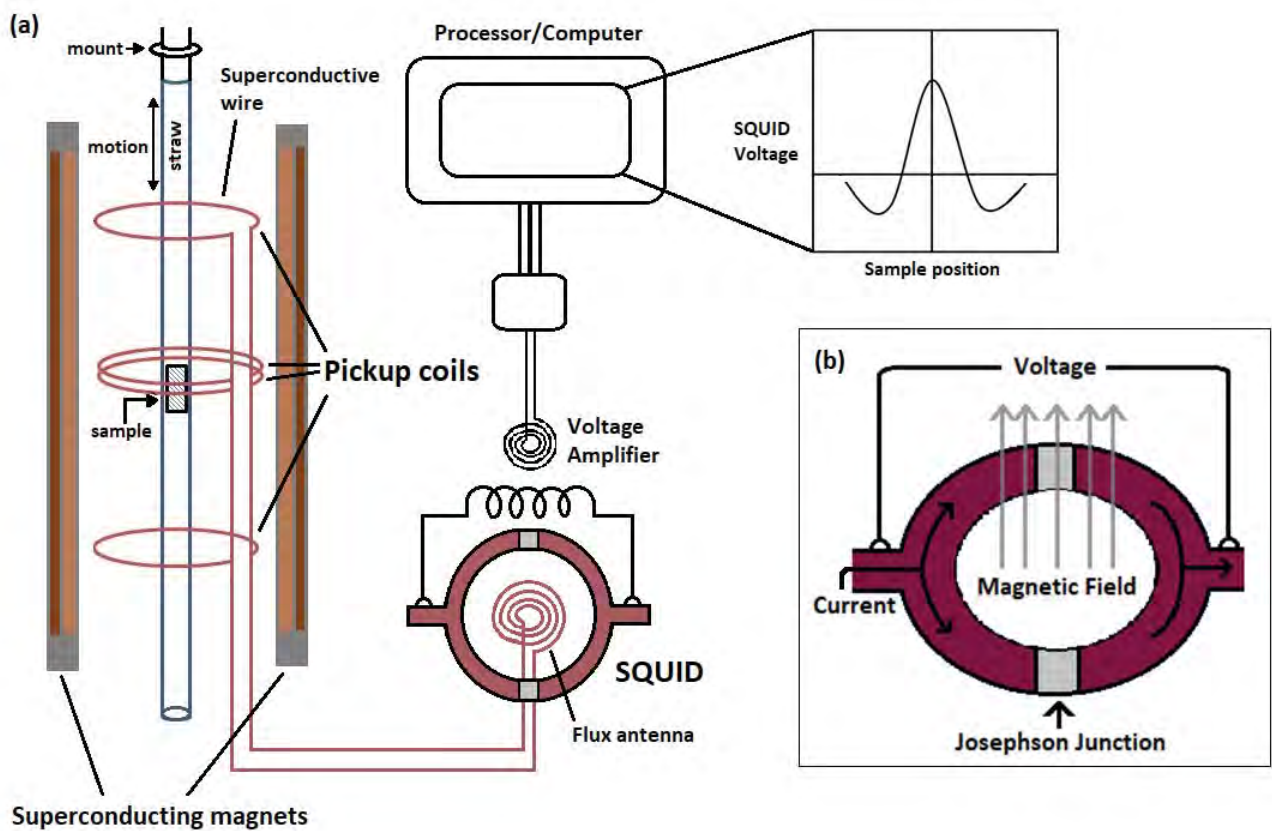


**Figure 2:** (a) Illustration of a SQUID magnetometer apparatus. Movement of the sample in the z-direction induces fluctuations in voltage. (b) Implementation of Josephson junctions in the SQUID.

### III. MBE growth process

The creation of GaMnAsP/GaAsBe trilayer samples required the use of the molecular beam epitaxy (MBE), where a crystalline structure is grown by a layer-by-layer mode at roughly one

layer per second. During MBE, various elements are contained within effusion cells and are heated up to several hundred °C, depending on the element. The resulting vapors are collimated into a beam and deposited onto a crystalline substrate which is heated to a few hundred °C [figure 3]. A reflection high energy electron deflection (RHEED) gun is pointed at the sample, where a portion of electrons is diffracted and collides into a photoluminescent detector screen, where the diffraction pattern is dependent on the surface height of the sample. Thus, RHEED is used in tandem with MBE in order to monitor the development of sample (Arthur, 2002).

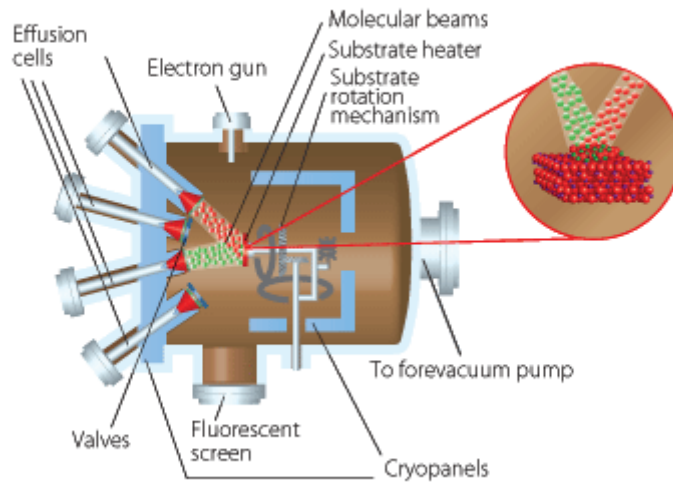


**Figure 3:** Illustration of the MBE apparatus.

In order to achieve greater purity, the MBE process is enclosed in an ultra-vacuum chamber. For diluted magnetic semiconductors, a small concentration of a magnetic dopant (such as  $\text{Mn}^{2+}$  ions) is integrated into the semiconductor. In the formation of  $\text{Ga}_{1-x}\text{Mn}_x\text{As}_{1-y}\text{P}_y$ , the Mn ions ( $x = 0.01-0.05$ ) replace a fraction of the Ga atoms, whereas the P ions ( $y = 0.10-0.30$ ) replace some of the As atoms.

#### **IV. Experimental Setup**

Initially, 3 GaMnAsP trilayer samples were prepared by use of MBE onto pre-prepared GaAs (100) semi-insulating substrates attached to a sample holder by Indium. These samples were grown to total thicknesses of 62, 65, and 75 nm. Once removed from the MBE apparatus, the samples were scrubbed with sandpaper to remove the Indium residue on the backside, and then rinsed with methanol. The samples were then measured and placed into the SQUID apparatus (via plastic straws) in order to measure their magnetization. Once the magnetization of these samples was measured, a secondary piece of each sample (with identical thickness) was annealed at 273 °C for an hour. The annealed samples were then placed into the SQUID apparatus after scrubbing and cleaning for a second round of measurements. All measurements made by the SQUID machine were processed and sent to computer for further processing and data analysis via OriginPro software.

All 6 samples possessed different structural dimensions. Each sample featured a 50 nm thick “bottom” layer of GaMnAsP and a 5 nm GaAs:Be middle layer - the differences between the samples arose from the “top” layer of GaMnAsP, having a thickness of 7 nm, 10 nm, or 20 nm. During magnetization measurements, the SQUID magnetometer subjected all GaMnAsP/GaAs:Be samples to a 2000 Gauss loop and an incremental increase in temperature, from to 5 K to 150 K.

#### **V. Results**

In each of the 6 samples, the magnetization of the samples decreases significantly as the temperature increases. The observed Curie temperatures ranged from 30 K to roughly 50 K, and these temperatures were consistently higher in the annealed samples [figure 4]. Magnetization measured as a result of the magnetic field occurred mostly within the -500 to 500 Gauss range. In

the hysteretic loops, either two or four distinct magnetic orientations can be observed, depending on the sample - these magnetic moments were much more clearly defined in the annealed samples than in the as-grown samples [figure 5]. Overall, the annealed samples produced more satisfactory data.

In addition to a background magnetic field of 2-3 G, some diamagnetic interference from the GaAs (100) substrates was observed. The data corresponding to temperatures that exceeded the Curie temperatures of the samples represented this interference and was used to correct data that corresponded to the actual magnetization of the samples.

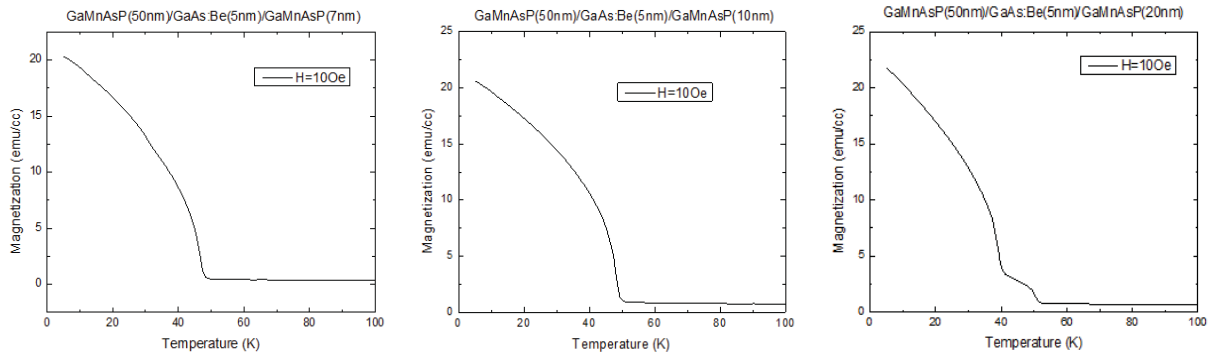


**Figure 4:** Graphs of the annealed samples illustrating the dependence of their magnetic moment on temperature under a field of 10 Gauss. The Curie temperatures are indicated where the magnetization flatlines.

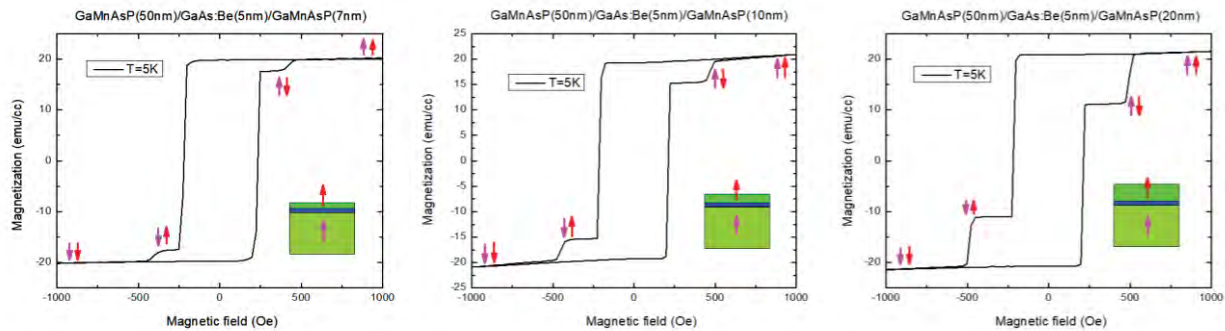


**Figure 5:** Hysteretic loops showing the magnetization of the annealed samples due to the external magnetic field. The four distinct magnetic states due to the two magnetic layers of the samples are indicated by the arrows (up-up, down-down, up-down, and down-up). It can be seen that the amount of magnetization is correlated to layer thickness, where the top layer exerts more magnetic influence as it becomes thicker.

## **VI. Discussion**

The incorporation of P influences the axis of magnetization within the GaMnAsP layers. P atoms are chemically similar enough to As atoms in order to replace them in significant concentration. However, the P atoms are smaller than the As atoms, causing the lattice structure of crystal to stretch to compensate. The resulting tensile strain and warping of the crystal structure causes the magneto-crystalline anisotropy to shift from in-plane magnetization to out-of-plane magnetization, provided that the concentration of P atoms is high enough. It is also worth noting that, if the difference in thickness between the two layers is large enough, the larger layer will force the thinner layer to have similarly-oriented magnetization (Zhu & Park, 2006). However, during data analysis, this coupling effect was not observed to any appreciable extent.

In any case, our experiment provides information that would allow the tunnel magnetoresistance (TMR) of these samples to be measured. TMR measurements are valuable because they are an indicator of the alignment of the magnetization in the ferromagnetic layers (Yoo et al., 2013). The development of perpendicular magnetization in MTJs is particularly important because it suggests a path to the reduction of size in MRAM products. Since the magnitude of in-plane magnetization is determined by the dimensions of the layers, size affects the switching threshold and ultimately limits the scalability of the MTJ in the MRAM cell - this restriction is not believed to be posed by out-of-plane magnetization (Zhu & Park, 2006). It follows that the magnetization of the layers should be as aligned as possible.

## **VII. Conclusion**

This study resulted in the characterization of the magnetization magnitude and orientation in several different GaMnAsP-based magnetic tunnel junctions. It portrays the successful integration of P into GaMnAs to produce ferromagnetic layers with distinct magnetization in the

out-of-plane direction. Hopefully, similar experiments using GaMnAs will achieve strong magnetic alignment between the ferromagnetic layers in the out-of-plane direction, and consequently, higher TMR values that are desirable for higher-density MRAM devices.

## **Acknowledgements**

I would like to thank Prof. Liu and Prof. Furdyna for their guidance and expertise throughout the duration of this study. I would also like to thank Prof. Garg, the ND Physics dept., and NSF for providing the arrangements and funding necessary for me to engage in research at the University of Notre Dame.

## **References**

- J. Clarke, & A. I. Braginski (2004). *The SQUID handbook* (Vol. 1), p. 1-11. Weinheim: Wiley-VCH.
- J. R. Arthur (2002). Molecular beam epitaxy. *Surface Science*, 500(1-3), 189-217.
- J. Zhu, & C. Park. (2006). Magnetic tunnel junctions. *Materials Today*, 9(11), 36-45.
- Quantum Design. (2011). *Magnetic Property Measurement System – MPMS®-XL* [Brochure].
- T. Yoo, S. Khym, S. Lee, X. Liu, J. K. Furdyna, D. U. Lee, & E. K. Kim (2013). Tunneling magnetoresistance from non-collinear alignment of magnetization in Fe/GaAlAs/GaMnAs magnetic tunnel junctions. *Applied Physics Letters*, 102(21), 212404.

# Truncation of Ab Initio Nuclear Interactions

Robert J. Power

2018 NSF/REU Program

Physics Department, University of Notre Dame

Advisors: Prof. Mark A. Caprio<sup>[1]</sup>, Dr. Anna E. McCoy<sup>[2]</sup>

<sup>1</sup>Department of Physics, University of Notre Dame, Notre Dame, Indiana 46556-5670, USA

<sup>2</sup>TRIUMF, 4004 Wesbrook Mall, Vancouver, British Columbia, V6T 2A3, Canada

## Abstract

Predicting nuclear structure from the nucleon-nucleon interaction has been a long standing goal in nuclear theory. The accuracy of these predictions depends on the interaction and the method used to solve the nuclear Hamiltonian eigenvalue problem. Accurate numerical solutions to this problem require computational resources beyond the current capacity of super-computers for nuclei other than light nuclei. We aim to reduce the necessary computational resources by truncating the nuclear interaction based on approximate symmetries of the nuclear system. As a first step towards this goal, various truncations were applied to the JISP16 interaction. These truncated interactions were used to calculate the ground state energies of  $^3\text{He}$  and  $^6\text{Li}$  obtained using the no-core configuration interaction (NCCI) framework. The calculated results were compared with those obtained using the original interaction.

## 1 Introduction

Calculating the nuclear observables from inter-nucleon interactions requires a large amount of computational resources. We use ab initio no-core configuration interaction (NCCI) methods [1–5] to calculate the nuclear observables, e.g. binding energies of nuclei, by constructing a nuclear Hamiltonian matrix in a configuration basis, and then solving the Hamiltonian matrix eigenvalue problem to get the energies (eigenvalues of the Hamiltonian) and the nuclear wavefunctions (eigenstates of the Hamiltonian). Traditionally the harmonic oscillator basis is used.

However, the harmonic oscillator basis is an infinite dimensional basis and therefore must be truncated. This truncation must leave a basis large enough to obtain predictions of observables within a desired accuracy. But as the number of nucleons increases calculations of nuclear observables become challenging due to the size of the basis necessary to obtain accurate results.

The symplectic no-core configuration interaction (SpNCCI) [6] framework seeks to reduce the necessary basis size by carrying out calculations in an  $\text{Sp}(3, \mathbb{R})$  symplectic basis. This makes it possible to apply symmetry based truncations to the many-body basis. This has the potential to

drastically reduce the basis size. The trade-off of this new method is a significant increase in the computational complexity of constructing the Hamiltonian matrix.

A possible means of reducing the computational cost of constructing the Hamiltonian matrix in the symplectic basis is to truncate the nuclear interaction itself. We use the different approximate and exact symmetries of the nuclear Hamiltonian to identify and remove specific components of the interaction. These components fail to contribute to the calculation of observables to more than our desired level of accuracy.

To study the effect of these truncations, they were applied to the J-matrix inverse scattering potential (JISP16) interaction [7] and used to calculate the ground state energy of  $^3\text{He}$  and  $^6\text{Li}$  in the NCCI framework using the well established MFDn code [8, 9]. JISP16 is a nucleon-nucleon interaction which is used in the description of light nuclei and was fit to nucleon-nucleon scattering data and deuteron properties. The extent of the truncation is measured by the proportion of components retained and its effect is the error in resulting observables compared to an untruncated result.

In section 2 we will review the primary concepts in the NCCI framework. In section 3 the truncation schemes implemented in this report are defined. Section 4 will study the effects on the nuclear energies of these truncated schemes applied to the JISP16 interaction.

## 2 Review of NCCI framework

The ab initio no core shell configuration (NCCI) framework [1–5] uses realistic nucleon-nucleon interactions to predict the properties of light nuclei. The Hamiltonian is given by

$$\hat{H} = \hat{T} + \sum_{\substack{ij \\ i \neq j}}^A \hat{V}_{NN}(\vec{r}_i - \vec{r}_j). \quad (1)$$

The Hamiltonian matrix is constructed in a configuration basis composed of antisymmetric product states (Slater determinants) that traditionally involve single particle harmonic oscillator states from many major shells. This harmonic oscillator basis contains configurations that are

distributions of nucleons over single particle harmonic oscillator eigenstates, which are described by the quantum numbers  $(nljm)$ , where  $n$  is the radial quantum number,  $l$  is the orbital angular momentum,  $j$  is the angular momentum and  $m$  is the projection of  $j$ . The eigenstates are grouped into major harmonic oscillator shells which are associated with the number of oscillator quanta  $N = 2n + l$ .

The harmonic oscillator basis must be truncated.  $N_{\max}$  truncation truncates the total number of oscillator quanta. The number of oscillator quanta  $N$  is the sum of the oscillator quanta of each occupied single particle orbit  $N_i = 2n_i + l_i$  so  $N = \sum_{i=1}^A N_i$ . This can be written as  $N = N_0 + N_{\text{ex}}$  where  $N_0$  is the number of quanta in the lowest Pauli-allowed configuration and  $N_{\text{ex}}$  is the number of excited quanta.  $N_{\max}$  truncation limits the basis to configurations with  $N_{\text{ex}} \leq N_{\max}$ .

The nucleon-nucleon interaction is a function of the separation between two particles. Thus, it is often represented in terms of its matrix elements in the relative harmonic oscillator basis. Like the Hamiltonian the two-body harmonic oscillator basis can be factored into relative and center-of-mass parts. The relative harmonic oscillator basis is labeled by  $\{|N_{\text{rel}}LSJM_JTM_T\rangle\}$  where  $N_{\text{rel}}$  is given by the equation  $N = N_{\text{cm}} + N_{\text{rel}}$ ,  $S$  is the spin and  $T$  is the isospin.

For calculations in the NCCI framework, the matrix elements of the interaction must be converted to matrix elements on the two-body single particle basis. This is done by first coupling the relative states to the center of mass excitations. We can use the Talmi-Moshinsky transformation [10, 11] to relate the relative-center-of-mass basis to the two body single particle basis.

Expressing  $V_{\text{rel}}$  in terms of the relative harmonic oscillator basis matrix elements is equivalent to writing the relative interaction in terms of SU(2) unit tensor components as follows

$$V = \sum_{ab} \langle a || V^{J_0} || b \rangle \mathcal{U}^{J_0}(a, b), \quad (2)$$

where  $a = (N_{\text{rel},a}L_aS_aJ_aT_a)$  and  $b = (N_{\text{rel},b}L_bS_bJ_bT_b)$ . A unit tensor  $\mathcal{U}^c(a, b)$  is defined by having a single unit reduced matrix element (RME)  $\langle a || \mathcal{U}^c(a, b) || b \rangle$  and all other RMEs are zero in a given basis.

For SpNCCI we want to express the interaction in terms of  $SU(3) \times SU(2) \times SU(2)$ . This then

allows us to make use of group theory machinery like the Wigner-Eckart theorem which allows us to write matrix elements as a product of a reduced matrix element (RME) and Clebsch-Gordan coefficients. This means we are only required to calculate the RMEs once and then apply the Wigner-Eckart theorem to get the full set of corresponding matrix elements. The SU(3) group is given by the quantum numbers  $(\lambda_0, \mu_0)$ . The spin and isospin symmetries can be described by SU(2) groups. To this end, we apply a method known as upcoupling [6] to write the interaction in terms of SU(3)×SU(2)×SU(2) unit tensors as

$$V_{J_0} = \sum_{\substack{(\lambda_0, \mu_0) S_0 T_0 \\ \kappa_0 L_0 J_0}} \sum_{\substack{N' S' T' \\ NST}} \langle N' S' T' \| V^{(\lambda_0, \mu_0) S_0 T_0: \kappa_0 L_0} \| NST \rangle \mathcal{U}_{\kappa_0 L_0 J_0}^{(\lambda_0, \mu_0) S_0 T_0} (N' S' T', NST), \quad (3)$$

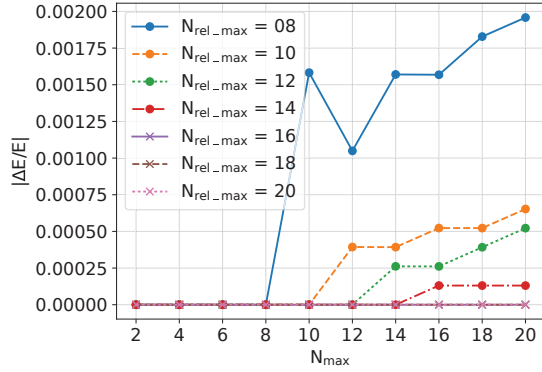
where  $(\lambda_0, \mu_0)$  is the SU(3) operator labels,  $S_0$  is the operator spin,  $T_0$  is the operator isospin and  $(\kappa_0, L_0)$  is the running index tied to the multiplicity of SU(3).  $N_0$  is defined by the equality  $N_0 = N' - N$  which, because of SU(3) coupling rules, implies that  $N_0 = \lambda_0 - \mu_0$ .

### 3 NCCI Interaction Truncation Schemes

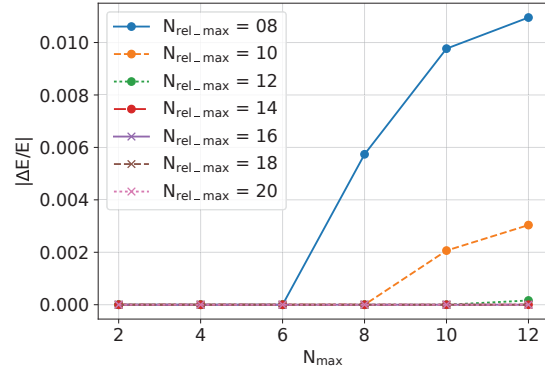
The truncation schemes implemented in this report eliminate specific components of the interaction. This is done by setting RMEs in equation (3) to zero. We eliminate components based on their oscillator quanta and SU(3) symmetries. Three different truncation schemes were applied to the JISP16 interaction.

The first truncation,  $N_{\text{rel,max}}$  truncation, is a truncation on the number of oscillator quanta carried by the relative basis state of both the bra and ket. It restricts the interaction to unit tensor components that satisfy the equality  $\max(N', N) \leq N_{\text{rel,max}}$ . Any RMEs that do not satisfy this equality are set to zero, removing the corresponding components of the interaction.

The second truncation,  $(\lambda_0, \mu_0)$  truncation, is restricting the allowed SU(3) tensor components of the interaction. The SU(3) quantum numbers of an operator  $(\lambda_0, \mu_0)$  are related to the oscillator numbers by  $(N, 0) \times (0, N') \rightarrow (\lambda_0, \mu_0)$ . Allowed unit tensor components are those where the equality  $\max(\lambda_0, \mu_0) \leq (\lambda_0, \mu_0)_{\text{max}}$  was satisfied. All RMEs that did not satisfy this relation were



(a)  ${}^3\text{He}$  untruncated  $E = -7.660$  Mev



(b)  ${}^6\text{Li}$  untruncated  $E = -30.951$  MeV

Figure 1: Comparison of fractional error of the calculated ground state energy of  ${}^3\text{He}$  and  ${}^6\text{Li}$  values for different values of  $N_{\text{rel,max}}$  as a function of  $N_{\text{max}}$  with  $\hbar\omega = 20$ .

set to zero.

In the final truncation,  $N_{0,\text{max}}$  truncation, the oscillator constant of the operator was restricted so that the equality  $|N_0| \leq N_{0,\text{max}}$  was satisfied. Similarly any RME that did not satisfy this equality was set to zero.

## 4 Effect of Truncations on Nuclear Energy

We will look at the error that gets introduced in the calculated energy when the interaction is truncated. The fractional error of the calculated energy is defined as the absolute difference between the energy calculated with the truncated interaction at a specific  $N_{\text{max}}$  value and the energy calculated with untruncated interactions for the same  $N_{\text{max}}$  value, divided by the energy calculated with the untruncated interaction.

First, we will look at  $N_{\text{rel,max}}$  truncation. Each curve in Figure 1 corresponds to a different value of  $N_{\text{rel,max}}$ . We observe that as the value of  $N_{\text{rel,max}}$  decreases the fractional error of the calculated energy increases for each  $N_{\text{max}}$  truncation. It is evident from Figure 1 that  $N_{\text{rel,max}}$  truncation has no effect on the value of the observable when  $N_{\text{max}} + 2N_v \leq N_{\text{rel,max}}$ , where  $N_v$  is the number of valence shell quanta. An  $N_{\text{rel,max}}$  truncation above  $N_{\text{max}} + 2N_v$  only eliminates RMEs involving pairs of nucleons which are too highly excited to appear in the configurations allowed by the  $N_{\text{max}}$

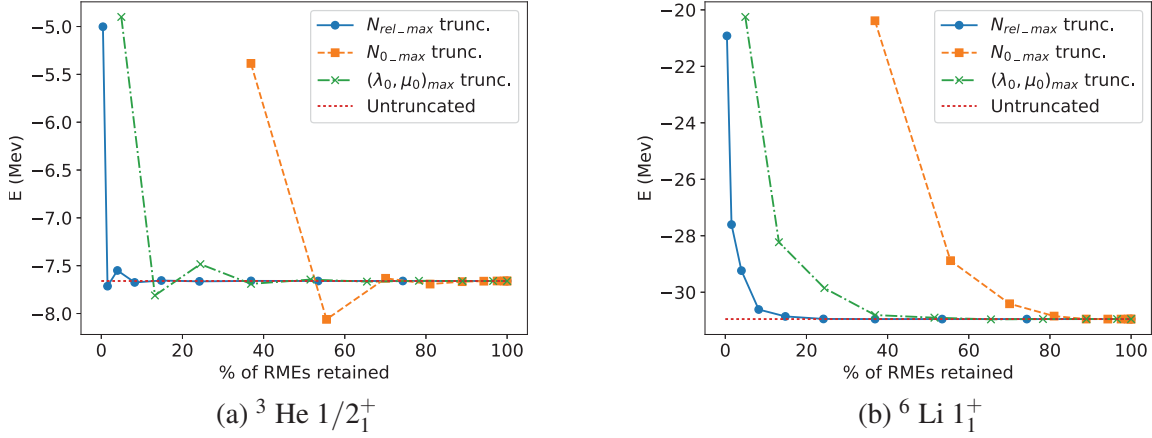


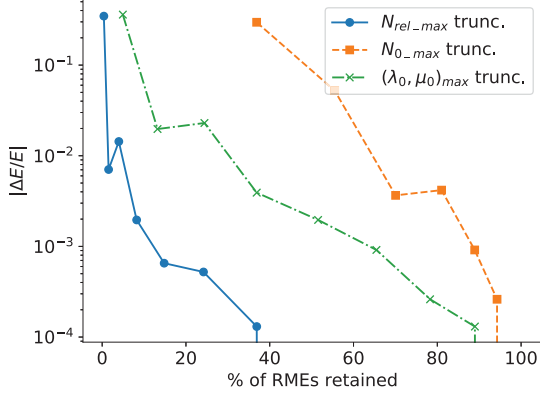
Figure 2: Convergence of ground state energy ( $E$ ) for  ${}^3\text{He}$  and  ${}^6\text{Li}$  as a function of reduced matrix elements retained after truncation using JISP16 interaction at  $N_{\max} = 20$  and  $\hbar\omega = 20$ .

truncation. This is due to  $N_{\max}$  truncation restricting the number of excitation quanta of the system and therefore, indirectly, the maximum number of excitation quanta in the relative motion of any particular pair of particles.

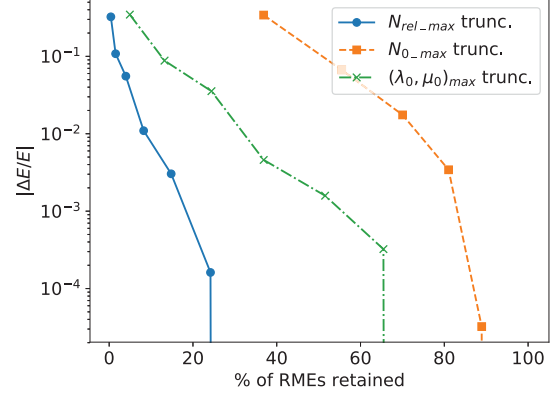
The effect of the additional  $N_v$  can be seen in the case of  ${}^6\text{Li}$  where the errors in the energy begin at  $N_{\max} + 2N_v = N_{rel,max}$ , where  $N_v = 1$  in the case of  ${}^6\text{Li}$ , compared to  ${}^3\text{He}$  which begins to diverge at  $N_{\max} = N_{max}$ . For values of  $N_{rel,max} \geq 16$ , the error in the calculated energy is below the order of keV, which is the accuracy of the method used to calculate this value.

Figure 2 shows a comparison of the convergence rate for  $N_{rel,max}$ ,  $N_{0,max}$  and  $(\lambda_0, \mu_0)_{max}$  truncations as a function of the percent of RMEs retained when calculating the ground state energy of both  ${}^3\text{He}$  and  ${}^6\text{Li}$ . The percent of RMEs retained is determined by the difference between the total number of RMEs in the original interaction and the number of RMEs in the truncated interaction, divided by the number of RMEs in the original interaction.

The three schemes all converge to the exact value of energy as the fraction of retained RMEs is increased towards unity. The dependence of the calculated energy with  $(\lambda_0, \mu_0)_{max}$  and  $N_{0,max}$  truncations is similar to that of  $N_{rel,max}$  discussed above. Both the  $N_{rel,max}$  truncation and the  $(\lambda_0, \mu_0)_{max}$  truncations converge to the exact energy with increasing percentage of RMEs retained faster than  $N_{0,max}$ .



(a)  ${}^3\text{He}$  untruncated  $E = -7.660$  MeV



(b)  ${}^6\text{Li}$  untruncated  $E = -30.951$  MeV

Figure 3: Plot of fractional error of the ground state energy for  ${}^3\text{He}$  and  ${}^6\text{Li}$  on a logarithmic scale as a function of the percentage of RMEs retained after truncation.  $N_{\text{max}} = 20$ ,  $\hbar\omega = 20$ .

An error on the order of keV is acceptable for calculating the energy of these nuclei as that is also the accuracy of the interaction that was used. We see in Figure 3 that for  ${}^3\text{He}$  the energy has converged to within 1keV of the exact value with only 40% of the RMEs retained for  $N_{\text{rel,max}}$  truncation and 25% of the RMEs are retained for  ${}^6\text{Li}$ .  $N_{0,\text{max}}$  truncation requires 95% of the RMEs to converge to the accuracy for  ${}^3\text{He}$  and 90% for  ${}^6\text{Li}$ . Finally  $(\lambda_0, \mu_0)_{\text{max}}$  truncation requires 75% of the RMEs to converge to an error on the order of keV for  ${}^3\text{He}$  and 65% for  ${}^6\text{Li}$ .

In Figure 3 we are plotting the fractional energy on a logarithmic scale to see if we can identify the convergence pattern. A linear falloff would indicate an exponential convergence.  $N_{\text{rel,max}}$  and  $(\lambda_0, \mu_0)_{\text{max}}$  truncations could have a locally exponential convergence to the exact value of energy for  ${}^6\text{Li}$  as the percentage of RMEs retained is increased. However, we do not observe this same dependence for  ${}^3\text{He}$ . Fractional error of the calculated energy does not monotonically increase as the percentage of RMEs retained is increased for lower values of  $N_{\text{rel,max}}$ ,  $N_{0,\text{max}}$  and  $(\lambda_0, \mu_0)_{\text{max}}$ . This is seen by the point of increased fractional error as the percentage of RMEs retained is increased for each curve in  ${}^3\text{He}$ . This may be due to some new physics in the interaction for states with lower numbers of oscillator quanta.

$N_{\text{rel,max}}$  truncation and  $(\lambda_0, \mu_0)_{\text{max}}$  truncation perform better than  $N_{0,\text{max}}$  which is evident from the lower percentage of RMEs required to still obtain the desired accuracy for energy.  $N_{\text{rel,max}}$

truncation is a truncation on the relative interaction so it is not viable in a two-body single particle basis.  $(\lambda_0, \mu_0)_{\max}$  truncation is not dependent on the relative interaction and can be used as a truncation on the two-body single particle basis and could be effective in the NCCI framework.

## 5 Conclusion

In this report we were inspired by the approximate  $U(3)$  symmetry of the nuclear system to study  $SU(3)$  and oscillator based truncations of nuclear interactions. The JISP16 nuclear interaction was used as a first test case. This was done by setting specific RMEs to zero and solving the many-body problem using the NCCI framework.

We used three types of truncation schemes.  $N_{\text{rel,max}}$  truncation, is a truncation on the number of oscillator quanta carried by the relative basis state of both the bra and ket.  $(\lambda_0, \mu_0)$  truncation, is restricting the allowed  $SU(3)$  tensor components of the interaction. In  $N_{0,\max}$  truncation, the oscillator constant of the operator was restricted. We found that for  $N_{\text{rel,max}}$  truncation we can use  $N_{\text{rel,max}} = 14$  to calculate the energy within an error on the order of 1keV while only retaining 40% of the RMEs. Similar results are seen for  $(\lambda_0, \mu_0)_{\max}$  truncation.  $N_{0,\max}$  truncation loses accuracy for energy calculations quicker than the other two truncations.

The next step towards using these truncation schemes is to examine how stable the conclusions we have found are for different choices of interaction and for nuclei with  $A > 6$ . To do this we solve the truncated Hamiltonian eigenvalue problem using different interactions, and study the truncation effects of these realistic nuclear interactions to find similarities and differences between them and JISP16.

We want to use these truncations to reduce the computational load of the method. Now that we have established that these truncations are viable, we need to return to SpNCCI and determine how much they actually help reduce computational resources needed.

## 6 Acknowledgements

Patrick J. Fasano is thanked for assistance in this research. This material is based upon work supported by the U.S. National Science Foundation under Award Number NSF-PHY05-52843 and by the U.S. Department of Energy, Office of Science, Office of Nuclear Physics, under Award Number DE-FG02-95ER-40934. TRIUMF receives federal funding via a contribution agreement with the National Research Council of Canada.

## References

- <sup>1</sup>B. R. Barrett, P. Navratil, and J. P. Vary, *Part. and Nucl. Phys.* **69**, 131 (2013).
- <sup>2</sup>P. Maris, J. P. Vary, and A. M. Shirokov, *Phys. Rev. C* **79**, 014308 (2009).
- <sup>3</sup>P. Navratil, J. P. Vary, and B. R. Barrett, *Phys. Rev. Lett.* **84**, 5728 (2000).
- <sup>4</sup>P. Navratil, J. P. Vary, and B. R. Barrett, *Phys. Rev. C.* **62**, 054311 (2000).
- <sup>5</sup>P. Navratil, V. G. Gueorguiev, J. P. Vary, W. E. Ormand, and A. Nogga, *Phys. Rev. Lett.* **99**, 042501 (2007).
- <sup>6</sup>A. E. McCoy, M. Caprio, and T. Dytrych, *Ann. Acad. Rom. Sci. Ser. Chem. Phys. Sci.* **3**, 17 (2018).
- <sup>7</sup>A. M. Shirokov, J. P. Vary, A. I. Mazur, and T. A. Weber, *Phys. Lett. B* **644**, 33 (2007).
- <sup>8</sup>J. P. Vary, P. Maris, E. Ng, C. Yang, and M. Sosonkina, *J. Phys. Conf. Ser.* **180**, 012083 (2009).
- <sup>9</sup>P. Maris, M. Sosonkina, J. P. Vary, E. Ng, and C. Yang, *Procedia Comput. Sci.* **1**, 97 (2010).
- <sup>10</sup>M. Moshinsky and T. A. Brody, *Rev. Mex. Fis.* **9**, 181 (1960).
- <sup>11</sup>M. Moshinsky and Y. F. Smirnov, *The harmonic oscillator in modern physics* (Harwood Academic Publishers, Amsterdam, 1996).

Advances in Time Projection Chamber Design for Nuclear Reaction and  
Nuclear Structure Detection

Aidan D. Tollefson

2018 NSF/REU Program

Physics Department, University of Notre Dame

Advisor:

Dr. Tan Ahn

---

**Abstract.** The time projection chamber, or TPC, project at Notre Dame allows precision measurement and tracking of nuclear reactions in order to explore nuclear structuring. Advantages to the TPC are its sensitivity to nuclear-scaled reactions and its ability to reconstruct the collision kinematics within the reaction, increased experimental results while using less beam relative to other detection systems, larger active target path which equates to increased reaction probability, and higher detection resolution which results in pinpoint reaction location and corresponding beam energy. Measures have been taken to both increase TPC run efficiency and establish compatibility with Notre Dames nuclear science laboratory through unique component design and assembly. New electric field modeling of the TPC aids in the design process and troubleshooting of the chamber physics by ensuring sufficient field uniformity within the chamber. Calculations with SRIM, a program that calculates the stopping range of ions in matter, will be tested against future acquired run data.

---

## Background and Motivation

Humankind dating back to the ancients has believed that structure underlies reality. Lifetimes of work have been dedicated to uncovering patterns and structure in order to conceptualize the universe and its natural phenomena. Bringing order and simplicity to the seemingly complex gives humankind access to power and meaning, as we increasingly understand how nature can be harnessed for our story and how our story fits into the history of the universe.

Understanding the structural evolution of radioactive nuclei is one of the keys to unlocking the mysteries surrounding how the universe developed. There is a high propensity for objects to congregate and structure on all physical scales large and small. The belief that the same phenomena that underlies galactic structuring and quark structuring guided the physical

intuition behind searching for nuclear structuring at the nuclear scale. Early work in nuclear structure detection rose from analysis of nuclear decay processes; alpha decay hinted at the possible existence of alpha clusters prior to emission. This structure of quantum many-bodied systems is greatly affected by changes in nucleon numbers and nucleon energy [4]. Alpha clusters have been shown to increase in number as mass number and internal energy increases. One of the best ways to explore these phenomena is to analyze the reaction dynamics of unstable nuclei that lie outside the line of stability [1]. Researching alpha clustering is crucial in further understanding the stellar synthesis of elements.

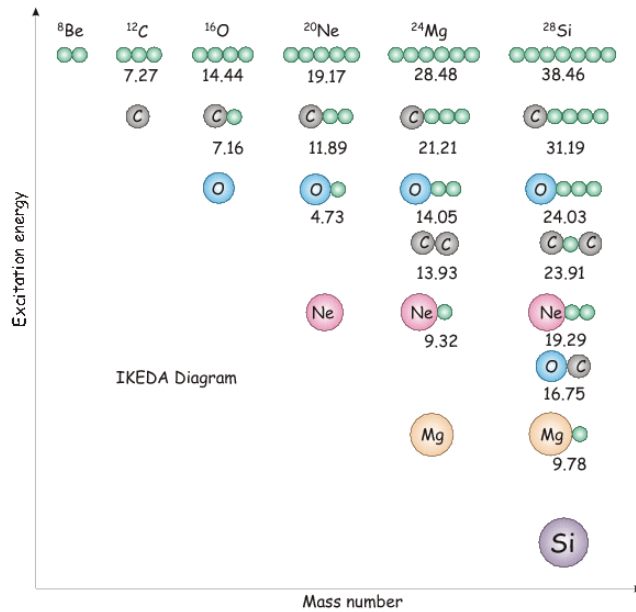


Figure 1: Excitation energy vs. mass number shows how alpha clusters develop as energy is added to the nucleus [4].

## Objective

One way nuclear clustering can be tested is through data analysis of nuclear cross sections. Dr. Ahn's group detects nuclear cross sections with a time projection chamber (TPC). TPC detectors have unique advantages that make them important tools in nuclear structure detection. Advantages to the TPC are its sensitivity to nuclear-scaled reactions and its ability to reconstruct the collision kinematics within the reaction, increased experimental results while using less beam relative to other detection systems, larger active target path which equates to increased reaction probability, and higher detection resolution which results in pinpoint reaction location and corresponding beam energy.

An incident heavy isotope beam strikes a lighter gas target within the chamber. As the heavy ion beam propagates through the target, it loses energy. A nuclear reaction occurs somewhere in the target region and the daughter products ionize the gas. An electric field forces the electrons from the ionization towards a signal-amplifying detector. The signal-amplifying detector, called the Micromegas [1], will give a one-dimensional coordinate of each charged daughter product. Because the nuclear reactions are energy dependent, calculating the energy loss as a function of distance is crucial in finding the specific energy regions for reaction initiations.

The beam particles react with the active target particles to produce outgoing charged particles. The charged particles ionize gas atoms as they propagate through the active target region of the chamber. The resulting ionization electrons drift down at a constant rate due to the electric field within the chamber and their signals are picked up and amplified by the Micromegas. The paths of the daughter products are reconstructed from the time-carrying information provided by these ionization electrons. For measuring nuclear reaction products, particle identification involves analyzing their energy deposition profiles which act as particle fingerprints. With the high spatial and energy resolutions of the TPC, comparing energy deposit profiles to calculations will aid the identification process [1].

## Method

Notre Dames TPC design draws on some of the design components of an Active Target Time Projection Chamber (AT-TPC) at the National Superconducting Cyclotron Laboratory (NSCL) Michigan State University [1]. The TPC remains in design, assembly, and installation phases, as there are important aspects to consider when focusing on experimental nuclear structuring. Practical improvements can be made to the TPC through the design of a vacuum-sealing beam window and electric potential simulations in the chamber. Geometric construction and dimensioning of TPC components is done through Autodesk Inventor. Investigation and visualization of electric potential and electric field line within the chamber volume requires simulations provided by COMSOL.

### Beam Window

Since the TPC remains in design and assembly stages, there were several features that remained to be improved and refined. There needed to be a way to allow a particle beam to enter the chamber while maintaining a near-vacuum seal. A beam window aluminum piece was proposed as a solution. Using Autodesk Inventor I created the geometries of several beam window prototypes (Fig. 2). It was necessary for the piece to be International Standards Organization (ISO) compatible, allow beam passage through an opening, and not interfere with the electric field gradient within the chamber.

The manufacturer of the vacuum chamber, the Kurt J. Lesker company, allows access to the CAD files of their products, and I based many dimensions of my parts off of those files. There is a 40mm gap between the chamber wall and the field cage. I created several beam window prototypes each with different distances from the field cage and different edge geometries. The window prototypes allowed various gaps before the field cage with edge geometry options of right angled edges, chamfered edges, and filleted edges (Fig. 2).

After some deliberation, it was decided that the prototype that comes flush with the plane of the chamber wall and has right angled edges is the simplest and most unobtrusive

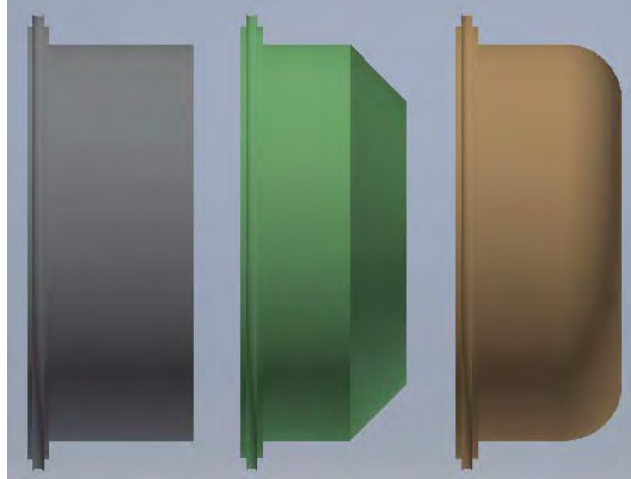


Figure 2: Side profiles of the beam window prototypes. From left to right, right edge, chamfered edge, and filleted edge.

design. Conveniently, it was also the quickest and most inexpensive design as well. As shown in Fig. 3.



Figure 3: Side profiles of a Kurt J. Lesker ISO ring model on the left and the new right edge prototype.

In the future as improvements are made to the TPC system, some of the other prototypes may be fabricated. There is a 40mm gap between the chamber wall and the exterior of the field cage. Bringing the beam window to within only 20mm of the field cage makes the beam path 20mm shorter and will save energy. The geometry of the edges may be changed as

well. Electric fields are strong at small geometric angles and sharp edges. Any mitigation of sharp edges will reduce the likelihood of electric sparking between the field cage and the beam window within the chamber.

## COMSOL

It is crucial to analyze the electric potential and electric field lines within the chamber. Uniform electric field lines from a consistent electric potential gradient are necessary for uniform electron drift velocity. COMSOL is a finite element analysis software that has multi-physics solving capabilities and has an electrostatics module that directly applies to the physics pervading the TPC. Modeling the TPC in COMSOL is a simple, practical, and powerful way to analyze its electrostatic properties.

First, using COMSOL's CAD import feature, I placed the field cage geometry inside the model and built the geometry of the chamber around the field cage. I then assigned material properties to the domains of the geometry; conductors were made of aluminum, a low pressure helium gas mixture pervaded the rest of the volume. The field cage operates as a voltage divider with a constant voltage stepdown between conducting rings. Within the electrostatics module, electric potentials were assigned to several regions of the model with  $-10,000$  Volts at the cathode,  $-200$  Volts at the base plate, and constant stepdown voltages assigned to the rings. All chamber walls were grounded. Finite element analysis methods require breaking up model information into nodes via meshing. Meshes can be customized to best suit the geometry, data storage allowance, and desired computation time of a simulation. Initial problems occurred because the CAD model had details too fine to mesh, so I had to replace the field cage geometry with a simpler geometry involving only the conductors. Once all of the physical properties were assigned in the model, a study could be run to solve for the electric potential within the chamber. Plots of electric potential and electric field lines can be generated from the results of the study.

## SRIM

SRIM (Stopping Range of Ions in Matter) is a group of programs that makes the stopping range of ions in a medium calculable [2]. Any type of ion beam with a specific energy level can be selected to collide with a target and five properties are then calculated. These properties are ion energy, nuclear energy rate of change, electric energy rate of change, projected range, longitudinal straggling, and lateral straggling. Nuclear rate of change effect is greater at low beam energy, and the electric rate of change effect is greater at high beam energy. Future work is planned to use SRIM to calculate energy savings of various beam window prototype depths.

## Results and Implications

Running studies with the electric potential and the correct TPC geometry proved to be useful in the evaluation of TPC construction readiness. In order to maximize the quality of TPC experimentation, special focus should be placed on assessing electric field lines within the chamber volume and its effect on the beam line energy and beam window geometry. COMSOL has shown that the electric field lines remain uniform within the chamber over the detection region (Fig. 4). Future simulations can be run from the COMSOL model that I created and be adjusted appropriately to account for electrical, geometric, and property changes.

The TPC is now several steps closer to being run-ready. The chamber, by way of the new beam window, now allows particles to pass through a thin and unobstructed foil while keeping a pressure seal around the active target chamber. Modeling the chamber electrostatics in COMSOL makes it possible to examine the invisible electric potential gradient and corresponding electric field lines. The unobtrusive design of the beam window means there is a low chance of sparking between the window and the field cage. This design also keeps the electric field lines uniform within the target region of the chamber, which preserves a constant drift velocity. The COMSOL modeling will also prove helpful for future design

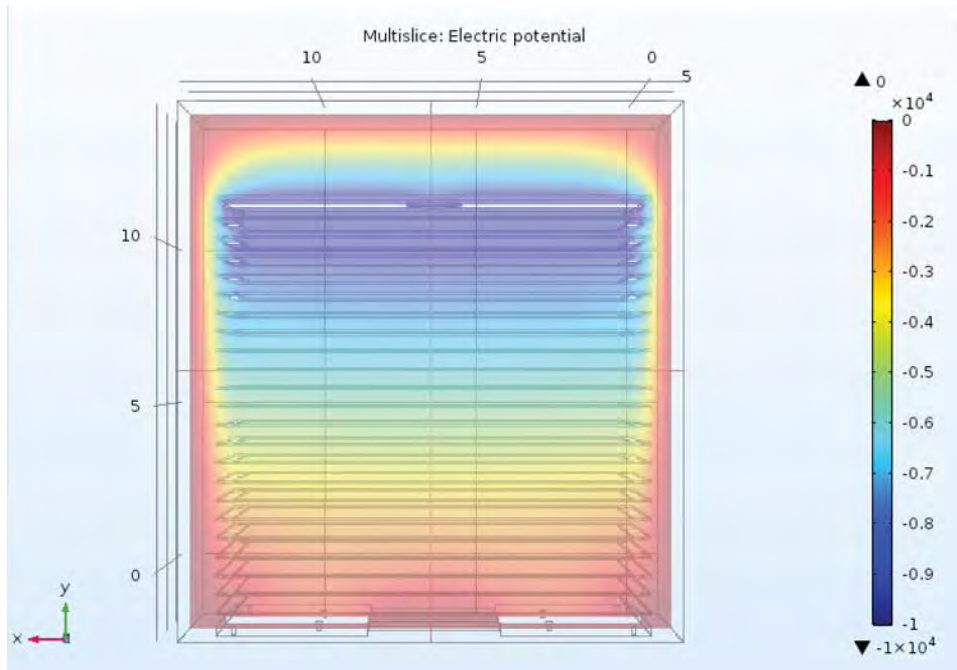


Figure 4: COMSOL plot of electric potential within the chamber.

changes of the chamber as revisions are made to it. SRIM programs will be able to calculate the energy saved by any future beam window prototypes depending on how closely the window approaches the field cage.

After my work this summer, the TPC is much closer to being completely finished and ready for implementation and my simulations will continue to be useful tools for other TPC project members. The beam window should be manufactured within a week after my departure and future students working on the TPC will be able to reference my notes on COMSOL modeling and SRIM to better study other components of the project. There is much to be excited about regarding the progress of the project, as just a few more sensory and electrical components must be installed before tests can be run, and there is hope that the TPC will be ready by the end of the year. Once ready, the TPC will be tested in the TwinSol system and the collected data will be compared to previous data and theory. Confirming the accuracy and effectiveness of the TPC is a crucial step towards implementing experimentally superior testing techniques of nuclear structures, such techniques as TPC detectors.

## References

- [1] D. Suzuki and M. Ford and D. Bazin and W. Mittig and W.G. Lynch and T. Ahn and S. Aune and E. Galyaev and A. Fritsch and J. Gilbert and F. Montes and A. Shore and J. Yurkon and J.J. Kolata and J. Browne and A. Howard and A.L. Roberts and X.D. Tang, “Prototype AT-TPC: Toward a new generation active target time projection chamber for radioactive beam experiments”, Nuclear Instruments and Methods in Physics Research Section A: Accelerators, Spectrometers, Detectors and Associated Equipment, Vol. 691, p. 39 - 54, 2012
- [2] D. Suzuki, A. Shore, W. Mittig, J. J. Kolata, D. Bazin, M. Ford, T. Ahn, F. D. Becchetti, S. Beceiro Novo, D. Ben Ali, B. Bucher, J. Browne, X. Fang, M. Febraro, A. Fritsch, E. Galyaev, A. M. Howard, N. Keeley, W. G. Lynch, M. Ojaruega, A. L. Roberts, and X. D. Tang, “Resonant scattering of  $^6\text{He}$ : Limits of clustering in  $^{10}\text{Be}$ ”, Physical Review, C 87, 054301, 2 May 2013
- [3] Fritsch, Adam and Beceiro-Novo, Saul and Suzuki, D and Mittig, Wolfgang and Kolata, J and Ahn, T and Bazin, D and Becchetti Jr, Frederick and Bucher, Brian and Chajacki, Zbigniew and Fang, Xiao and Febraro, Michael and M. Howard, A and Kanada-En'yo, Y and Lynch, William and Mitchell, Alan and Ojaruega, M and M. Rogers, A and Shore, A and Wang, Hongwei, ”One-dimensionality in atomic nuclei: A candidate for linear-chain clustering in  $^{14}\text{C}$ ”, Physical Review C, Vol. 93, 2016
- [4] Prof. Martin Freer, Univeristy of Birmingham, Edgbaston, Birmingham, “Clusters in nuclei”, [www.scholarpedia.org/article/Clusters-in-nuclei](http://www.scholarpedia.org/article/Clusters-in-nuclei), 2010

---

# RECONSTRUCTION OF HIPPO SUPERSONIC GAS JET TARGET

---

XIANFENG WANG

2018 NSF/REU Program

Department of Physics, University of Notre Dame

ADVISOR: PROF. MANOËL COUDER

## Abstract

HIPPO, a supersonic windowless helium gas jet target, is designed and reconstructed as the target for the beam from 5 MeV  $^5\text{U}$  electrostatic accelerator located at Nuclear Science Laboratory (NSL) of the University of Notre Dame. Connected to the target area, St. George recoil separator has been developed to perform, in inverse kinematic, radiative capture experiments of interest to nucleosynthesis. Inverse kinematics, here, means that a heavy ion beam is bombarding a lighter nuclear target. The nozzle-catcher system and chamber have been designed and prepared. A differential pumping system is set up to lower the pressure in the target chamber down to  $10^{-7}$  torr in the beamline. The advantages of the windowless design and advantages that gas target compared with the solid target will be discussed. An Arduino based system is set up and now we are able to control the pumps with a touch screen. We have performed preliminarily pressure measurements. Initial experiments are discussed along with plans for future use at the NSL.

## 1 Introduction

Human was born with the fascination with the starry sky, in spite of diverse cultures. However, we did not make a profound understanding of the forming of our universe until nuclear physics made significant progress in last century. The study of nuclear astrophysics concerns the nuclear reaction in stellar environment. After the hydrogen burning process inside a evolved star, helium is accumulated in the stellar core. Then,  $^{12}\text{C}$ , which is formed during triple- $\alpha$  process, can radiatively capture a helium nucleus to form  $^{16}\text{O}$  and release  $\gamma$ -ray. Other heavier elements can be formed by this  $\alpha$  capture reaction, which is crucial to

understand the energy production and nucleosynthesis during stellar helium burning. Several experimental methods have been applied to measure the cross-section of these reactions.

In low energy direct kinematics experiments, the measurement of the gamma rays of interest is often handicapped by cosmic ray induced background gamma radiation, or by gamma radiation from natural long-lived materials in the experimental environment , or frequently also from beam induced gamma radiation on target impurities[1]. Therefore, to limit the contribution of cosmic ray induced background, some experiments are performed underground. Different from the direct kinematics, the method of inverse kinematic indicates that an accelerated heavy ion beam is impinged on a lighter nuclear target. Thus, our reaction of interest can be clearly distinguished from unwanted background radiation[2]. St. George, the recoil separator developed at Nuclear Science Laboratory in University of Notre Dame, is performing inverse kinematic experiment to study  $(\alpha, \gamma)$  reactions[3]. The recoil nuclei emitted from the target area can be electromagnetically separated from the unreacted beam nucleus.

## 2 Design of the HIPPO gas target system

### 2.1 General description

The supersonic jet in HIPPO(HIGH Pressure POint-like gas system) provide a confined (relative to the size of the ion beam) region of gaseous helium where the density is as high and uniform as possible, compared with the extended gas target[4]. This property serves perfectly as a gas target for St. George recoil separator, because all the reaction productions can be originated from a localized(point-like) area, which guarantees the optimum mass

separation[1]. A heavy radiative ion beam gains energy from 5U electrostatic accelerator. In the target area, high density gas is continuously injected through a simple converging-diverging nozzle into the central chamber, where the reaction between the radiative beam and the gas target takes place. Then the gas flows into a catcher, connected with the roots blower WS501 and the gas circulation system.

In the target area, high pumping speeds is achieved using large roots blowers and turbo pumps[6].

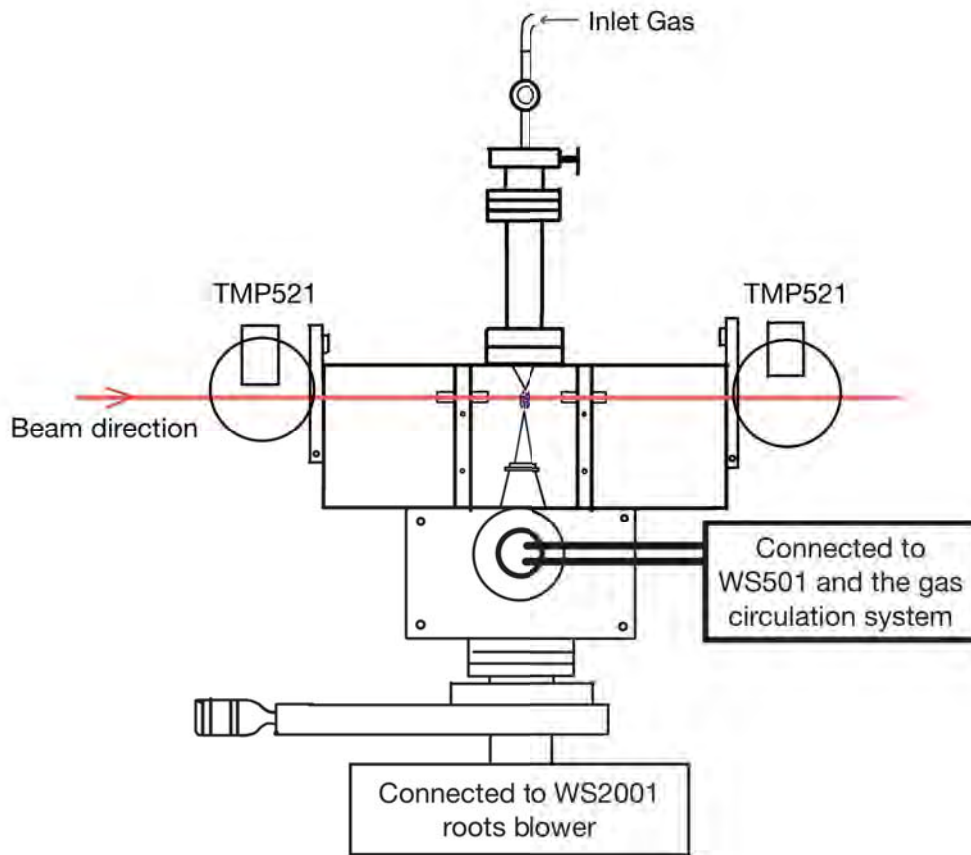


Figure 1: Diagram of the gas target system. WS stands for Roots Blowers(Leybold). TMP stands for turbo-molecular pump(Preiffer), two of which placed in the front of the chamber, two in the back and one connected to the chamber.

## 2.2 The windowless design

There used to be an experimental arrangement that there are some “windows” in the foil cell, allowing the beam to enter and exit, as well as allowing the reaction products get into the detectors. However, this design brings some frustrating issues. First, the beam may scatter with the foil cell, which causes a significant energy loss. Moreover, the reaction between the beam and the foil will cause the heating and possible breaking of the cell, thus limiting the gas pressure and effective beam intensities. To avoid this energy loss of the beam through the target, we adopt the windowless design in HIPPO, in which the windows are replaced by several apertures through which the beam passes. A series of pumps, which are known as differential pumping system, are set up between the apertures to lower the gas pressure from about 1 torr to  $10^{-7}$  torr in the target chamber.

## 2.3 Gas target compared with solid target

The targets can be divided by the materials into solid targets and gas targets. Solid target can either be made for the transmission of the beam or to stop the beam. However, transmission targets cannot be cooled efficiently, so they can be easily destroyed[6]. On the other hand, the beamstop backings may produce a intolerable beam-induced radiation. It may also produces a large number of Coulomb-scattered ions and, therefore, are not suitable for measurements of elastic scattering cross sections.

Windowless gas targets, which ensure a high chemical purity along with the variable target density, can efficiently eliminated these problems. Therefore, in certain circumstances, gas targets are more desirable than solid targets.

### 3 Experimental set up

As can be seen in Figure 1, high density gas is continuously injected from the converging-diverging nozzle into the catcher, and a pure point-like gas area is thus formed at the center of the chamber. The WS2001 pump under the catcher pumps the gas away into a gas circulation system, which is still under development. According to the data from previous experiment[1], the optimum catcher diameter for the setup was 10.5 mm. The smaller catcher is too small to fit all the jet, whereas the larger one allows at higher pressures for some back-flow into the central chamber, and thus elevating the pressure.

The silicon detector, which can detect the elastically scattered particles in Rutherford scattering experiments, can be set up in the chamber with a certain angle from the beam direction. It can provide the information of the thickness of the target and can also be used to normalize the beam intensity.

Three pairs of apertures(only one pair showed in Figure 1)has been placed separately before and after HIPPO along the beam direction. These apertures are able to change the pumping impedance allowing for differential pumping. They can also serve for collimation to make sure that the diameter of beam is smaller than the scale of gas target. A monitoring quartz system, which extends a camera into the beam line, is also prepared to visualize the beam on a monitor, thus allowing us to monitor and correct the beam direction. Two Faraday cups are separately placed in the front and back of HIPPO, which is used to measure the transmission of the beam through HIPPO.

We developed an Arduino based operating system, which allow us to control the switch of the pumps by touchscreen.

Since most of the gas is unreacted and flow straight into the catcher, therefore, to make full use of it we preliminarily designed a gas circulation system to guide the gas flow back to the chamber area, which indicates a series of pumps inside the dashed line in Figure 2 and is still underdeveloped.

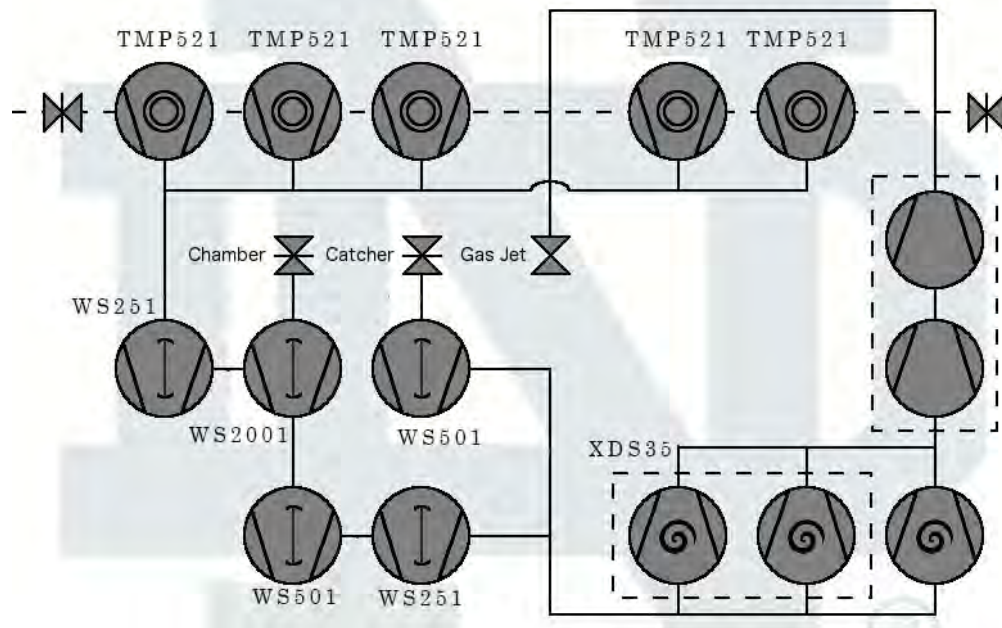


Figure 2: Scheme of the whole circulation system.

## 4 Pressure measurements

Six Hornet convection pressure gauges have been placed in different parts of the central chamber. We have performed a preliminary pressure test of the performance of the vacuum pumps and it is proved to be successful. In next steps we plan to measure the pressure distribution across the chamber area at certain inlet helium pressure and investigate the differential pumping conditions as a function of inlet pressure.

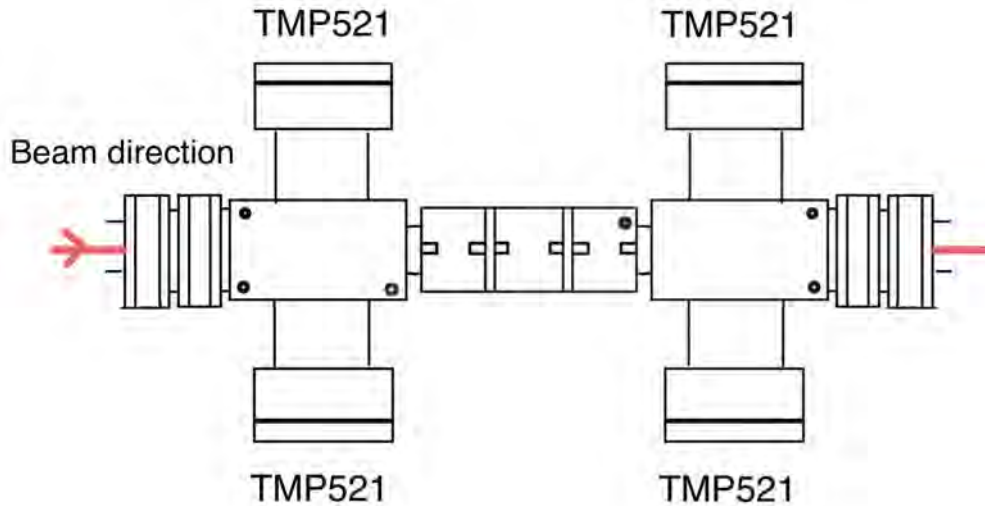


Figure 3: Upper view of the chamber. Six dots indicate the Hornet convection pressure gauges which used to test the pressure profile of the chamber area.

## 5 Conclusion

In summary, HIPPO supersonic windowless gas jet targets have several advantages compared with the solid target and gas target with “windows”, includes lower contaminant reactions, localized target, variable target density, pure helium gas target and allowing for higher beam densities. We have set up the differential pumping system and performed a preliminarily pressure test successfully. The follow-up experiments will be carried out to sufficiently test the property of the new gas target, and finally use it as an effectively gas target for St. George recoil separator to study low energy ( $\alpha, \gamma$ ) reactions in inverse kinematics.

## Acknowledgement

I would like to give my sincere gratitude to Prof. Manoël Couder, my advisor who gave me great guidance and advice on this project with extraordinary patience and enthusiasm throughout the summer. Special thanks also go to Dr. Ed Stech, Dr. Daniel Robertson, graduate student Shane Moylan, Christopher Seymour, Luis Morales and Gwenaëlle Gilardy. Finally, thanks to the University of Notre Dame and Prof. Umesh Garg for hosting me this summer and providing me with the opportunity to participate in this research project.

## References

- [1] A. Kontos, et al.: *HIPPO: A supersonic helium jet gas target for nuclear astrophysics*, Nuclear Instruments and Methods in Physics Research Section A(2012)
- [2] D.W.Bardayan, et al.: *The JENSA Gas-Jet Target for Radioactive Beam Experiments at ReA3 and FRIB*, Physics Procedia(2015)
- [3] M. Couder, et al.: *Design of the recoil mass separator St. George*, Nuclear Instruments and Methods in Physics Research A 587, 1 (2008)
- [4] Zach Meisel, et al.: *Exploratory investigation of the HIPPO gas-jet target fluid dynamic properties*, Nuclear Instruments and Methods in Physics Research A 828, 8 (2016)
- [5] Claus E. Rolfs, William S. Rodney: *Cauldrons in the Cosmos*, The University of Chicago Press(1985)
- [6] C. Illiadis: *Nuclear Physics of Stars*, John Wiley & Sons(2015)



# **GALACTIC ARCHEOLOGY**

*Investigating r-process Absorption Signatures in Stellar Spectra in Search of r-II Stars*

TINO WELLS

2018 NSF / REU Program  
Physics Department, University of Notre Dame

ADVISOR: Prof. T. Beers

## ABSTRACT

Nucleosynthetic origins of various elements past iron remain a partial mystery. Through neutron-capture reactions, atoms change from one element to the next, through two scenarios: slow (s-) and rapid (r-) neutron-capture. Specifically, s-neutron-capture, or s-process, occurs when a nucleus undergoes  $\beta$ -decay before acquiring an additional neutron; where r-neutron-capture, or r-process, occurs when an additional neutron is captured prior to the ensuing  $\beta$ -decay. S-process elements have been linked to a certain stage in a stars life cycle, known as the Asymptotic Giant Branch (AGB stars); the astrophysical cite of r-process elements are currently unknown. By observing signatures of known r-process elements in stellar spectra—of stars located in ultra-faint dwarf galaxies and within our Galactic halo—this research focuses on identifying possible candidates of an extremely rare stellar subclass: r-II stars (defined in the introduction). In total, we identify three possible first-pass constraints that isolate a significant percentage of tested r-II stars: (1) Using the absorption-line strengths of singly-ionized eurpoium (Eu-II; 4129 Å), singly-ionized dysprosium (Dy-II at 4103 Å), and neutral iron (Fe-I at 4099 Å), we compute the ratios of each specie with respect to iron, and define the constraints of  $1.0 \leq \text{EW}(\text{Eu-II}) / \text{EW}(\text{Fe-I}) \leq 1.6$  and  $0.36 \leq \text{EW}(\text{Dy-II}) / \text{EW}(\text{Fe-I}) \leq 0.6$ , yielding six r-II stars in a sample of seven; (2) Using  $\text{EW}(\text{Dy-II})$  as a function of metallicity, we identify a region that encompasses six out of seven r-II stars; (3) Utilizing a flavor of (2), we construct  $\text{EW}(\text{Dy-II})$  as a function of effective temperature ( $T_{\text{EFF}}$ ), and define an additional region isolating all seven tested r-II stars. We suspect the collective implementation of these constraints will filtrate a

given sample and quickly identifying stars with similar characteristics and ultimately increase the discovery rate of this rare subclass.

## INTRODUCTION

Astrophysical production of heavy elements via r-process—28% of all elements, and roughly 50% of those heavier than iron—in the early universe remains an open question. In order to investigate the nucleosynthesis of the r-process elements, we observe a specific category of stars formally known as metal-poor. As defined in [1], the chemical abundances of observed stars (\*) are compared to the Sun ( $\odot$ ), and given the following notation:  $[A / B] \equiv \log_{10}(N_A / N_B)_* - \log_{10}(N_A / N_B)_{\odot}$ , where  $N_A$  and  $N_B$  are the number of element A and element B atoms, respectively. Additionally, [1] defines a rare subclass of metal-poor stars, known as r-II or highly r-process-enhanced stars, that must meet two constraints regarding their chemical abundances:  $[\text{Eu} / \text{Fe}] > +1.0$  and  $[\text{Ba} / \text{Eu}] < 0$  (I refer the reader to *Table 1* and *2* for additional definitions of stellar classifications). However, the full analysis of these stars, detection methods, and rate of discovery have various limitations, such as the time necessary in estimating the required parameters for stellar classification, and needing a relatively large telescope with a high-resolution spectrograph to observe them. In response to these issues, the research below has been devoted to accessing different methods/ways that isolate r-II stars. Within this discipline, there have been previous attempts to do so using the absorption-line signature of singly-ionized europium, a known product of r-process-enrichment, however, the results find it difficult to separate r-II stars from a similar subclass, known as r-I or moderately r-process-enhanced stars. This research

carries out those efforts with singly-ionized dysprosium, another known product of r-process-enhancement.

In the sections below, we address the entirety of parameters used in the effort of isolating r-II stars in Methods, highlight the constraints and success rates thereof in Results, and follow by discussing possible ways to improve the isolation percentage.

## METHODS

Defining constraints to classify possible r-II candidates falls into three flavors; first, we quantify the absorption-line strength of r-process elements by measuring two ionic species equivalent-widths (EW; singly-ionized europium and dysprosium) and create a ratio relative to the equivalent-width of neutral iron (see *figure 1*). Accurately measuring the EW of singly-ionized dysprosium—EW(Dy-II)—is critical due to being used in the all defined constraints. Furthermore, we use EW(Dy-II) as a function of [Fe / H] metallicity and define a region highly populated by r-II stars (see *figure 2a*). In *figure 2b*, notice the same EW(Dy-II) is used, however, as a function of effective temperature ( $T_{\text{EFF}}$ ) of the observed star. The python software that performs this filtration process takes a list of stars with required parameters, applies the constraints on the given sample and allows for the user to visually inspect which stars pass which constraints.

## RESULTS

After measuring the absorption-line strengths of the three species, the primary constraint constructed to isolate r-II stars is as follows:  $1.0 \leq \text{EW}(\text{Eu-II}) / \text{EW}(\text{Fe-I}) \leq 1.6$  and  $0.36 \leq \text{EW}(\text{Dy-II}) / \text{EW}(\text{Fe-I}) \leq 0.6$  (see *figure 1*). This region is composed for 11

stars in total, six of which are r-II stars, three are r-I stars, and two of unknown classification. Following these constraints, *figure 2a* shows the cut-off region of  $[\text{Fe} / \text{H}]$  metallicity as a function of  $\text{EW}(\text{Dy-II})$ , where stars rightward of the dashed line have been isolated for consideration. This region consists of 16 stars in total, and of these stars, we see six r-II stars, four r-I stars, and five stars of separate classifications. Lastly, *figure 2b* displays a separate cut-off region with  $\text{EW}(\text{Dy-II})$  as a function of  $T_{\text{EFF}}$ , where we now isolate all seven r-II stars, with 13 r-I stars, and four stars of additional classification, rightward of the dashed line. The collective implementation of these constraints, on a sample of 107 stars in total, produces a list of nine stars: six r-II stars, and three r-I stars, converging to a 66% success rate of all stars, and 85% success rate of r-II stars.

## CONCLUSIONS

Nucleosynthetic origins of elements past iron has been an ongoing project since the late 1950's, and has recently been estimated to be explained within the next decade. And creating a prioritized list of potential r-II candidates will surely expedite the true nature of r-process elements. By defining constraints of r-process characteristics—equivalent-widths of singly-ionized europium and dysprosium—as well as utilizing readily available information— $[\text{Fe} / \text{H}]$  metallicity and effective temperature—the filtration system identifies a prioritized list of stars highly populated by r-II classification. Additionally, not only is this process going to save an incredible amount of time, all but one tested r-II star are included in the final product. The

constraints defined from this research are currently being implemented to identify r-II candidates for future observing campaigns with the South African Large Telescope.

## **DISCUSSION**

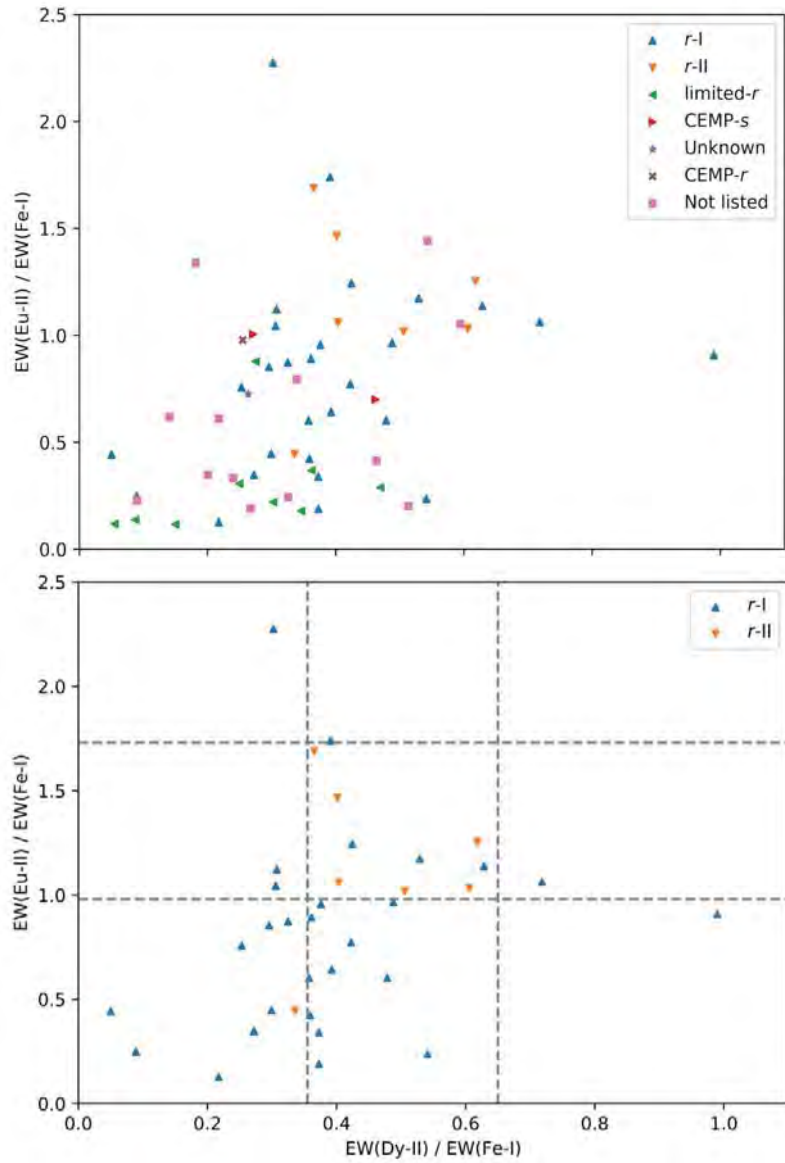
The three constraints of this research enable a relatively decent, first-pass in the isolation process, however, the entirety of the analysis process takes a much longer time. This research is focused on shining light on possible r-II candidates—essentially prioritizing stars with similar characteristics. Currently under development, we are creating a convolutional neural network (CNN) that will predict stellar parameters, specifically focused on those necessary in defining r-II stars. Although this may take some additional time, the CNN is believed to produce much more accurate and usable information, including an estimate for overall  $[Fe / H]$  metallicity, and with a growing population of known r-II stars, become more and more accurate over time.

## **Acknowledgements**

I would first like to thank NSF, the REU program, and REU coordinator, Dr. Umesh Garg, at the University of Notre Dame for funding and allowing my opportunity. I would also like to thank graduate student Erika Holmbeck for her explicit help, guidance, and expertise on this project, and a special thank you to my advisor, Professor T. Beers, for allowing REU student(s) to aid his research.

## FIGURES & TABLES

Figure 1: The EW ratios of Dy-II and Eu-II with respect to Fe-I of the sample. In the upper-panel, seven different stellar classification are shown. After removing some of the noise, and over-plotting the  $1.0 \leq EW(\text{Eu-II}) / EW(\text{Fe-I}) \leq 1.6$  and  $0.36 \leq EW(\text{Dy-II}) / EW(\text{Fe-I}) \leq 0.6$  constraints as vertical and horizontal dashed-lines respectively, we see the isolation region as the middle square of the



lower-panel. In total, this region isolates nine stars, and six out of seven total r-II stars. The single r-II star not located in this region happens to be a statistical outlier, in terms of its other stellar parameters, and therefore not heavily weighted when defining these constraints.

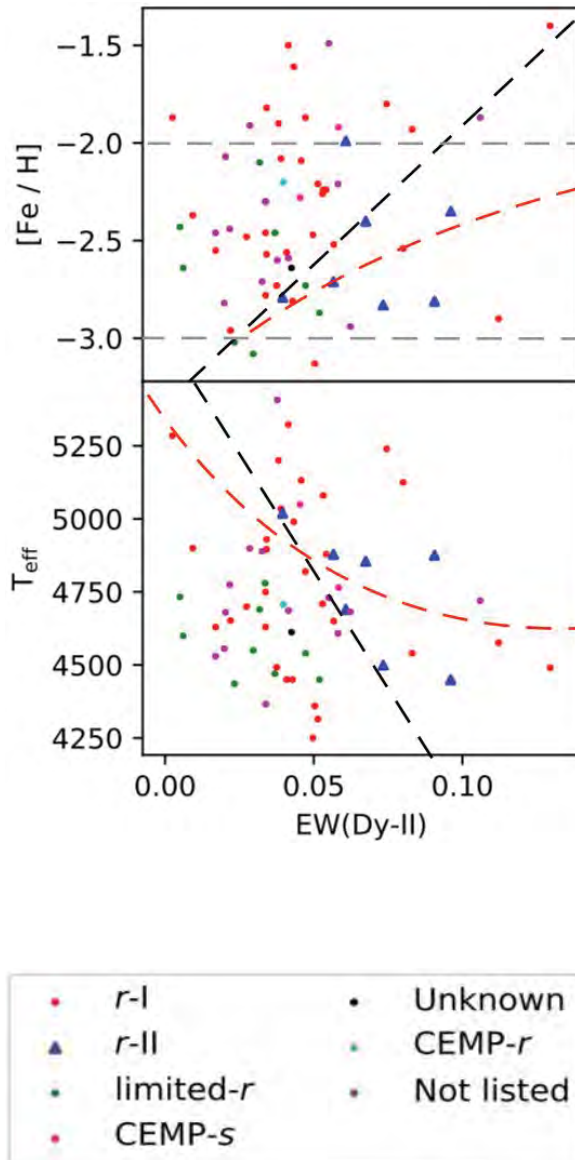


Figure 2a, upper-panel: Shown is a projection of EW(Dy-II) as a function of [Fe / H] metallicity, color-coordinated by known stellar classification. The dashed-black line representing the cut-off region, isolating stars rightward of this cut-off. The red-dashed line corresponding to a best-fit curve. The horizontal dashed-gray line represents definitions of the nomenclature in [1]; -2.0 and -3.0 referring to Very metal-poor (VMP) and Extremely metal-poor (EMP), respectively. This provides additional evidence towards stars being relatively more metal-rich having a larger EW(Dy-II) in order to still be classified as an r-II star.

Figure 2b, lower-panel: Projection of EW(Dy-II) as a function of effective temperature, with cut-off region as a dashed-black line, with an isolation region rightward of this line. Notice as temperature increases, EW(Dy-II) decreases, which agrees with common literature.

<i>Table 1: Nomenclature for stars of different metallicities, from [1]</i>		
[Fe / H]	Term	Acronym
> +0.5	Super metal-rich	SMR
~ 0.0	Solar	-
< -1.0	Metal-poor	MP
< -2.0	Very metal-poor	VMP
< -3.0	Extremely metal-poor	EMP
< -4.0	Ultra metal-poor	UMP
< -5.0	Hyper metal-poor	HMP
< -6.0	Mega metal-poor	MMP

<i>Table 2: Definitions of subclasses of metal-poor stars, from [1]</i>	
Neutron-capture-rich stars	
r-I	$0.3 \leq [\text{Eu} / \text{Fe}] \leq +1.0; [\text{Ba} / \text{Eu}] < 0$
r-II	$[\text{Eu} / \text{Fe}] > +1.0; [\text{Ba} / \text{Eu}] < 0$
s	$[\text{Ba} / \text{Fe}] > +1.0; [\text{Ba} / \text{Eu}] > +0.5$
r/s	$0.0 < [\text{Ba} / \text{Eu}] < +0.5$
Carbon-enhanced metal-poor stars	
CEMP	$[\text{C} / \text{Fe}] > +1.0$
CEMP-r	$[\text{C} / \text{Fe}] > +1.0; [\text{Eu} / \text{Fe}] > +1.0$
CEMP-s	$[\text{C} / \text{Fe}] > +1.0; [\text{Ba} / \text{Fe}] > +1.0; [\text{Ba} / \text{Eu}] > +0.5$
CEMP-r/s	$[\text{C} / \text{Fe}] > +1.0; 0.0 < [\text{Ba} / \text{Eu}] < +0.5$
CEMP-no	$[\text{C} / \text{Fe}] > +1.0; [\text{Ba} / \text{Fe}] < 0$

## References

- [1] Beers, T., & Christlieb, N. 2005, *Annu. Rev. Astron. Astrophys.* 43:531-580.



A Proposal for Experimentally Measuring the  $^{35}\text{Cl}(^3\text{He},2p)^{36}\text{Cl}$  Cross  
Section: Early Solar System Irradiation Effects on Short-Lived Radioisotope  
Production

Connor A. Williams

2018 NSF/REU Program

Physics Department, University of Notre Dame

Advisor:

Philippe Collon

## Abstract

Short-lived radioisotopes (SLRs) with half-lives  $t_{1/2} < 100$  Ma are known to have existed during the formation of the solar system around 4.5 billion years ago through the detection of their decay products in meteorites [1]. The origin of SLRs in the solar system is understood through two main production hypotheses. It is believed that a nearby supernova, Wolf-Rayet star, or thermally pulsating Asymptotic Giant Branch (AGB) star, injected newly synthesized SLRs into the Giant Molecular Cloud (GMC) from which the sun was formed [1], possibly contributing enough mass to engender the collapse of the cloud itself. However, the concentration of the decay products of  $^{36}\text{Cl}$ ,  $^{26}\text{Al}$ , and  $^{60}\text{Fe}$ , exceed their expected galactic steady-state enrichment levels, suggesting that a secondary production source may be responsible for the excess. In the sun's infancy, solar energetic particles (SEP) may have irradiated gas and dust present in the solar accretion disk, aiding the accumulation of SLRs in chondrules and Ca-Al rich inclusions (CAIs)[2]. Determining the origination of SLRs may lead to a heightened understanding of the manner in which the solar system was formed. Experimental data is needed in order to validate the solar irradiation model, and therefore, the cross sections of the nuclear reactions in question must be measured. In 2013, Bowers *et al.* proposed nine different reactions that could potentially be influential in the creation of  $^{36}\text{Cl}$ .

The cross section of the  $^{35}\text{Cl}(^3\text{He},2p)^{36}\text{Cl}$  reaction was estimated in order to evaluate the feasibility of creating the reaction in a laboratory setting. Based off of cross section predictions, seven activation energies within the range of 1.44 MeV/A to 2.51 MeV/A are proposed for future measurement.

## Introduction

Many chondrules and CAIs found in meteorites contain the decay products of SLRs that can be used to calculate abundance excesses regarding stellar injections into the GMC. The SLR  $^{36}\text{Cl}$  decays 98.1 % to  $^{36}\text{Ar}$  by  $\beta^-$  emission, and the remaining 1.9 % to  $^{36}\text{S}$  by electron capture

from the K or L atomic shells. Concentration data of both of these decay products, as well as Cl/S ratios, have been used to support the solar irradiation model. In order to verify this hypothesis, estimations on the flux of SEP from the young sun need to be matched with cross section information, to estimate total SLR production. as a result of solar irradiation. SEP have a wide energy range, which makes cross section data at various energies pertinent. We propose measurement of the  $^{35}\text{Cl}(^3\text{He},2p)^{36}\text{Cl}$  reaction, in favor of other  $^{36}\text{Cl}$  producing reactions, due to the energy limitations of the Notre Dame FN tandem accelerator.

## Nuclear Models

Experimental cross section data are essential in understanding the mechanisms that govern nuclear reactions, particularly because of the complex nature in which nucleons interact. In order to better understand these processes, different models have been constructed to explain complex phenomena such as strong absorption and nuclear scattering. Existing nuclear theory has been used to predict the cross sections of numerous reactions with great accuracy. The program TALYS was used to predict the  $^{35}\text{Cl}(^3\text{He},2p)^{36}\text{Cl}$  cross section, which uses four distinct models to account for parameters that influence reactions between projectile and target nuclei.

## Optical Model

The optical model generally discards any notion of the structure of the incident and target nuclei, and approximates them as interacting through a common potential. This potential is only a function of the distance between the centers-of-mass of the nuclei. It acts in a similar fashion to the negative nucleon-nucleon potential often used to explain strong interactions. However, the optical model potential must be complex [4] to allow for absorption from the elastic channel. In this manner, it is similar to the attenuation of electromagnetic radiation in a dielectric, via a complex index of refraction (as the name suggests).

## Compound Nucleus Model

It is typical for a low-energy projectile to merge with the target, forming a *compound nucleus*. Bohr hypothesized that on a nuclear timescale, a compound nucleus may exist for such a long time that it retains no information of how it was formed. The compound nucleus begins to distribute the bombarding energy of the projectile statistically between all nucleons present, and forms an excited state. It will subsequently find a more energetically favorable state, either by decaying electromagnetically through  $\gamma$ -ray emission, or by ejecting a nucleon (or several) with a Maxwellian energy distribution [4].

Compound nucleus formation becomes highly probable whenever a discrete excited state can be achieved, known as a resonance. Excitation functions (graphs which plot cross sections as a function of reaction energy) show distinctive resonance peaks which can be used to relate the width of the resonance to the lifetime of the excited state [3]. Wider resonances correspond to shorter lifetimes. Not only do higher excited states have wider resonances, but the spacing between states becomes much shorter, and eventually a continuum occurs where the width of the resonances exceeds the spacing between them, and discrete states can no longer be identified. This defining characteristic severely dampens compound nucleus formation for high incident energies, and causes the total cross section to be much more dependent on direct reactions (which are not considered in the TALYS code).

## Pre-Equilibrium Model

When a projectile is incident upon a target, it is possible for the two nuclei to exist in a semi-stable state in which the two have momentarily merged, but has not allotted the projectile energy among the constituent nucleons [4]. In such a state of pre-equilibrium, one or more nucleons may be emitted with a spectrum of energies near that of the projectile, as the pre-equilibrium nucleus continues to de-excite. Whereas evaporation from a compound nucleus is generally symmetric about  $90^\circ$ , decays from pre-equilibrium tend to be forward-peaked.

## Multiple Hauser-Feshbach Decay

Particularly for high energy reactions, a nucleus may remain in an excited state even after decaying, and consequent decays become necessary. Low-lying excited states cannot result in the emission of nucleons, and must therefore decay by emitting a photon or series of photons [3]. It should be noted that for increasing reaction energies, new exit channels begin to open, and the cross sections of reactions occurring at low energies may drastically decrease.

## TALYS Outputs

TALYS assumes forward kinematic reactions, in which a light projectile is incident upon a heavy target. For the purposes of our experiment, an inverse kinematic reaction is suggested, so as to ensure that the products of the exit channel will be forward peaked. A  $^{35}\text{Cl}$  beam that will be incident upon  $^3\text{He}$  in a gas chamber, with an Al catcher to collect the reaction products. Therefore, in order to assess the predicted cross section, the reaction needs to be viewed from the center-of-mass frame, in which the total momentum of the system is zero.

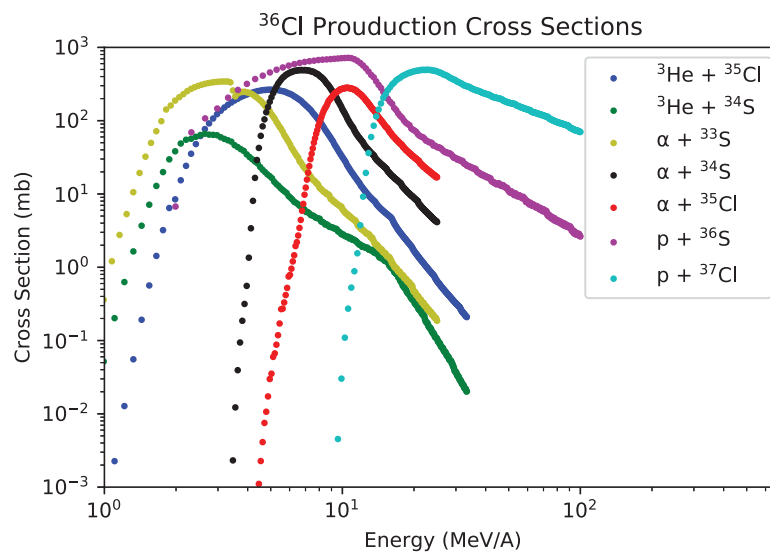


Figure 1: Seven different nuclear reaction cross sections that are important in the production of  $^{36}\text{Cl}$ .

Figure 1 displays seven nuclear reactions that may have taken place as the result of the SEP irradiation (namely protons and  $\alpha$ -particles) of the solar accretion disk. Energies are given normalized by the mass of the light nuclide to eliminate the distinction between target and projectile.

## Activations

### SNICS

In order to create a stable beam of  $^{35}\text{Cl}$  ions, a Cu cathode will be packed with AgCl powder, and placed at the back of the ion source chamber. It will subsequently be accelerated via a source of negative ions through cesium sputtering (SNICS). SNICS consists of a Cs source that is boiled to create an ionized vapor, which is accelerated toward the Cu cathode where it sputters the AgCl. The sputtered AgCl will pick up an electron, and be accelerated towards a low-energy analyzing magnet that directs the beam into the FN tandem accelerator. The isobar  $^{36}\text{Ar}$  is not expected to escape SNICS, as it is a noble gas and therefore will not become a negative ion.

### FN Tandem Accelerator

Upon reaching the FN tandem accelerator, it is assumed that the sputtered AgCl will be separated into Ag and Cl as a result of the cesium impact. The negatively charged ions will enter the low-energy side of the accelerator (0 V), and be accelerated toward the center of the accelerator (up to 10.0 MV). A carbon stripper foil at the center of the FN will create a charge distribution of positively charged Cl ions, with higher voltages corresponding to higher average charge states. The carbon foil also acts to break up any remaining molecules that may enter the beamline. Upon becoming positively charged, the ions will receive a secondary boost towards the high-energy side of the FN (0 V). As a result of the two boosts, the total energy of any ion at the end of the accelerator is

$$E_0 = V(1 + q) \quad (1)$$

where  $V$  is the terminal voltage, and  $q$  is the end charge state of the ion.

## Analyzing Magnet

An analyzing magnet will remove isotopic contamination, by passing only ions with a specific momentum-to-charge ratio. The magnet has a known radius  $r = 1.0170999$  m, thus, a magnetic field can be applied so as to select for ions with a specific mass, energy, and charge state, by the relation

$$B = \frac{mc}{qr} \left\{ 1 - \frac{1}{\left\{ \frac{E_0}{mc^2} \right\}^2} \right\}^{1/2} \quad (2)$$

where  $c$  is the speed of light,  $B$  the magnetic field strength,  $m$  the mass of the desired SLR, and  $q$  the desired charge state. While the analyzing magnet will filter out isotopic contaminants, it will not eliminate isobaric contamination, as ions of the same mass and charge state will also be accepted. The analyzing magnet will pass the ions into the  $^3\text{He}$  chamber after passing through a Ni foil that acts to separate the beamline from the chamber and fight the diffusion of the  $^3\text{He}$ . The reaction may take place anywhere within the chamber, so the energy loss experienced by both the foil and the gas must be taken into account.

## Accelerator Mass Spectrometry

After producing the  $^{35}\text{Cl}(^3\text{He},2p)^{36}\text{Cl}$  reaction in the  $^3\text{He}$  chamber, the number of  $^{36}\text{Cl}$  nuclei produced will need to be assessed in order to calculate an experimental cross section. Accelerator mass spectrometry allows for both isotopic separation (through the analyzing magnet and Wien filter) and isobaric separation (from the spectrograph and ionization chamber). A schematic for the entire beamline is given by fig. 2.

## Accelerator Mass Spectrometry at the NSL

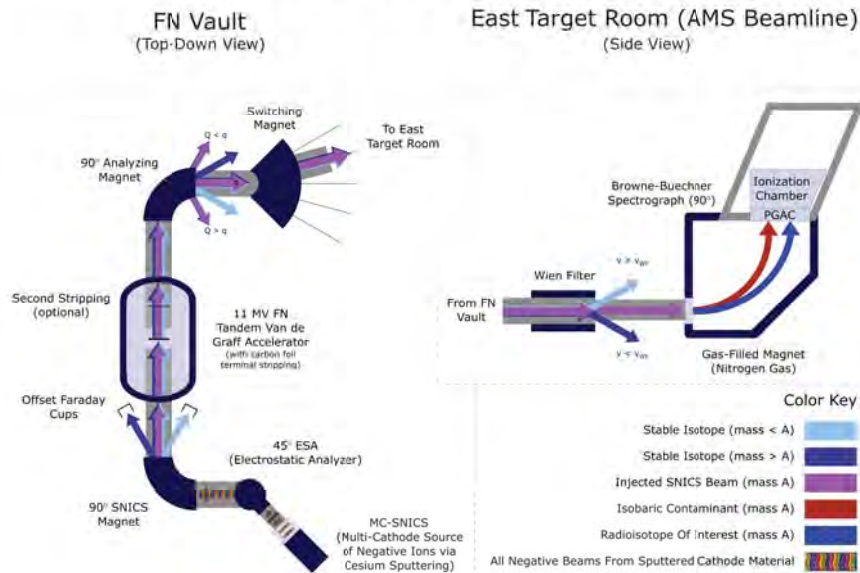


Figure 2: A schematic view of the beamline.

### Wien Filter

A Wien filter following the switching magnet will act to further filter isotopic contamination. It will apply electric and magnetic fields mutually perpendicular to the beam direction. The magnetic force is velocity dependent while the Coulomb force is not, therefore only particles of a selected velocity will pass unperturbed through the beamline; those traveling too fast or too slow will be deflected in opposite directions. The undisturbed speed is the ratio of the electric field magnitude to the magnetic field magnitude  $v = \frac{E}{B}$ .

### Spectrograph

Following the Wien filter, it is still possible for isobaric contaminants (namely  $^{36}\text{S}$ ) to travel alongside the  $^{36}\text{Cl}$  ions of interest, assuming they have the correct charge state and energy.

To filter out the  $^{36}\text{S}$  contamination, a spectrograph (gas-filled magnet) will be utilized. Nitrogen gas causes the two competing isobars to occupy a mean charge state through continuous charge exchange, leading to a separation of position between the two beams. Figure 3

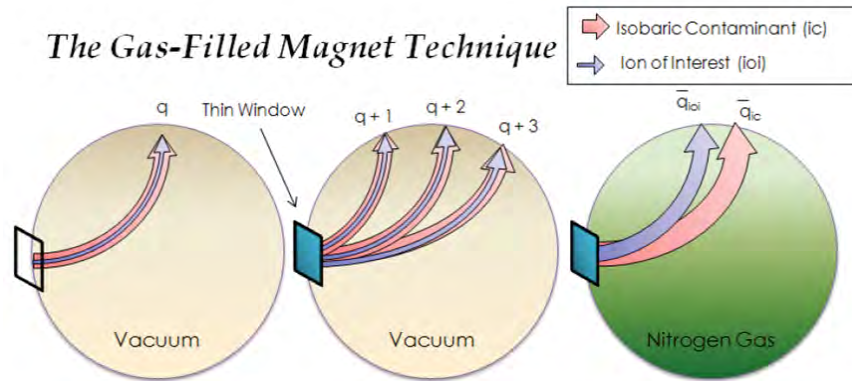


Figure 3: The gas-filled magnet causes continuous charge exchange, and the two distinct ions to coalesce around a mean charge state. This separates their position by engendering two varying magnetic forces on the isobars. In vacuum, a single stripping of electrons occur and distinctive paths containing both isobars would form.

shows that the ionization of an atom is partially dependent on its nuclear charge. These two beams will then be sent to the parallel grid avalanche counter (PGAC) for positional analysis.

## Parallel Grid Avalanche Counter

The PGAC is an assortment of wires oriented in a grid formation, that will produce position sensitive data. Electrical impulses caused by the incident ion beams will travel down both sides of the wires, and the time difference between the signals can be used to pinpoint the location of the beam.

## Ionization Chamber

After passing through the PGAC, the two beams will pass into an ionization chamber filled with the gas isobutane ( $C_4H_{10}$ ). The  $^{36}Cl$  and  $^{36}S$  nuclei will ionize the surrounding gas, and lose energy as they do so. The energy loss of both ions will partially be dependent on their nuclear charge. Therefore a Bragg curve depicting the energy loss of both ions as a function of penetration will be constructed to find the stopping ranges of both ions, to locate the  $^{36}Cl$  counts.

## Discussion

Due to the energy loss of SEP in matter, reaction energies on the order of 1 MeV/A become relevant. Table 1 displays seven suggested beam energies, and energies after passing through the Ni foil and  $^3\text{He}$  chamber, along with the necessary magnetic field applied by the analyzing magnet. These energies should produce cross sections ranging from approximately 0.2 mb to 60 mb according to fig. 1.

Voltage(MV)	Charge	Beam Content (%)	$B(T)$	$E_0(\text{MeV})$	$E_{Ni}(\text{MeV})$	$E_{He}(\text{MeV})$
9.0	$8^+$	32.8	0.940	81.0	52.6	50.3
9.0	$9^+$	18.6	0.881	90	62.3	60.1
9.0	$10^+$	5.2	0.831	99.0	71.8	69.7
9.5	$8^+$	33.6	0.966	85.5	57.4	55.1
9.5	$9^+$	21.3	0.905	95.0	67.5	65.4
9.5	$10^+$	6.6	0.854	104.5	77.7	75.6
9.5	$11^+$	1.0	0.810	114.0	87.9	86.0

## References

- [1] M. Bowers et al. “Measurement of the  $^{33}\text{S}(\alpha,p)^{36}\text{Cl}$  cross section: Implications for production of  $^{36}\text{Cl}$  in the early Solar System”. In: *Phys. Rev. C* 88 (6 2013), p. 065802. DOI: 10.1103/PhysRevC.88.065802. URL: <https://link.aps.org/doi/10.1103/PhysRevC.88.065802>.
- [2] J. N. Goswami, K. K. Marhas, and S. Sahijpal. “Did Solar Energetic Particles Produce the Short-lived Nuclides Present in the Early Solar System?” In: *The Astrophysical Journal* 549.2 (2001), p. 1151. URL: <http://stacks.iop.org/0004-637X/549/i=2/a=1151>.
- [3] W.N. Cottingham & D.A Greenwood. *An Introduction to Nuclear Physics*. 2nd. University of Cambridge Press, 2001, pp. 33–111.
- [4] George Raymond Satchler. *Introduction to Nuclear Reactions*. Ed. by George Raymond Satchler. 2nd. Oxford University Press, 1990.

Constructing and Developing the Instrumentation  
for Dissociative Electron Attachment Studies

John (Hulin) Yang

2018 NSF/REU Program

Physics Department, University of Notre Dame

Advisor: Sylwia Ptasińska

July 26, 2018

## Abstract

The Dissociative Electron Attachment (DEA) process lead to a molecular fragmentation. In the DEA process, low energy electrons break bonds in the molecule. The interesting phenomenon in this process is that the electron energy can be lower than the bond dissociation energy. The bond is broken in the resonance state in the electron-molecule interaction. DEA processes involve in physical, chemical, and biochemical studies. In this project, I constructed the instrumentation for the DEA study. Construction of the instrumentation is currently completed and the instrumentation has been tested on  $CO_2$  molecules, as because  $CO_2$  is one of the simplest among polyatomic molecules, and has widely studied for the DEA process.

## Introduction

The DEA process was first found in the Temporary Negative Ion (TNI on timescale  $10^{-12}$  to  $10^{-15}$  s) study, by Schulz[1], in 1973. Schulz noticed the discontinuities at specific energies while looking at the curve of ion yield from TNIs as a function of energy. The discontinuities, peaks or troughs, indicate a fragmentation pathway via electron scattering resonance[2]. The DEA process starts with a low energy electron interacting with a molecule. The electron-molecule-scattering interaction, that forms a TNI in a resonance state, for  $10^{-12}$  to  $10^{-15}$  s. The TNI then decays into two fragments, a neutral and a anion, schematically written as  $AB + e^- \rightarrow A^- + B$ .

Since low energy electrons are likely to exist in various environments, from atmosphere to human bodies, the DEA process takes place in various environments. In earth science studies for instance, the production of oxygen in the primitive earth atmosphere is essential to questions like the origin of life. Apart from the three-body recombination reaction and the  $CO_2$  photo-dissociation under ultraviolet light, the DEA process might be a pathway to produce oxygen or to produce oxygen atoms or  $O^-$  anions which can then form oxygen molecules[3].

In a human body, the damage to DNA molecules would cause cancer when the mutation quantity is over the limitation of immunity. Instead of incoming high-energy quanta, the secondary species produced by the direct radiation inside the

body are mostly responsible for the DNA-molecule-damage. The secondary species include radicals, excited molecules, ions, and secondary electrons (SEs). Furthermore, SEs like sub-ionizing electrons are the most copiously secondary products during radiation therapy. Some pioneering work showed that electrons with energy below the bond dissociation energy are capable of breaking DNA molecules. Their work-data showed some resonance peaks. Therefore, the DEA process is very likely to be a key for understanding the cancer[4]. Also, plasma studies are closely related to the DEA process. For example, molecular damage by low-energy plasmas involves the DEA process[5]. So, the DEA process is a key to understanding oxygen production in primitive atmosphere, the cause and treatment of cancer, the plasma action both in industry and biology, etc.

In order to carry out DEA studies, the molecules should be introduced into a vacuum chamber. An ion source inside the chamber can emit electrons. The molecules capture the electrons, to form TNIs. TNIs then decay into neutrals and anions. By measuring anion yield at different energies, one can reveal, identify and quantify various fragmentation patterns of different biologically relevant molecules in the gas phase.

# Experimentation

## Vacuum chamber

For this summer project, I carried out the DEA study in a cylinder vacuum chamber with a diameter of 10 inches and a length of roughly 20 inches. To achieve high vacuum level inside the chamber, a two-level pumping system is adopted, since different vacuum pumps have different vacuum limits and working ranges.

A SH-110 Dry Scroll Pump and a TwisTorr 304 FS turbo molecular high-vacuum pump are used in our experiment. The scroll pump can achieve of at most  $10^{-3}$  mbar, and can work under atmosphere. The turbo pump can technically reach as high as  $10^{-10}$  mbar, but has to work under a vacuum of lower than  $10^{-1}$  mbar. In the two-level pumping system, the exhaust of the turbo pump is connected to the dry scroll pump for rough pumping, to produce a pressure, under which the turbo pump can work efficiently[6]. An ion gauge mounted to the chamber is necessary in the vacuum system for monitoring the pressure inside the chamber. After switching on the scroll pump under atmospherical pressure, the pressure drops to  $9.45 \times 10^{-2}$  mbar in one hour. The turbo pump was turned on and decreased the pressure to  $9.87 \times 10^{-7}$  mbar in 5.5 hours. The high-vacuum level is well accomplished. Under such high-vacuum, the background noise is minimized. Since the gas inlet is already mounted

and capable of introduction of sample, the next part needed for the experiment would be the electron source and the anion detecting device.

## **QMS(Quadrupole Mass Spectrometer)**

On the front end of the quadrupole is an electron ionization ion source. In the ion source part, electrons are emitted by filaments and interact with molecules. Interactions include elastic scattering, excitation, ionization, ion pair formation and electron capture. Electron capture results in formation of stable molecular anions, auto detachment, and DEA. The intensity of each interaction depends primarily on the structure of the molecule and the electron energy. The various fragments like the molecular ions, anions from the DEA process, etc, can be detected by the quadrupole part of the QMS, and can indicate their intensities.

The quadrupole mass spectrometer which was used is a HAL/3F series QMS from Hiden Analytic Inc. It can measure the mass spectrum up to 300 amu. Also, it can measure the ion yield as a function of energy or time[6].

The quadrupole mass spectrometer was mounted to the chamber and connected to the a computer. The software MASsoft is used to monitor and control the quadrupole mass spectrometer. Measuring the mass spectrum and measuring the ion yield can all be done with the MASsoft. The instrumentation for the DEA study is constructed

and is ready for experimental test and further adjustments.

## Testing of gas phase $CO_2$

A functioning mass spectrometer would distinct background from  $CO_2$  gas since their spectrums are different. In figure 1 we can see peaks at mass 28 and 32 and no peak at mass 44 on the background spectrum, because the background in the chamber is mostly the remaining substance of the air. Comparing with the background spectrum, peaks at mass 28 and mass 32 dropped while a sharp peak reveals at mass 44, indicating the reduction of  $N_2^+$  yield and  $O_2^+$  yield, and the increase of  $CO_2^+$  yield. I compared the spectrum to the standard  $CO_2^+$  spectrum on the NIST web site, whereas did not match perfectly. The  $CO_2^+$  gas phase spectrum looks rather like a superposition of the  $CO_2^+$  spectrum and air spectrum[7].

Positive and negative ions are formed in the  $CO_2$  gas phase. Their yields as a function of energy can be measured by the QSM. Positive ions,  $C^+$ ,  $O^+$ ,  $CO^+$  etc., would yield when electron energy is high enough, showing thresholds in ion yield curves as a function of electron energy, as shown in figure 2. And we can see that above 70 eV, most of the molecules are ionized so that the ion yield tends to be constant.

Negative ions including  $C^-$ ,  $O^-$ ,  $CO^-$  etc., can yield via DEA process at certain electron energies. Similar to the classical mechanical resonance where the frequency of a periodical force matches the eigenfrequency of the object, if an electron with certain energy that matches the eigenfrequency of the molecule, the electron-molecule scattering can result in a TNI, in a resonance state. Those molecule eigenfrequencies reveal themselves as peaks on the curve, as shown in figure 3.

Both the thresholds and resonance peaks had been measured and compared with data from NIST and previous works[3]. However, they do not match well. The main cause comes from contamination of the air and the chamber wall.

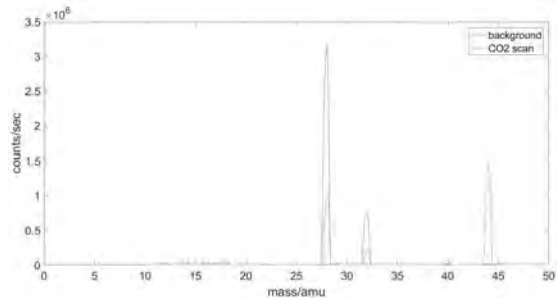


Figure 1: background spectra &  $CO_2$  gas phase spectra comparison

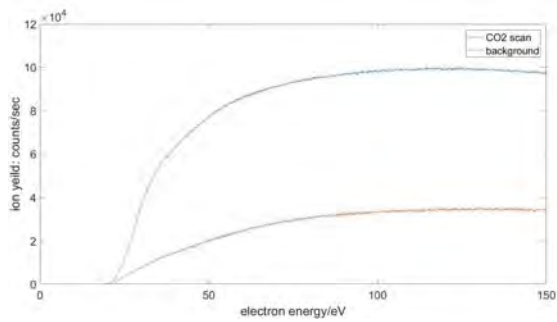


Figure 2: positive ion  $O^+$  yield curve as a function of electron energy

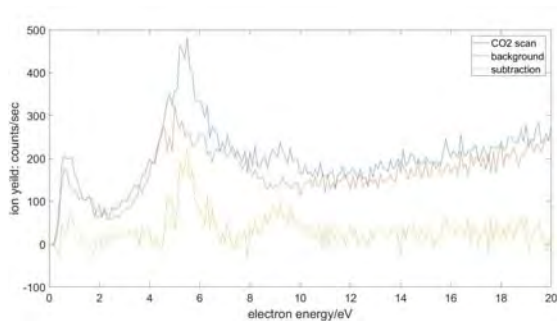


Figure 3: negative ion  $O^-$  yield curve as a function of electron energy

Long time pumping and baking should be done for the next step of the DEA study, to eliminate contaminations.

## Conclusion

The apparatus for the DEA study is constructed and tested on gas phase  $CO_2$ . A high-vacuum inside the chamber is achieved. However, the gas phase  $CO_2$  test data has not been satisfying. More sets of repetitive tests on  $CO_2$  gas phase, long time pumping, and baking of the chamber shall be carried out to be ready for the DEA studies on various molecules, from simple polyatomic molecules like  $CCl_4$ , to complex biomolecules like DNA molecules.

## References

- [1] Sanche, Schulz. Electron, Transmission Spectroscopy - Resonance in Triatomic Molecules and Hydrocarbons (1973), J. Chem. Phys., Vol. 58, no. 2, pp. 479-493

- [2] Ilya I. Fabrikant, Samuel Eden, Nigel J. Mason, Juraj Fedor, *Advances In Atomic, Molecular, and Optical Physics* (2017), pp. 547-548
- [3] Xu-Dong Wang, Xiao-Fei Gao, Chuan-Jin Xuan and Shan Xi Tian, Dissociative electron attachment to CO<sub>2</sub> produces molecular oxygen (2016), *Nature Chem.*, Vol. 8
- [4] Arreola, Esmeralda, *Dissociative Electron Attachment* (2016), APS March Meeting
- [5] James J. Munro, Stephen Harrison, Milton M Fujimoto, and Jonathan Ten-nyson, A dissociative electron attachment cross-section estimator (2012), *Journal of Physics, Conference Series* 388
- [6] Zhou L. Kastner. *Dissociative Electron Attachment to gas phase biomolecules*(2017), Ph.D. Dissertation, pp.41-52
- [7] <https://webbook.nist.gov/chemistry/> (accessed on Jul. 24th, 2018)

Using Spectral Stacking to Probe the Baryonic Mass of the  
Milky Way Halo with Fe XIV absorption

Theodora Zastrocky

2018 REU Program

Department of Physics, Notre Dame University

Advisor: Professor J. Christopher Howk

## Abstract

The hot gas in the halo of the Milky Way is a possible solution to the “baryon budget deficit”: the underabundance of baryons compared with the Galaxy’s total gravitational mass. We use a new approach of spectral stacking with spectra from the KODIAQ survey to limit the column density of Fe XIV in the Milky Way halo, which peaks in abundance at the virial temperature of the Milky Way. We produce mean and median flux stacks of 95 spectra of distant quasars (QSOs) whose sightlines pass through the Galactic halo, adopting the median stack as our fiducial choice. We use these spectra to set a  $3\text{-}\sigma$  upper limit on the equivalent width ( $W_\lambda$ ) of the average Milky Way halo sight line of  $W_\lambda < 8 \text{ m}\text{\AA}$  for the mean stack and  $W_\lambda < 7 \text{ m}\text{\AA}$  for the median stack. We use these  $W_\lambda$  limits to calculate an upper limit on  $N(\text{Fe XIV})$ . This derived upper limit is  $N(\text{Fe XIV}) < 6 \times 10^{16} \text{ cm}^{-2}$  for the mean stack and  $< 5 \times 10^{16} \text{ cm}^{-2}$  for the median stack. We calculate an upper limit on the mass of the halo from our fiducial  $N(\text{Fe XIV})$  limit. Assuming a constant gas density distribution the derived halo mass upper limit is  $m < 6 \times 10^{13} M_\odot$ . Assuming a  $\beta$ -model gas density distribution the derived halo mass upper limit is  $m < 3 \times 10^{14} M_\odot$ . The halo mass limit is a factor of 1000x higher than the expected baryonic mass of the halo and thus not strongly constraining. This indicates that using our spectral stacking technique, many more spectra than the 95 in our sample are needed to detect Fe XIV absorption and set a constraint on the mass of the Milky Way halo.

## 1. Introduction

We estimate the baryonic mass associated with the Milky Way based on the dark matter mass of the Milky Way using the following ratio:  $\Omega_b / \Omega_m$ , where  $\Omega_b$  is mass-energy density of baryonic matter and  $\Omega_m$  is total mass-energy density. Planck (2015) found that in the universe,

$\Omega_b / \Omega_m \approx 0.16$ . Eadie & Harris (2016) determined the mass of the Galaxy  $M_{\text{mw}} \approx 9 \times 10^{11} M_{\odot}$ . The baryonic mass of the Galaxy predicted by  $\Omega_b / \Omega_m$  is  $M_b \approx 1.4 \times 10^{11} M_{\odot}$ . However, when we sum the mass from all the luminous stars and gas in the galaxy, we find  $M_b \approx 6.5 \times 10^{10}$  (Licquia et al. 2016). This is a factor of 2x smaller than the prediction. It is thought that baryons follow gravitationally dominant dark matter into the hot, highly ionized, gaseous halo of a galaxy. Thus, it is worthwhile to investigate the halo of the Milky Way to look for all of the baryons in order to assess the “baryon budget deficit” (Tumlinson et al. 2017). In this paper we limit the mass of the halo gas using Fe XIV as a tracer of halo gas. We use Fe XIV because it peaks in abundance at the virial temperature (2 MK) of the Milky Way (Gnat & Sternberg 2007). However, the 5302 Å transition of Fe XIV is extremely weak ( $f \sim 5 \times 10^{-7}$  from NIST). At typical metal ion columns through the halo, we would need a signal-to-noise ratio, SNR  $\sim 3000$ , to detect measurable absorption. It is difficult with our current telescopes to achieve a high enough SNR from single observations. Our solution is to stack a large number of spectra from multiple sightlines to produce a composite spectrum with a higher SNR than any single spectrum. We used spectrum along multiple quasar (QSO) sight lines through the Galactic halo drawn from the KODIAQ survey (O’Meara et al. 2017). We describe our production of spectral stacks in Sect 2. We describe our limits on the equivalent width ( $W_{\lambda}$ ) and column density of Fe XIV absorption ( $N(\text{Fe XIV})$ ) and use these to derive a limit on the total mass of the gaseous halo in Sect. 3 Our limits to the baryonic mass of the halo are not competitive with other assessments; we discuss the implications in Sect. 4.

## 2. Methods

### 2.1. Initial estimate of $N(\text{Fe XIV})$

We made two initial predictions of N(Fe XIV) that we expect in the halo based on a halo mass estimate of  $10^{11} M_{\odot}$ : one assuming a constant density of H in the Galaxy and one using a  $\beta$ -model to model the density of H in the Galaxy. We use the  $\beta$ -model power law approximation and parameter best fit values from Miller & Bregman (2015). The  $\beta$ -model power law approximation is defined as:

$$n(r) \approx \frac{n_o r_c^{3\beta}}{r^{3\beta}}$$

Following Miller & Bregman (2015) we adopt  $n_o r_c^{3\beta} = 1.35 \times 10^{-2} \text{ kpc}^{3\beta} \text{ cm}^{-3}$ , and  $\beta = 0.5$ . We adopt a virial radius of the Milky Way of 300 kpc. The constant density model and  $\beta$ -model density model initial estimates of N(Fe XIV) are summarized in Table 1 below:

Density Model	N(Fe XIV) $\text{cm}^{-2}$
Constant density	$7.4 \times 10^{13}$
$\beta$ -model density	$3.5 \times 10^{13}$

## 2.2. The Stack

We began with a sample of sightlines from various QSOs from the KODIAQ data survey. Our initial collection contained 300 spectra. We eliminate spectra toward QSOs at redshift  $z > 3.25$  to avoid contamination from intergalactic absorption. We also eliminated spectra that did not cover  $5302.86\text{\AA}$ : the transition wavelength of Fe XIV. Through experimentation we found that using spectra with  $\text{SNR} > 20$  produced the highest quality stacked spectrum. We eliminated spectra with  $\text{SNR} < 20$  from our sample. Our final selection consists of 95 spectra. For each spectrum in our sample we convert wavelength to velocity. Each spectrum is trimmed to only include data for  $\pm 1500 \text{ km/s}$  and resampled onto a regular grid with  $\Delta v = 2.5 \text{ km/s}$  per pixel. We mask all pixels in each spectrum where the error  $< 0$  as this indicates an error with the telescope, and thus a bad pixel.

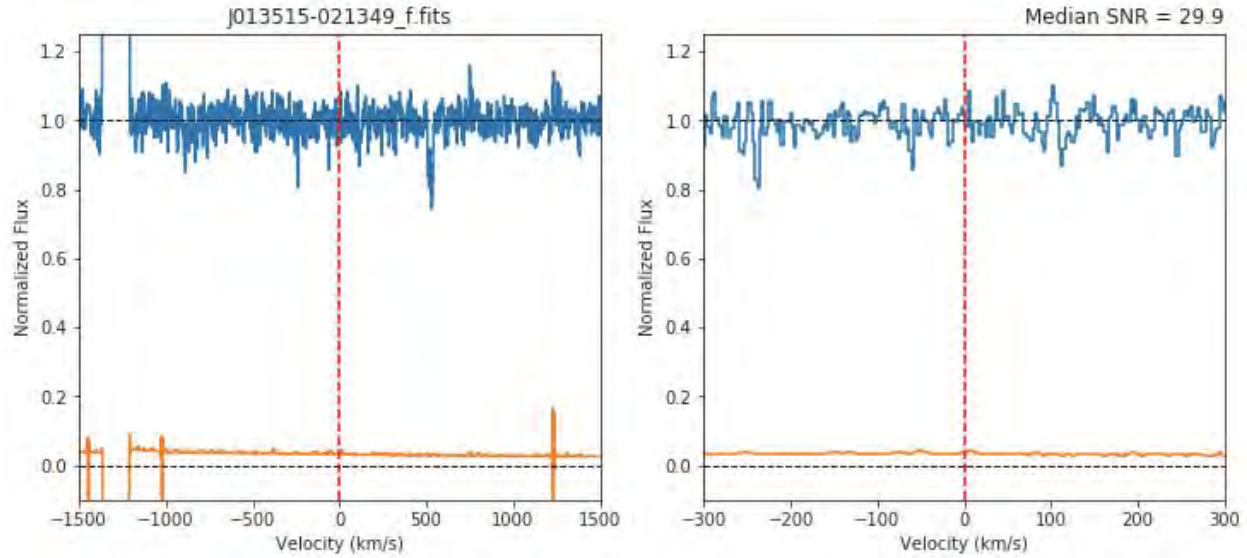


**Figure 1**

A plot of normalized flux (blue) and error (orange) vs velocity of the spectrum from the QSO sightline J013515-021349. The righthand plot is the spectrum over only  $\pm 300$  km/s

We employ two statistics to produce the stacked spectrum: the median and the mean. To produce the median stack, we take the median of the flux at every point in our velocity grid for each of the 95 spectra in our sample. This produces a composite flux array. The median is more robust than the mean because the mean is sensitive to outliers. We know that there is contaminating absorption. It is easy to identify the contaminating absorption through a visual inspection of the spectra, but the contaminating absorption will be masked once the spectra is stacked and may be mistaken for Fe XIV absorption. In order to use the mean to produce a stack, we must first eliminate contaminating absorption. We do this with two techniques: mask all flux less than 0.85, and a 2.5 sigma outlier clipping on the masked flux for the mean stack. We expect Fe XIV to be present along all sight lines to a small extent. Thus, removing outliers is unlikely to impact this pervasive absorption. Using the clipped, masked flux and the mean statistic, we produce the mean stack with the same process as we did the median stack.

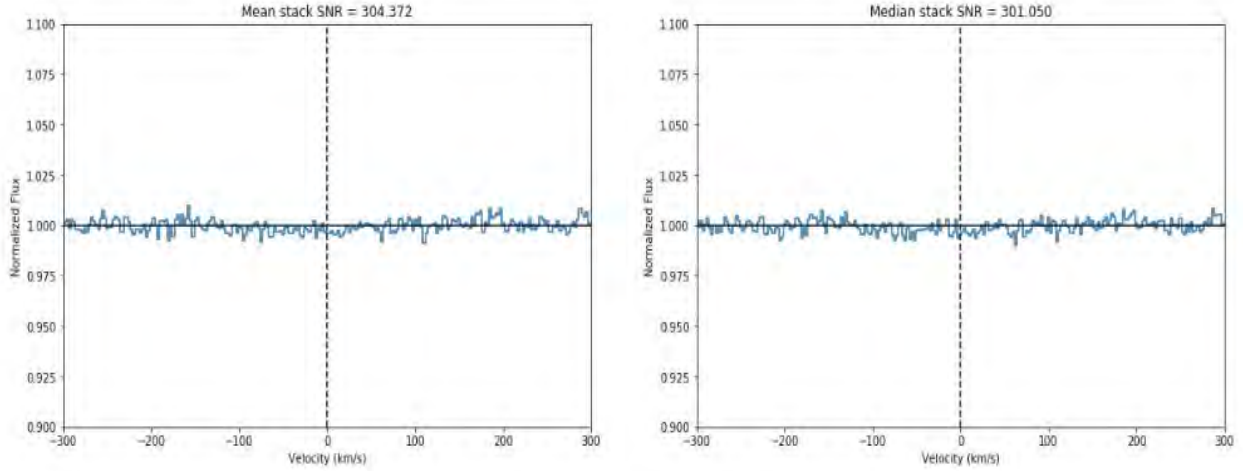


**Figure 2**

Normalized flux vs velocity is plotted for the mean stack (right) and the median (left). The two spectra are very similar.

We estimate the error in the flux for each of our stacked spectrum using bootstrap resampling to create 100 resamples of the data, using the standard deviation at each point in the resulting stacks as estimates of the uncertainties.

We produced a mean and median stack in order to compare features of the resulting spectra. The two stacked spectra are very similar; however, we adopt the median stack as our fiducial choice as it is still less prone to outliers than the masked mean.

### 3. Analysis

We do not detect Fe XIV absorption in our stacked spectra. We calculate limiting equivalent widths ( $W_\lambda$ ) and column densities,  $N(\text{Fe XIV})$ , and use these to limit the mass of the gaseous halo.

#### 3.1. Equivalent Width Calculation

We use the renormalized flux stacks trimmed to a velocity range of  $\pm 300$  km/s to calculate the  $W_\lambda$  of all the flux in our velocity range for each of our three stacks. We calculated  $W_\lambda$  over  $\pm 300$  km/s using the equation defined below:

$$\sum (1 - F_\lambda) \Delta\lambda,$$

where  $F_\lambda$  is the flux at each wavelength and  $\Delta\lambda$  is the change in wavelength per pixel.

We then calculate the error in our  $W_\lambda$  using the error arrays created through bootstrap resampling. We do not detect significant Fe XIV absorption, finding 3- $\sigma$  upper limits of  $W_\lambda < 7$  mÅ (median stack) and  $< 8$  mÅ (mean stack).

### 3.2. FeXIV Column Density Calculation

We calculate an upper limit on the column density of Fe XIV in the Milky Way Halo using equation 3 from Savage & Sembach (1996) as defined below:

$$N(\text{cm}^{-2}) = 1.13 \times 10^{17} \frac{W_\lambda(\text{m}\text{\AA})}{f \lambda^2(\text{\AA})}.$$

Here  $W_\lambda$  is our  $W_\lambda$  upper limit in mÅ,  $f$  is oscillator strength that we adopt as  $f = 5.08 \times 10^{-7}$  (from NIST), and  $\lambda$  is the rest wavelength  $\lambda = 5302.86$  Å. We calculated an upper limit on  $N(\text{Fe XIV})$  in the halo of  $< 5 \times 10^{16}$  (median stack) and  $< 6 \times 10^{16} \text{ cm}^{-2}$  (mean stack).

### 3.3 Halo Mass limit calculation

We calculate an upper limit on the halo mass using our median  $N(\text{Fe XIV})$  limit, assuming that the halo extends 300 kpc radially outward from the center of the Galaxy. We first calculate a halo mass limit assuming a constant density distribution of the halo gas. Constant

density distribution however, is an oversimplification. We also calculate a halo mass limit using a more realistic  $\beta$ -model gas density distribution. We use the same  $\beta$ -model from Miller and Bregman (2015) that we used to initially estimate  $N(\text{Fe XIV})$  in section 2. We use our  $N(\text{Fe XIV})$  limit to derive  $n_o r_c^{3\beta}$  from the following equation:

$$N(r) = \int \frac{n_o r_c^{3\beta}}{r^{3\beta}} dr,$$

where we integrate from 8 kpc to 300 kpc. We derive  $n_o r_c^{3\beta} = 5.215 \times 10^{-4} \text{ kpc}^{3\beta} \text{ cm}^{-3}$  assuming Miller & Bregman (2015) best fit value of  $\beta = 0.5$ . We then use the full  $\beta$ -model to calculate the mass of Fe XIV in the halo using the following equation:

$$M = \int n_o \left(1 + \left(\frac{r}{r_c}\right)^2\right)^{-3\beta/2} 4\pi r^2 dr.$$

We assume  $r_c = 1$  kpc. We adopt Miller & Bregman (2015) best fit value of  $\beta = 0.5$ . We integrate along the radius of the Galaxy, from 0 kpc to 300 kpc.

We convert the mass of Fe XIV in the halo to the mass of H in the halo using the ionization fraction of Fe XIV, the solar abundance of Fe XIV and the metallicity of the halo relative to the sun:  $x(\text{Fe XIV})$ ,  $Z_\odot$  and  $Z/Z_\odot$  respectively. We assume  $x(\text{Fe XIV})=0.243$  for gas at  $T = 2$  MK (Gnat & Sternberg 2007),  $Z_\odot = 2.8 \times 10^{-5}$ , and  $Z/Z_\odot=0.3$  (Miller & Bregman 2015). Our derived halo mass upper limit assuming constant density is  $m < 6 \times 10^{13} M_\odot$ . Our derived halo mass upper limit assuming  $\beta$ -model density distribution is  $m < 3 \times 10^{14} M_\odot$ . These are respectively a factor of 100x and 1000x higher than predicted based on the gravitational mass of the Milky Way. Thus our limits are not competitive with other constraints (e.g., X-rays by Miller & Bregman 2015).

Limit	Median Stack	Mean Stack
$W_\lambda$ (mÅ)	< 7	< 8
$N(\text{Fe XIV})$ (cm <sup>-2</sup> )	< $5 \times 10^{16}$	< $6 \times 10^{16}$
Halo mass constant density distribution ( $M_\odot$ )	< $6 \times 10^{13} M_\odot$	
Halo mass $\beta$ -model density distribution ( $M_\odot$ )	< $3 \times 10^{14} M_\odot$	

#### 4. Discussion

Our  $N(\text{Fe XIV})$  and halo mass limits are too high by orders of magnitude to set a constraint on  $N(\text{Fe XIV})$  in the halo and a constraint on the halo mass. This indicates that using our spectral stacking technique we need many more spectrum to add to our stack to improve the SNR if we are to be able to detect Fe XIV in the halo. Whole sky surveys such as the Sloan Digital Sky Survey (SDSS) may provide a large enough database of spectrum to detect Fe XIV in the halo. Another possibility is that improved high-resolution telescopes will be developed that will increase the SNR of individual spectra. A collection of spectra with a higher SNR than our collection may not need to be as large as our collection of spectra from the KODIAQ survey in order to detect Fe XIV in the halo. It is worth noting that in our stack we weighted all spectra equally. A next step could be weighting by the inverse variance. This would tend to increase the total S/N. It would do so however, at the cost of weighting some directions more than others, thus making the interpretation more complex. It is possible that Fe XIV is more densely distributed in the region near the center of the galaxy. Future work could select only sight lines along the central region of the Galaxy. However, this only will be interesting if the Galaxy's central region is 1000x overabundant in Fe XIV compared with typical halo.

## 5. Summary

We developed a new technique of spectral stacking for probing the halo of the Milky Way through very weak Fe XIV absorption. Spectral stacking achieves a higher SNR than any single spectrum and our spectral stack reaches SNR  $\sim 300$ . We do not detect Fe XIV absorption, and our halo mass limits are orders of magnitude higher than those predicted for the Milky Way. However, we learned that with a larger spectra collection or higher quality individual spectrum we can use the technique of spectral stacking to set a constraint on the mass of the Milky Way halo and thus estimate the baryonic mass contained in the halo and perhaps account for the “baryon budget deficit.”

## References

1. Planck Collaboration 2016, *A&A*, 594, A13
2. Eadie, G.M., & Harris, W.E. 2016, *ApJ*, 829, 108
3. Licquia, T., Newman, J., & Bershady, M. 2016. *ApJ*. 833, 220
4. Tumlinson, J., Peebles, M.S., & Werk, J.K. 2017. *ARAA*. 55, 389
5. O’Meara, J.M., et al. 2017. *AsJ*. 154, 114
6. Miller, M.J., & Bregman, J.N. 2015, *ApJ*, 800,14
7. Gnat, O., & Sternberg, A. 2007, *ApJS*, 168, 213
8. Savage, B., & Sembach, K., 1996. *ARAA*. 34, 279